Computational Modeling of Metal-Metal Interactions in Inorganic Complexes Using DFT Methods

By

Trey C. Pankratz

A dissertation submitted in partial fulfillment of the requirements for the degree of Doctor of Philosophy

(Chemistry)

at the UNIVERSITY OF WISCONSIN-MADISON 2025

Date of final oral examination: 9/2/2025

The dissertation is approved by the following members of the Final Oral Committee:

John F. Berry, Professor, Chemistry

Thomas C. Brunold, Professor, Chemistry

Daniel C. Fredrickson, Professor, Chemistry

JR Schmidt, Professor, Chemistry

Dedication – To the underdogs and the first-timers. I'll give you some advice I got yesterday. It's not always going to feel rewarding to you, but the doing of it changes the world.

Acknowledgements

I would like to thank my friends, my family, my committee, John and the rest of the Berry lab, and the staff and regulars at Sconniebar. The last few years have been turbulent to say the least. Thank you for your support and friendship, especially here over the last half a year, when things have gotten the darkest. Without all of you, this document wouldn't have hit the page.

Abstract

The electronic structure and bonding of inorganic complexes has always been of interest to the chemical community, especially in more complicated systems, such as in systems with metal-metal interactions. Recently, density functional theory (DFT) methods have been utilized to help better understand these complicated inorganic systems. In this work, I will showcase the versatility of these approaches to better understand the magnetic and spectroscopic behavior of inorganic complexes, to explain the bonding in these complexes, and to predict desirable complexes exhibiting new features in their electronic structure. In Chapter, 1 DFT calculations for Ru2M(dpa)4Cl2 (dpa = dipyridylamine) (M = Mn, Fe, Co, Mo, Tc, Re, W, Os) were used to determine the ground spin states of these complexes, and for the subset of (M = Mo, Tc, Re, W, Os), we show the formation of new Ru-M bonds, surpassing the strength of the starting material's Ru-Ru bond. In Chapter 2, the synthesis of dicolbalt paddlewheel complexes using acetate equatorial ligands and ether axial ligands is shown. These complexes were investigated using SQUID magnetometry, giving a J value of -31.7 cm-1. Broken symmetry (BS)-DFT calculations show that the magnetic exchange pathway is a function of both Co-Co distance and of Co-Co-L (L = axial ligand) angle. It is also shown that these complexes are competent for carbene reactivity. In Chapter 3 we show the synthesis of a novel hexa-iron complex. This complex was analyzed using bond valence sum (BVS) analysis , DFT calculations, Mössbauer spectroscopy and electrochemical data to give the formulation of [Fe6O2(OH)(H3L)L], with nominally four Fe(II) ions and two Fe(III) ions. In Chapter 4, the synthesis of complexes of the form Mo2M(dedpa)4Cl2 (dedpa = diethyl-dipyridylamine) (M = Cr, Mn, Fe, Co, Ni) is explored. These complexes are shown to be more electron rich, easier to oxidize, and, interestingly, the impact of the ethyl substituents is not applied equally to all three metal. Additionally, the

mechanism of ligand rearrangement is explored by DFT, showing that combating forces of ligand rearrangement energy and the interaction energy between the metals and the equatorial ligands drives the energetic barrier for ligand rearrangement.

Table of Contents

Chapter 1: Computational Investigation of a New Class of Heterometallic Ru-M Bonded Cores

Trey C Pankratz, Thomas Hsu, John Berry

TCP and HS contributed equally to this work.

Abstract: In this work, we showcase computational results exploring HEMACs derived from the Ru_2dpa_4Cl (dpa = N,N'-diphenylamine) metalloligand and two series of metal salts, namely $Ru_2Mdpa_4Cl_2$ (M = Mn, Fe, Co, Mo, Tc, W, Re, Os; compounds **1** – **8** and their monocations **1**$^+$-**8**$^+$). The spin states and structures of these compounds are of interest, in particular, we predict compounds **1**-**3** and **1**$^+$-**3**$^+$ to exist in high-spin states derived from ferromagnetic interaction of the Ru_2- and M-based unpaired electrons. The early transition metal complexes **4**-**7** and the cations **4**$^+$-**8**$^+$ are predicted to either partially or completely cleave the Ru-Ru bond in favor of a new, heterometallic Ru-M multiple bond.

Section 1.1: Introduction Metal-metal bonded complexes have garnered much attention over the past forty years, due to their various applications, but mainly because of what they have taught us about fundamental aspects of chemical bonding.[1, 2] Heterometallic extended atom chain (HEMAC) complexes are a class of metal-metal bonded compounds at the forefront of the field of metal-metal bonds, having possible applications as molecular-scale circuitry components, but also having unusual bonding features that provide challenges to theory and computational modeling. We focus on trimetallic HEMACs, in which the metal core composition can be either $M_AM_AM_B$, $M_AM_BM_A$, or $M_AM_BM_C$.[1,

[3] The polar $M_AM_AM_B$ compounds are of particular interest due to their possible use as molecule-scale rectifiers,[4, 5] and the fact that the compounds present a single heterometallic interaction that can be probed.

Unsymmetric $M_AM_AM_B$ compounds have been examined by the groups of Berry and Peng; the inventory of known compounds is shared in Table 1.1.1. The Berry lab has focused on compounds containing a quadruply-bonded M_AM_A pair, either CrCr, MoMo, or WW. They have developed a synthetic strategy involving deliberate synthesis of a M_AM_A metalloligand (e.g., $Cr_2(dpa)_4$ where dpa = 2,2'-dipyridylamide, the ligand shown in Table 1), followed by metalation of a M_BX_2 salt to form the HEMAC structure.[6] Similar approaches have been developed by the Peng lab.[7, 8]

Table 1.1.1. Known asymmetric $M_AM_AM_B$ HEMACs

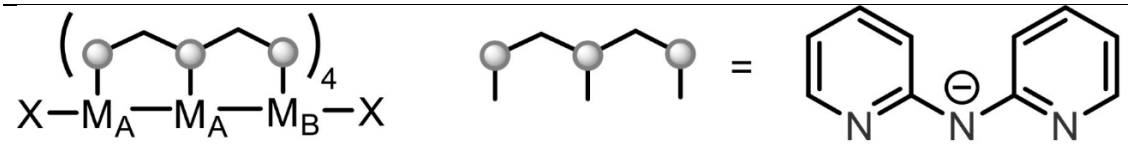

M_A	M_B	Ref.
Cr	Cr, Mn, Fe, Co, Ni, Zn	[9]
Mo	Cr, Mn, Fe, Co, Ni, Ru	[10]
W	Cr, Mn, Fe, Co, Ni, Ru	[11]
Ru	Mn, Fe, Co, Ni, Cu, Zn	[8]
	Ru, Rh, Pd, Cd	
Rh	Mn, Fe, Co, Ni, Cu	[7]
	Ru, Rh, Pd, Cd	
	Ir	

One thing that the systems in which M_A = Cr, Mo, W, or Rh have in common is that the metal-metal bonded metalloligand has a diamagnetic ground state. Thus, magnetic properties of $M_AM_AM_B$ compounds with paramagnetic M_B ions typically are similar to those of an isolated M_B complex, though there tends to be some delocalization of spin due to overlap of d_{z^2} orbitals of the two M_A atoms and M_B.[10] The question of what happens to the

electronic structure and magnetism when the M_AM_A group contains unpaired electrons has not been fully investigated.

We have recently reported an example of a cationic $[Mo_2Ni(dpa)_4Cl_2]^+$ species, formed upon one electron oxidation of $Mo_2Ni(dpa)_4Cl_2$.[12] In this case, it is the Mo_2 unit that becomes oxidized rather than the Ni, such that the cation contains both a paramagnetic Mo_2^{5+} group having a $\sigma^2\pi^4\delta^1$ electron configuration ($S_{Mo_2} = 1/2$), and a paramagnetic, high-spin Ni(II) ion ($S_{Ni} = 1$). The two spin centers, S_{Mo_2} and S_{Ni}, could interact either antiferromagnetically, yielding a total spin state, S_T, of ½; alternatively, S_{Mo_2} and S_{Ni} could have a ferromagnetic interaction to give $S_T = 3/2$. Ultimately, the $S_T = 3/2$ state wins out, and this state is magnetically isolated up to room temperature. The reason for this is that S_{Mo_2} and S_{Ni} are not isolated spin centers, but are bonded, having an unpaired electron delocalized in a three-center non-bonding orbital, σ_{nb}. The other two unpaired electrons, one housed in a Mo_2 δ bonding orbital, and the other housed in a Ni-centered δ-symmetry orbital, are both orthogonal to the delocalized σ_{nb} spin, and thus all three spins align parallel in agreement with the Goodenough-Kanamori rules.[13-16]The mechanism of exchange within this system is related to the concept of double exchange, in which the spin of an itinerant (delocalized) electron causes the alignment of other (localized) unpaired electrons within the system.[13]

$M_AM_AM_B$ compounds in which M_A = Ru are predicted to share the complexity of the Mo_2Ni cation because the Ru_2 group is also paramagnetic.[1] A further complexity of Ru_2M_B compounds is the distribution of charge. Metal-metal bonded Ru_2 compounds are remarkably stable in the mixed-valent Ru_2^{5+} oxidation state, and the homovalent Ru_2^{4+}

species tend to be quite reducing, especially when supported with strongly basic ligands. Thus, there are two limiting charge distributions for Ru_2M_B HEMACs, as outlined in Figure 1.1.1. Distribution **A** has both Ru atoms and M_B in the same, 2+ oxidation state, while distribution **B** involves a mixed-valent Ru_2^{5+} group appended to a M_B^+ ion.

Electronic Structure Possibilities

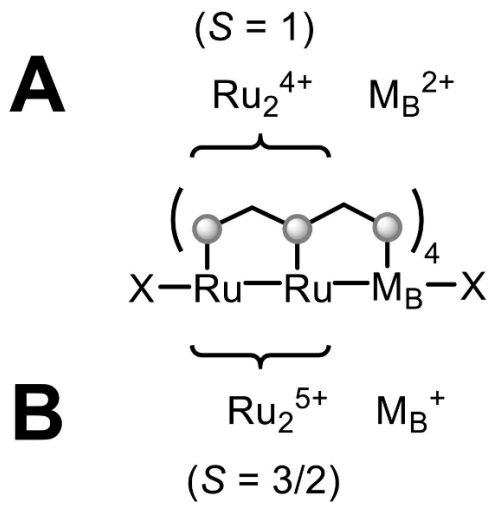

Figure 1.1.1. Possible distributions of charge within Ru_2M_B HEMAC compounds.

Simple dimers in the Ru_2^{4+} redox state have the electron configuration $[Q]\delta^{*2}\pi^{*2}$, where [Q] denotes the $\sigma^2\pi^4\delta^2$ core of the quadruple bond. The occupation of orthogonal π* orbitals with one electron each leads to a triplet (S_{Ru_2} = 1) ground state, similar to the ground triplet state of O_2. In the Ru_2^{5+} oxidation state, the configuration is $[Q]\delta^{*1}\pi^{*2}$, where the near-degeneracy of the δ* and π* orbitals gives rise to a parallel alignment of spins and a quartet (S_{Ru_2} = 3/2) ground state, and an analogy may be made to the quartet state of octahedral Cr^{3+} compounds.

By combining our understanding of the Ru_2 dimers with our observations of the $[Mo_2Ni(dpa)_4Cl_2]^+$ cation, we may expect that Ru_2M_B HEMACs may have interesting magnetic properties. Specifically, when M_B is a paramagnetic metal, the itinerant σ-symmetry electrons, being orthogonal both to any π or δ symmetry unpaired electrons on the Ru_2 unit and on M_B, will enforce parallel alignment of all of these spins. Thus, we may expect the highest possible spin states to be favored in these cases, i.e., ferromagnetic coupling between the Ru_2 group and M_B. As an example of this, the compound $Ru_2Ni(dpa)_4Cl_2$ has been shown experimentally to have an $S_T = 2$ ground spin state.[17] Computations indicate that the compound shows electron distribution **A**, with an Ru_2^{5+}–Ni^+ electronic structure. The S_{Ru_2} = 3/2 and S_{Ni^+} = 1/2 spins couple ferromagnetically to yield the $S_T = 2$ ground state. Interestingly, Raman studies of $Ru_2Ni(dpa)_4Cl_2$ indicate that there are two low-lying excited states available that are proposed to have electron distribution **B**.[18-20]

Even though crystal structures of other Ru_2M_B compounds have been reported in which M_B is a paramagnetic metal (Mn, Fe, or Co), magnetic properties of these compounds have not been determined, and no electronic structure calculations have been reported. In this work, we report an analysis of the spin state energetics of the Ru_2M_B series with M_B = Mn, Fe, and Co (compounds **1**, **2**, and **3**, respectively) in order to test the hypothesis outlined above predicting these compounds to prefer a ferromagnetic, high-spin ground state.

Additionally, we examine a second series of Ru_2M_B compounds in which M_B are second- or third-row transition metals. As shown in Table 1.1.1, such compounds are known with M_B = Rh, Pd, Cd, or Ir. Magnetic measurements of $[Ru_2Rh(dpa)_4Cl_2]^+$ and $[Ru_2Ir(dpa)_4Cl_2]^+$ cationic

complexes have been made, and electronic structure calculations on these two HEMACs have been performed[8], indicating a strongly delocalized three-center bonding interaction with both σ and π character, as is also the case for the homotrimetallic $Ru_3(dpa)_4Cl_2$. The second series of compounds examined here explores new Ru_2M_B combinations in which M_B is an early second or third row transition metal. In contrast to the cases of known Ru_2M_B compounds in which either the Ru–Ru bond is stronger than the Ru–M_B bond, or where there is delocalcization across all three metals, we predict complexes with early metals that display greatly weakened Ru–Ru bonding and strong Ru–M_B heterometallic bonding (Figure 1.1.2). The new $Ru_2M_B(dpa)_4Cl_2$ compounds have M_B = Mo, Tc, W, Re, or Os (compounds **4**, **5**, **6**, **7**, or **8**, respectively). These new metal-metal bonded compounds are worth synthetically targeting in order to test the predicted change in bonding properties, and also due to possible synthetic utility as an entry to explore new polar metal-metal bonds. These compounds could also be used as precursors to other, truly heterotrimetallic systems of the form M'RuMB$(dpa)_4Cl_2$ by replacement of the weakly bonded Ru atom with a new metal M'.

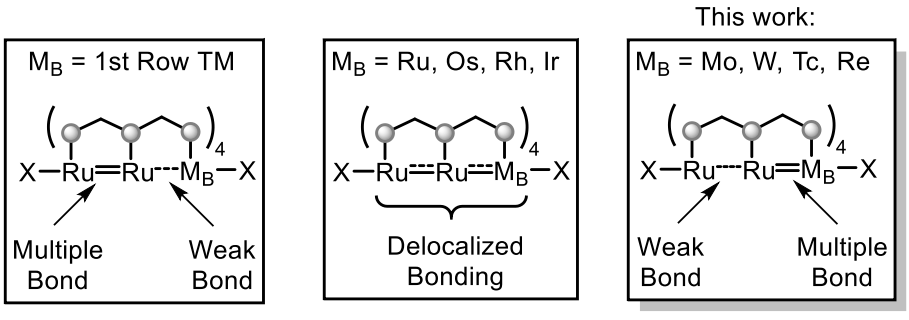

Figure1.1. 2. Changes in bonding trends across the series of Ru_2M_B compounds.

It is not unheard of for a heteronuclear bond to be stronger than the corresponding homonuclear bonds; perhaps the best known example is CO (bond dissociation energy, BDE, of 1075 kJ mol^{-1})[21] vs the gas phase C_2 (BDE = 605 kJ mol^{-1}) and O_2 dimers (BDE = 498 kJ mol^{-1}). More common is when one homonuclear bond is significantly weaker than the other, for example the interhalogen compound ICl (BDE = 213 kJ mol^{-1}) vs I_2 (BDE = 153 kJ mol^{-1}) and Cl_2 (BDE = 243 kJ mol^{-1}). For transition metal complexes, it is not possible to determine BDEs since one can't simply break one bond in a complex molecule. But examples of stable heterometallic bonds are known, as in Eq. 1 and 2, which proceed to form heterometallic products when heated.[22]

$Rh_2(TFA)_4 + Bi_2(TFA)_4 \rightarrow 2\ RhBi(TFA)_4$ Eq. 1.1.1

$Ru_2(TFA)_4 + Bi_2(TFA)_4 \rightarrow 2\ RuBi(TFA)_4$ Eq. 1.1.2

Here, TFA = the anion of trifluoroacetic acid. We describe the degree of heterometallic bonding in the series of compounds **1** – **8** here.

Section 2: Computational Details.

Calculations were performed using the ORCA program, version 5.0.0.[23] The B3LYP functional was used with the Def2-TZVP basis set on all atoms.[24-27] The D3 dispersion correction, as well as the resolution of identity and chain-of-spheres approximations were employed, using the D3 and RIJCOSX keywords respectively. The ZORA keyword was used to account for relativistic effects.[28, 29] The orbital interactions were analysed using the natural bonding orbital (NBO) package.[30, 31] Molecular orbitals were visualized using Chemcraft version 1.8.[32] To determine the correct spin state of each of these compounds,

geometry optimization was done on a range of possible spin states. Frequencies were calculated to ensure that the optimized structures correspond to energetic minima, and so that thermodynamic corrections to the electronic energy such that the tabulated energy differences correspond to Gibbs free energies.

Section 3: Results and Discussion

Geometries and Spin State Energetics.

Table 1.3.1 contains geometric information about the optimized structures of **1**-**3** and the cations **1**$^+$-**3**$^+$ as well as how they compare to experimental crystal structures. Notably, crystal structures have been obtained for **1**$^+$, **2**$^+$, **3**, and **3**$^+$. From the crystallographic data, it is clear that the cations prefer longer Ru_2–M_B distances. For example, while **2**$^+$ and **3** are isoelectronic, the Ru–Fe distance in **2**$^+$ is longer than the Ru–Co distance in 3 by 0.16 Å, consistent with a greater overall degree of electrostatic repulsion within the $[RuRuCo]^{7+}$ unit. Also, from the experimental data, oxidation of **3** to **3**$^+$ appears to involve oxidation of the Co center, based on the drastic shortening of the Co–Cl bond length by 0.24 Å upon oxidation. However, the Co–N bond lengths get slightly longer (~0.04 Å) upon oxidation, which is not expected for a Co-centered oxidation. It is important to note that there is little change in the Ru–Ru distance upon oxidation of **3** to **3**$^+$ (~0.02 Å), though Ru_2^{4+} and Ru_2^{5+} species often have similar Ru–Ru bond lengths, so this lack of change does not provide salient information about the site of oxidation.

The DFT geometry optimizations for **1-3 (**see Appendix for .xyz coordinates**)** and their cations showcase qualitative agreement with the above trends, showing for all six compounds longer Ru_2–M_B distances than the Ru–Ru distances indicating that the Ru_2 unit persists in all of these compounds. In the 4 compounds that have an experimental comparison, the Ru–Ru distances show very good agreement between the lowest energy spin state and the crystallographically determined distance. For **1**$^+$, **2**$^+$, **3**, and **3**$^+$**,** the Ru–M_B distances are also in quite good agreement, within ~0.02 Å. This highlights two aspects of this approach, one of which is a failing and one of which is useful. First it highlights the need for experimental conformation of DFT findings, due to DFT's difficulties in determining spin state energetics. However, the preservation of the Ru–Ru distances in these cases shows that this approach gives qualitatively correct geometries and may used as a predictive tool for complexes that exhibit different behaviors (see discussion of **4-8** below)

No magnetic susceptibility data for **1**$^+$, **2**$^+$, **3**, or **3**$^+$ have been recorded, so we must rely on comparison of the DFT optimized geometries with experimental geometries, and the calculated spin state energies to deduce the nature of the ground states. From the results in Table 1.3.1, we can see these complexes prefer high spin states between *S* = 5/2 in **3** to *S* = 4 in **1**$^+$. This indicates to us that these complexes are predicted to have ferromagnetic interactions between the Ru_2 core and the heterometal, leading to these elevated spin states. This ferromagnetic interaction requires strong bonding interactions, via an itinerant α-spin electron in the delocalized σ_{nb} orbital. Additionally, in these compounds where it is predicted that a primarily Ru-Ru core is maintained, the π^* and δ^* orbital occupations of this core can be used diagnostically to help differentiate between electron distribution A or

B. In A, you predict both π^* orbitals to be singly occupied with a doubly occupied δ^* orbital, and in electron configuration B, the δ^* orbital will also be singly occupied. For the lowest energy structures for **1**, **2**, **3** and $\mathbf{3}^+$ electron configuration A is predicted, however for the earlier metals in $\mathbf{1}^+$ and $\mathbf{2}^+$ electron configuration B is predicted (See Appendix for frontier orbitals)

Table 1.3.1. Comparison of geometries of optimized structures for 1-3 in various spin states with experimental crystallographic data.

Compound	3rd Metal	S =	Mayer BOs			Bond Lengths (Å)							Relative Energy (kcal mol^{-1})
			Ru_1-Ru_2	Ru_1-M	Ru_2-M	Ru_1-Ru_2	Ru_2-M	Ru_1-Cl	M-Cl	Ru_1-N (Avg)	Ru_2-N (Avg)	M-N (Avg)	
1	Mn	3/2	0.60	0.13	0.76	2.345	2.311	2.540	2.608	2.130	2.067	2.098	26.37
		5/2	0.62		0.33	2.361	2.481	2.560	2.497	2.126	2.040	2.114	25.59
		7/2	1.07		0.11	2.261	2.693	2.535	2.354	2.136	2.075	2.275	0.00
1$^+$	Mn	1	0.93	0.13	0.32	2.284	2.485	2.503	2.387	2.134	2.033	2.131	37.96
		2	0.48		0.49	2.371	2.397	2.474	2.460	2.128	2.037	2.127	23.54
		3	0.96		0.27	2.256	2.594	2.486	2.395	2.143	2.047	2.116	21.31
		4	1.07			2.273	2.734	2.469	2.336	2.129	2.037	2.270	0.00
Exp.		–	–	–	–	2.261[1]	2.718[2]	2.610[1]	2.151[2]	2.155[1]	2.027[2]	2.224[2]	–
2	Fe	1	1.00	0.20	0.42	2.317	2.416	2.770	2.804	2.134	2.045	2.057	28.17
		2	1.00		0.20	2.262	2.493	2.549	2.643	2.142	2.064	2.094	15.31
		3	1.00		0.20	2.266	2.564	2.524	2.363	2.136	2.073	2.212	0.00
2$^+$	Fe	1/2	1.02		0.15	2.265	2.531	2.478	2.588	2.135	2.031	2.105	15.29
		3/2	0.95		0.22	2.270	2.509	2.450	2.388	2.133	2.031	2.142	22.74
		5/2	1.00		0.17	2.266	2.543	2.479	2.567	2.136	2.030	2.109	14.96
		7/2	1.02		0.14	2.271	2.705	2.461	2.280	2.130	2.033	2.222	0.00
Exp.		–	–	–	–	2.283[3]	2.604[4]	2.564[2]	2.222[2]	2.070[2]	2.129[3]	2.169[2]	–
3	Co	1/2	1.00		0.19	2.254	2.449	2.533	2.607	2.147	2.061	2.043	15.98
		3/2	0.71		0.30	2.363	2.507	2.545	2.361	2.122	2.049	2.205	5.20
		5/2	1.00		0.20	2.267	2.549	2.518	2.344	2.137	2.070	2.186	0.00
Exp.		–	–	–	–	2.289(4)	2.449(6)	2.497(6)	2.43(1)	2.119[4]	2.040[3]	2.126[5]	–
3$^+$	Co	0	0.93		0.18	2.274	2.467	2.467	2.585	2.139	2.025	2.046	14.26
		1	1.05		0.14	2.267	2.601	2.461	2.313	2.131	2.035	2.182	6.44
		2	0.99		0.19	2.263	2.468	2.472	2.589	2.138	2.027	2.044	5.60
		3	1.03		0.14	2.270	2.612	2.459	2.308	2.131	2.033	2.183	0.00
Exp.		–	–	–	–	2.266[4]	2.614[8]	2.532[5]	2.190[8]	2.120[5]	2.018[4]	2.163[7]	–

The results of geometry optimizations for **4**-**8** and the cations **4**$^{+}$-**8**$^{+}$ are given in Table 1.3.2 (see Appendix for full comparisons of all investigated spin states). Analysis of the spin state energetics for **1**-**3** was important for calibrating our DFT method to experimental data, which is important because DFT often does not provide accurate spin state energies. With compounds **4**-**8**, we now apply these methods to unknown compounds for which there are no experimental data. Both **4** and **5** did not have unambiguously assignable ground spin states. For **4**, the S = 1 state was determined to be only 0.01 kcal/mol higher in energy than S = 0. Similarly for **5**, the S = ½ state was found to only be 0.49 kcal/mol higher in energy than S = 3/2. Otherwise, each heterometallic complex was calculated to have a well-isolated ground spin state, as listed in Table 2. Thus, our analysis will report on only the lowest-energy spin states, except for **4** and **5**, in which both these possible spin state options will be included, since, without experimental comparison, they are equally valid computational predictions at this level of theory.

In analyzing the geometries, it is useful to start with compound **8**. Os lies just below Ru on the periodic table, so we may expect **8** to have similar properties to the homometallic $Ru_3(dpa)_4Cl_2$. Indeed, this is the case. In **8**, the Ru–Ru and Ru–Os distances are practically equivalent at 2.29 and 2.28 Å, respectively. Oxidation of **8** to **8**$^{+}$ elongates both bonds, but to different extents. While the Ru–Os distance elongates by ~0.03 Å, the Ru–Ru distance elongates by 0.09 Å such that in **8**$^{+}$, the homometallic Ru–Ru distance is 0.06 Å longer than the heterometallic Ru–Os distance. This result was surprising, and has important implications for bonding.

All of the remaining compounds **4**-**7** and cations **4**$^{+}$-**7**$^{+}$ display the common feature that the Ru–Ru distances are longer than the heterometallic Ru–M_B distances. There is no straightforward trend of the difference, Δ*d*, with simple properties of M_B, such as electronegativity. We must therefore look into the bonding in these compounds to explain the surprising distance trends.

As a first step towards a bonding assessment, we have collected the calculated Mayer bond orders (MBO) for **4**-**8** and **4**$^{+}$-**8**$^{+}$ in Table 3. Remarkably, the Ru–M_B contact always has a greater MBO than the Ru–Ru contact, irrespective of metal, charge state, or spin state in the case of Mo and Tc. This is true even in the case of **8**, where the two metal-metal distances are practically identical. This indicates stronger bonding between Ru-M_B than Ru-Ru across the entire series. This is much different behavior than has previously been reported for any type of $M_AM_AM_B$ chain complex, contrasting distinctly with compounds **1**-**3** and **1**$^{+}$-**3**$^{+}$ described above.

Table 1.3.2. Optimized geometries of **4**-**8** and **4**$^{+}$-**8**$^{+}$.

				Mayer BOs			Bond Lengths (Å)							
Compound	**3rd Metal**	**Overall Charge**	***S* =**	**Ru_1-Ru_2**	**Ru_1…M**	**Ru_2-M**	**Ru_1-Ru_2**	**Ru_2-M**	**Ru_1-Cl**	**M-Cl**	**Ru_1-N (Avg)**	**Ru_2-N (Avg)**	**M-N (Avg)**	**Relative Energies (kcal mol^{-1})**
4	**Mo**	0	0	0.20	0.13	1.51	2.427	2.126	2.433	2.450	2.113	2.095	2.276	0
		0	1	0.25	0.35	1.22	2.399	2.223	2.524	2.537	2.117	2.098	2.262	0.01
5	**Tc**	0	1/2	0.23	0.12	0.97	2.353	2.189	2.497	2.490	2.127	2.085	2.184	0.49
		0	3/2	0.12	0.23	0.97	2.422	2.287	2.483	2.505	2.118	2.058	2.162	0
6	**W**	0	0	0.12	0.17	1.71	2.409	2.148	2.438	2.432	2.120	2.082	2.197	–
7	**Re**	0	1/2	0.37	0.38	1.60	2.366	2.198	2.528	2.478	2.129	2.085	2.165	–
8	**Os**	0	0	0.72	0.49	1.13	2.287	2.282	2.564	2.535	2.142	2.088	2.127	–
4^{+}	**Mo**	1	1/2	0.20	0.13	1.51	2.384	2.128	2.402	2.421	2.116	2.078	2.209	–
5^{+}	**Tc**	1	1	0.49	0.26	1.01	2.345	2.252	2.430	2.451	2.125	2.061	2.159	–
6^{+}	**W**	1	1/2	0.15	0.23	1.76	2.406	2.147	2.410	2.406	2.117	2.075	2.192	–
7^{+}	**Re**	1	0	0.26	0.34	1.73	2.352	2.137	2.389	2.369	2.125	2.073	2.169	–
8^{+}	**Os**	1	3/2	0.33	0.21	1.16	2.372	2.316	2.419	2.422	2.124	2.039	2.118	–

Bonding in 4-8.

With the unusual structural features and Mayer bond orders for the optimized geometries of **4**-**8** and $\mathbf{4}^{+}$-$\mathbf{8}^{+}$ analyzed indicating strong Ru-M bonds, we sought to further understand the nature of these interactions. To study this, we employed natural bonding orbital (NBO) analysis,[31, 33] a method that has been used before to analyze metal-metal multiple bonding,[34] but has never before been applied to the more difficult delocalized bonding situations found in HEMACs. In this method, both the alpha space and the beta space are assigned Lewis structure configurations. We can use these Lewis structure configurations to determine not only the bonding in the metal core, but also the oxidation states of the metals involved. We will start with the oxidation states of the metals, shown in table 1.3.3. These are determined by assigning which electrons are associated with the metal core through either being metal centered lone pairs, or metal-metal bonding pairs. From these assignments, we can assign oxidation states to each metal center in both the α and β spaces with lone pairs contributing all of their electrons to the metal center on which they reside, and by homolytically splitting the metal-metal bonding pairs, assigning one electron to each metal center involved. Then once the oxidation states of the α and β spaces are both computed, we take the sum of these electron counts to produce the oxidation states shown in table 1.3.3.

Table 1.3.3. Analysis of metal oxidation states in **4**-**9** and **4**$^{+}$-**9**$^{+}$.

Compound	Metal	Overall Charge	S=	Metal Oxidation State		
				Ru_1	Ru_2	M
4	**Mo**	0	0	2	4	2
		0	1	1.5	3.5	2
5	**Tc**	0	1/2	1.5	3.5	2
		0	3/2	2	2	2
6	**W**	0	0	2	4	4
7	**Re**	0	1/2	1.5	3.5	2
8	**Os**	0	0	2	3	1
9	**Zn**	0	1	2	2	2
4+	**Mo**	1	1/2	2	4	3
5+	**Tc**	1	1	2.5	3.5	2
6+	**W**	1	1/2	0	4	3
7+	**Re**	1	0	2	4	3
8+	**Os**	1	3/2	2	3	3
9+	**Zn**	1	3/2	2	3	2

Importantly, the $Ru_2M_B(dpa)_4Cl_2$ formula implies a $[RuRuM_B]^{6+}$ core charge for the metal atoms to account for the four dpa^- and two Cl^- anions. A glaring issue in Table 4 is that, with a few well-behaved exceptions, the oxidation states determined via this method do *not*

align with our preconceived notions of a total +6 charge for the metals in the neutral compounds, or a +7 charge in the cationic compounds. Excess oxidation of the core must therefore be accompanied by reduction of the dpa ligands. Many nitrogen donor ligands studied in the field of coordination chemistry are well-known to be redox active[35, 36] (or non-innocent), but this is previously unknown behavior of the dpa ligand. Surprised by this result, we undertook two sets of calculations to see if this effect was simply an artifact of the Lewis-like constraints of the NBO method. First, we examined $Ru_2Zn(dpa)_4Cl_2$ (**9,9**$^+$), which is a useful control because it should conform simply to the $[Ru_2]^{4+/5+}$–Zn^{2+} oxidation states with unpaired electrons only localized on the Ru_2 unit. Furthermore, $Ru_2Zn(dpa)_4Cl_2$ does not exhibit strong Ru–Zn bonding. Thus, the bonding in the Ru_2Zn system should be well-described by Lewis-like bonding depictions. We therefore can test the NBO method to determine if this approach can correctly describe the nature of M–M interactions in this simple system.

Indeed, we find that $Ru_2Zn(dpa)_4Cl_2$ is correctly described in this analysis, giving a d^{10} configuration around the Zn center in both the neutral and cationic species and as expected a Ru_2^{4+} and Ru_2^{5+} core, indicating that NBO analysis can correctly assess the diruthenium systems that have the expected Ru–Ru multiple bond and weak Ru–M_B interaction. As a second test, modeling of $Mo_2M_B(dpa)_4Cl_2$ complexes shows that the ligand reduction effect is not observed, (see Appendix for full details) suggesting that this ligand reduction may be not simply a computational artifact for the Ru system. It is likely a feature of the HEMAC systems that contain heavy, easily oxidized, early 2nd or 3rd row transition metals. Accessing these compounds experimentally will probably necessitate targeting

more highly oxidized $[Ru_2M_B]^{8+}$ or $[Ru_2M_B]^{9+}$ cores, or using ligands that are more difficult to reduce than the dpa ligand.

The other information that can be determined from the NBO analysis is the nature of the bonding in the metal core within a Lewis structure formalism. As described by Landis and Weinhold, bonding to transition metals makes use of the metal *nd* and (*n*+1)*s* orbitals to house 12 electrons (duodecet rule), which can be expanded to 18 electrons by the inclusion of three 3-center/4-electron bonding interactions.[37, 38] For paramagnetic species, the bonding interactions using these orbitals are by necessity different for the α and β electron sets. Thus, there will be different one-electron Lewis structures associated with the α and the β electron sets. The limiting Lewis-like structures involving metal-metal bonding for **4**-**9** and **4**$^+$-**9**$^+$ are shown in Figure 1.3.1. Though we have determined that each metal atom follows the duodecet rule, electrons involved in metal-ligand bonding are not shown in these diagrams.

The general trends observed in Figure 1.3.1 align with the evidence presented thus far, with the interaction between Ru and the heterometal showing at least a double bond, as opposed to the either fully non-bonding or singly-bonded Ru–Ru unit. The exception to this trend is the neutral Os compound **8**, with a double bond between the Ru atoms, though this bonding situation reverses upon oxidation to **8**$^+$. Previous studies on the triruthenium system have highlighted the unusual and partial multi-reference nature of this system. For completeness we also include the $Ru_2Zn(dpa)_4Cl_2$ results here as well, showing the expected behavior of an S = 1 Ru_2^{4+} group having a Ru=Ru double bond, and the Zn^{2+} ion being surrounded by 5 lone pairs (the d^{10} configuration). Worth noting here is that in many

of these “Lewis-like” structures of the metal core, the Ru atom distal to the heterometal is best described as Ru^{2+} and is not bonded to the other metals in the core, suggesting the possibility that given the correct reaction conditions this metal atom could be removed from the core using a relatively strong-field ligand (e.g. CN^-) to produce new Ru–M_B heterometallic metalloligands.

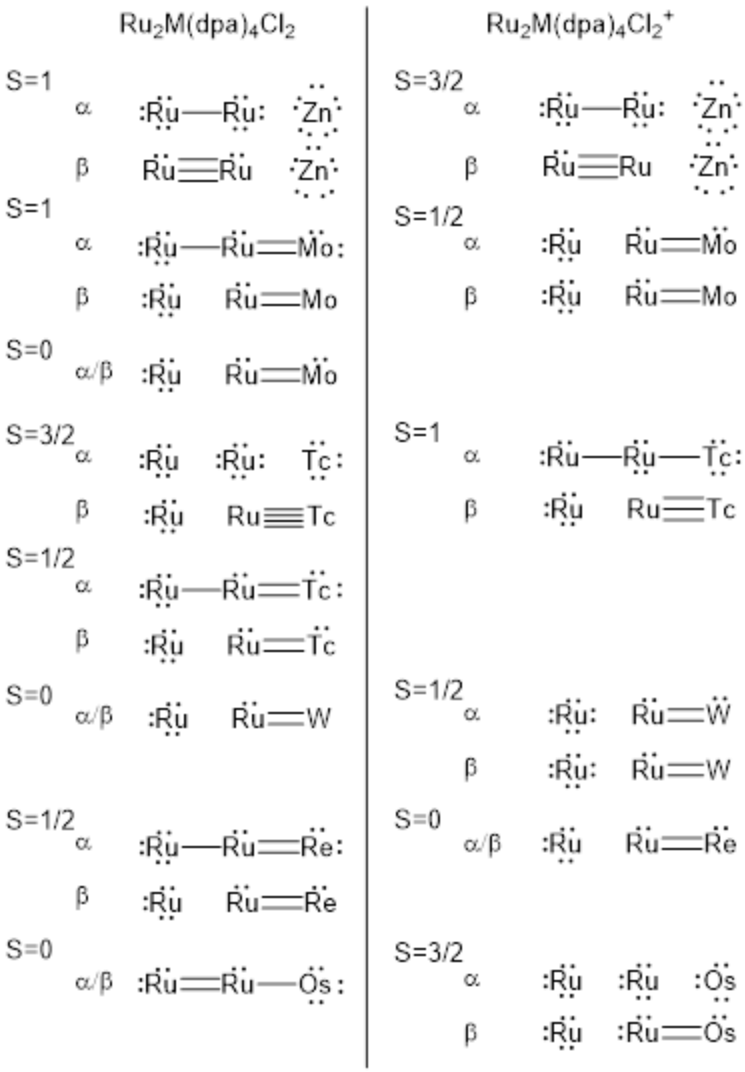

Figure 1.3.1. Limiting Lewis-like structures for the α and β sets of $Ru_2M_B(dpa)_4Cl_2$ compounds. For α or β diagrams, we draw pairs of dots and lines to conform to Lewis structure convention — however, since these are one-electron Lewis diagrams, each pair of dots indicates a single unshared electron, and each line indicates a single shared electron.

Conclusions

In this work, we have examined the structures and bonding in $Ru_2M_B(dpa)_4Cl_2$ HEMAC complexes, predicting high-spin ground states for cases in which M_B is a first-row transition

metal, and 5 complexes that create a stronger Ru–M_B bond (M = Mo, Tc, W, Re, Os) than the Ru–Ru bond in the Ru_2dpa_4Cl starting material. This conclusion is supported by the shorter Ru–M bond lengths compared to the Ru–Ru bond lengths, by the increase in Mayer bond order between the Ru–M interaction compared to the Ru–Ru interaction, and finally a NBO analysis of the compounds indicates Ru–M multiple bonding in the limiting Lewis-like structures. It is worth noting that the metal core in these complexes appears to be oxidized in this NBO analysis, with concurrent ligand reduction, but this behavior is not reproduced in systems of the form $Mo_2M(dpa)_4Cl$, suggesting such behavior is not a computational artifact. In conclusion, we believe that we have computationally predicted 4 reasonable synthetic targets (5 if you have a license to handle Tc) for precursors to new HEMAC compounds of the form $Ru_2M(dpa)_4Cl_2$ (M = Mo, Tc, W, Re, Os) which will certainly have application in molecular electronics due to their different predicted electronic structure from extant complexes, and may have further usefulness as precursors to HEMAC complexes of the form $M_ARuM_B(dpa)_4Cl_2$.

References.

(1) Parkin, G. *Structure and bonding. 136, metal-metal bonding*; Springer, 2010.

(2) Berry, J. F.; Lu, C. C. Metal–Metal Bonds: From Fundamentals to Applications. *Inorg. Chem.* **2017**, *56* (14), 7577-7581. DOI: 10.1021/acs.inorgchem.7b01330.

(3) Chipman, J. A.; Berry, J. F. Paramagnetic Metal–Metal Bonded Heterometallic Complexes. *Chem. Rev.* **2020**, *120* (5), 2409-2447. DOI: 10.1021/acs.chemrev.9b00540.

(4) Weng, T.; Debrincat, D.; Arcisauskaite, V.; McGrady, J. In search of structure–function relationships in transition-metal based rectifiers. *Inorg. Chem. Front.* **2014**, *1*. DOI: 10.1039/C4QI00038B.

(5) DeBrincat, D.; Keers, O.; McGrady, J. E. Can heterometallic 1-dimensional chains support current rectification? *Chem. Commun.* **2013**, *49* (80), 9116-9118, 10.1039/C3CC45063E. DOI: 10.1039/C3CC45063E.

(6) Nippe, M.; Berry, J. F. Introducing a Metal–Metal Multiply Bonded Group as an "Axial Ligand" to Iron: Synthetic Design of a Linear Cr−Cr···Fe Framework. *J. Am. Chem. Soc.* **2007**, *129* (42), 12684-12685. DOI: 10.1021/ja076337j.

(7) Cheng, M.-C.; Lee, G.-H.; Lin, T.-S.; Liu, Y.-C.; Chiang, M.-H.; Peng, S.-M. A new series of heteronuclear metal strings, MRhRh(dpa)$_4$Cl$_2$ and MRhRhM(dpa)$_4$X$_2$, from the reactions of Rh$_2$(dpa)$_4$ with metal ions of group 7 to group 12. *Dalton Trans.* **2021**, *50* (2), 520-534, 10.1039/D0DT03311A. DOI: 10.1039/D0DT03311A.

(8) Cheng, M.-C.; Hua, S.-A.; Lv, Q.; Sigrist, M.; Lee, G.-H.; Liu, Y.-C.; Chiang, M.-H.; Peng, S.-M. Stepwise synthesis of the heterotrimetallic chains [MRu$_2$(dpa)$_4$X2]$^{0/1+}$ using group 7 to group 12 transition metal ions and [Ru$_2$(dpa)$_4$Cl]. *Dalton Trans.* **2018**, *47* (5), 1422-1434, 10.1039/C7DT04114D. DOI: 10.1039/C7DT04114D.

(9) Nippe, M.; Turov, Y.; Berry, J. F. Remote Effects of Axial Ligand Substitution in Heterometallic Cr≡Cr···M Chains. *Inorg. Chem.* **2011**, *50* (21), 10592-10599. DOI: 10.1021/ic2011309.

(10) Wheaton, A. M.; Chipman, J. A.; Roy, M. D.; Berry, J. F. Metal–Metal Bond Umpolung in Heterometallic Extended Metal Atom Chains. *Inorg. Chem.* **2022**, *61* (38), 15058-15069. DOI: 10.1021/acs.inorgchem.2c02118.

(11) Stegman, S. W., A. M.; Nippe, M.; Berry, J. F. Manuscript in preparation.

(12) Chipman, J. A.; Berry, J. F. Extraordinarily Large Ferromagnetic Coupling (J≥150 cm^{-1}) by Electron Delocalization in a Heterometallic Mo≡Mo−Ni Chain Complex. *Chem. Eur. J.* **2018**, *24* (7), 1494-1499. DOI: https://doi.org/10.1002/chem.201704588 (acccessed 2025/08/20).

(13) Anderson, P. W.; Hasegawa, H. Considerations on Double Exchange. *Phys. Rev.* **1955**, *100* (2), 675-681. DOI: 10.1103/PhysRev.100.675.

(14) Anderson, P. W. Antiferromagnetism. Theory of Superexchange Interaction. *Phys. Rev.* **1950**, *79* (2), 350-356. DOI: 10.1103/PhysRev.79.350.

(15) Kanamori, J. Superexchange interaction and symmetry properties of electron orbitals. *J. Phys. Chem. Solids* **1959**, *10* (2), 87-98. DOI: https://doi.org/10.1016/0022-3697(59)90061-7.

(16) Kramers, H. A. L'interaction Entre les Atomes Magnétogènes dans un Cristal Paramagnétique. *Physica* **1934**, *1* (1), 182-192. DOI: https://doi.org/10.1016/S0031-8914(34)90023-9.

(17) Huang, G.-C.; Bénard, M.; Rohmer, M.-M.; Li, L.-A.; Chiu, M.-J.; Yeh, C.-Y.; Lee, G.-H.; Peng, S.-M. $Ru_2M(dpa)_4Cl_2$ (M = Cu, Ni): Synthesis, Characterization, and Theoretical Analysis of Asymmetric Heterometal String Complexes of the Dipyridylamide Family. *Eur. J.*

Inorg. Chem. **2008**, *2008* (11), 1767-1777. DOI: https://doi.org/10.1002/ejic.200701159 (acccessed 2025/08/20).

(18) Wu, B.-H.; Chung, J.-Y.; Hung, L.-Y.; Cheng, M.-C.; Peng, S.-M.; Chen, I. C. Facet-Dependent Reduction Reaction of Diruthenium Metal–String Complexes by Face-to-Face Linked Gold Nanocrystals. *ACS Omega* **2019**, *4* (3), 5327-5334. DOI: 10.1021/acsomega.9b00005.

(19) Wu, B.-H.; Lin, J.-Y.; Ho, K.-Y.; Huang, M.-J.; Hua, S.-A.; Cheng, M.-C.; Yang, Y.-W.; Peng, S.-M.; Chen, C.-h.; Chen, I. C. Determination of the Valence State of Diruthenium Moiety Using Redox Reactions and Surface-Enhanced Raman Scattering: Application in Heterometal Extended Metal-Atom Chain Diruthenium Nickel Complexes. *J. Phys. Chem. C* **2016**, *120* (36), 20297-20302. DOI: 10.1021/acs.jpcc.6b08351.

(20) Huang, P.-F.; Yang, H.-H.; Cheng, M.-C.; Peng, S.-M.; Chen, I. C. Thermoinduced Metal-to-Metal Charge Transfer in Trinuclear Metal String Complex $Ru_2M(dpa)_4Cl_2$ (M=Ni, Cu, dpa=Dipyridylamido). *ChemistrySelect* **2023**, *8* (1), e202203437. DOI: https://doi.org/10.1002/slct.202203437 (acccessed 2025/08/20).

(21) James Speight, N. L. *Lange's Handbook of Chemistry*; McGraw-Hill Education, 2017.

(22) Dikarev, E. V.; Gray, T. G.; Li, B. Heterobimetallic Main-Group–Transition-Metal Paddle-Wheel Carboxylates. *Angew. Chem. Int. Ed.* **2005**, *44* (11), 1721-1724. DOI: https://doi.org/10.1002/anie.200462433 (acccessed 2025/08/25).

(23) Neese, F. The ORCA program system. *WIREs Computational Molecular Science* **2012**, *2* (1), 73-78. DOI: https://doi.org/10.1002/wcms.81.

(24) Becke, A. D. Density-functional exchange-energy approximation with correct asymptotic behavior. *Phys. Rev. A* **1988**, *38* (6), 3098-3100. DOI: 10.1103/PhysRevA.38.3098.

(25) Perdew, J. P. Density-functional approximation for the correlation energy of the inhomogeneous electron gas. *Phys. Rev. B* **1986**, *33* (12), 8822-8824. DOI: 10.1103/PhysRevB.33.8822.

(26) Weigend, F. Accurate Coulomb-fitting basis sets for H to Rn. *Phys. Chem. Chem. Phys.* **2006**, *8* (9), 1057-1065, 10.1039/B515623H. DOI: 10.1039/B515623H.

(27) Weigend, F.; Ahlrichs, R. Balanced basis sets of split valence, triple zeta valence and quadruple zeta valence quality for H to Rn: Design and assessment of accuracy. *Phys. Chem. Chem. Phys.* **2005**, *7* (18), 3297-3305, 10.1039/B508541A. DOI: 10.1039/B508541A.

(28) Ch, C.; Pelissier, M.; Ph, D. Regular Two-Component Pauli-Like Effective Hamiltonians in Dirac Theory. *Phys. Scr.* **1986**, *34* (5), 394. DOI: 10.1088/0031-8949/34/5/007.

(29) van Lenthe, E.; Baerends, E. J.; Snijders, J. G. Relativistic total energy using regular approximations. *J. Chem. Phys.* **1994**, *101* (11), 9783-9792. DOI: 10.1063/1.467943 (acccessed 8/22/2025).

(30) *NBO 7.0*; Theoretical Chemistry Institute, University of Wisconsin, Madison, 2018. (accessed.

(31) Glendening, E. D.; Landis, C. R.; Weinhold, F. NBO 7.0: New vistas in localized and delocalized chemical bonding theory. *J. Comput. Chem.* **2019**, *40* (25), 2234-2241. DOI: https://doi.org/10.1002/jcc.25873 (acccessed 2025/08/22).

(32) *Chemcraft - graphical software for visualization of quantum chemistry computations. Version 1.8, build 682*. (accessed 2025 5/21).

(33) Weinhold, F.; Landis, C. R.; Glendening, E. D. What is NBO analysis and how is it useful? *Int. Rev. Phys. Chem.* **2016**, *35* (3), 399-440. DOI: 10.1080/0144235X.2016.1192262.

(34) Landis, C. R.; Weinhold, F. Origin of Trans-Bent Geometries in Maximally Bonded Transition Metal and Main Group Molecules. *J. Am. Chem. Soc.* **2006**, *128* (22), 7335-7345. DOI: 10.1021/ja060992u.

(35) England, J.; Scarborough, C. C.; Weyhermüller, T.; Sproules, S.; Wieghardt, K. Electronic Structures of the Electron Transfer Series $[M(bpy)_3]^n$, $[M(tpy)_2]^n$, and $[Fe(tbpy)_3]^n$ (M = Fe, Ru; n = 3+, 2+, 1+, 0, 1–): A Mössbauer Spectroscopic and DFT Study. *Eur. J. Inorg. Chem.* **2012**, *2012* (29), 4605-4621. DOI: https://doi.org/10.1002/ejic.201200232 (acccessed 2025/08/22).

(36) Ganguly, S.; Ghosh, A. Seven Clues to Ligand Noninnocence: The Metallocorrole Paradigm. *Acc. Chem. Res.* **2019**, *52* (7), 2003-2014. DOI: 10.1021/acs.accounts.9b00115.

(37) Landis, C. R.; Weinhold, F. 18-electron rule and the 3c/4e hyperbonding saturation limit. *J. Comput. Chem.* **2016**, *37* (2), 237-241. DOI: https://doi.org/10.1002/jcc.24001 (acccessed 2025/08/22).

(38) Weinhold, F.; Landis, C. R. *Valency and Bonding: A Natural Bond Orbital Donor-Acceptor Perspective*; Cambridge University Press, 2005. DOI: DOI: 10.1017/CBO9780511614569.

Chapter 2: Magnetic Exchange in a Dicobalt Paddlewheel Complex

Trey C. Pankratz, Caleb F. Harris, Ethan E. Hyland, Joshua K. Sailer, Amelia M. Wheaton, Huw M. L. Davies, and John F. Berry

TCP contributed to the BS-DFT studies and their subsequent analysis and catagorization of refences in the supoorting information in this work.

This work has been submitted to the New Journal of Chemistry and is currently under review.

Abstract: Dirhodium tetracarboxylate complexes catalyze a number of useful carbenoid transformations including cyclopropanation and C–H functionalization. However, complementary reactivity involving dicobalt tetracarboxylate complexes is significantly less developed; only cyclopropanation has been previously reported. The vast majority of dicobalt paddlewheel complexes reported to date have strongly coordinating N-donor axial ligands that are poisons known to arrest the catalytic activity of dirhodium complexes. We therefore sought a synthetic route to form dicobalt paddlewheel complexes that bear labile, O-donor axial ligands and report herein the synthesis of $Co_2(TPA)_4(L)_2$, where TPA = triphenylacetate and L = Et_2O (**2**) or THF (**3**), via two different synthetic routes. Magnetic susceptibility measurements of **3** have been performed and the data were fitted to a model incorporating isotropic exchange and zero-field splitting of the Co(II) centers. We reinvestigate the mechanism of magnetic exchange in paddlewheel-type Co(II) dimers finding that there are two direct exchange pathways of σ and π symmetry in addition to the

well-known δ symmetry superexchange pathway that is established for Cu(II) dimers. Complex **3** was successfully employed as a catalyst for carbenoid-type transformations using a diazo starting material, demonstrating utility in facilitating both cyclopropanation reactions and, for the first time, C–H functionalization.

Section 1:Introduction

Dirhodium tetracarboxylate complexes are well-known catalysts that facilitate a wide variety of bond-forming reactions. For example, carbenoid transformations that proceed via the intermediacy of a dirhodium carbene complex have been reported to yield cyclopropanation products, and even spectacularly selective insertions of carbenes into the C–H bond of alkanes.[1-15] A major goal in catalysis is to explore whether similar reactivity can be developed using metals that are cheaper and more Earth abundant than rhodium. In particular, cobalt attracted our attention because (1) cobalt and rhodium are both Group 9 metals, (2) mono-cobalt complexes have been explored as catalysts for a number of carbenoid transformations,[16-33] (3) a number of dicobalt tetracarboxylate structures have been reported,[34-68] (See Tables S1 and S2 in Appendix for a more detailed breakdown of these references) and (4) we recently reported that the dicobalt carboxylate compound $Co_2(esp)_2(EtOH)_2$ (esp = α,α,α',α'-tetramethyl-1,3-benzenedipropionate) can promote carbenoid styrene cyclopropanation,[55] though this catalyst was unable to perform C–H functionalization reactions.

With regard to the third point, of the known structures of paddlewheel-type Co_2 carboxylate dimers reported, ~85% of them contain nitrogen donor axial ligands such as pyridine or pyridine derivatives that are effective poisons for carbene transfer catalysts. Even the EtOH axial ligands in our reported $Co_2(esp)_2(EtOH)_2$ catalyst are carbene traps, as the carbene can insert into O–H bonds.

Another problem in the literature on Co_2 carboxylate dimers is that the lack of a strong Co–Co bond as a defining structural feature disfavors formation of dimers. Thus, while there are > 3,500 structures of Co carboxylate compounds in the Cambridge Database, < 40 are discrete dimeric structures. The propensity for mono-cobalt complexes was pointed out by Mehrotra and Bohra in their monograph on metal carboxylates[69], and it has been assumed that steric crowding is necessary to favor paddlewheel dimers. Compounding this issue is the fact that Co(II) is well known to display fast ligand exchange kinetics[70]. Thus, Co(II) carboxylates have been found to adopt a myriad of geometries other than the paddlewheel-type dimer structure.[55] For example, Kwon, Do, and co-workers have recently reported a Co(II) carboxylate coordination polymer in which the carboxylates display a combination of O,O'-bridging, O,O-bridging, O,O'-chelating, O,O,O'-triply-bridging, and monodentate coordination modes.[71] Furthermore, in previous work, we used the chelating dicarboxylate esp ligand, which we expected to circumvent this synthetic problem via the chelate effect, but we still found that other structure types were formed preferentially under certain reaction conditions.[55] Nevertheless, under the right synthetic conditions, we found that the paddlewheel-type dicobalt esp complex

could be formed, and, to our surprise, that it accommodated axial ligands such as ethanol and water,[54, 55] in contrast to the nitrogen donor ligands that have largely been used to support dicobalt paddlewheel structures in the past. carboxylic acid (pivalic acid) are initially combined to form an uncharacterized "polymeric material". This material is then treated with an excess of pyridine to form a dicobalt bridging aquo complex, which may then be dehydrated to yield the corresponding dicobalt paddlewheel dimer. Considering that there are numerous carboxylate-supported dicobalt bridging aquo complexes known,[55, 73-114] including some that do not contain N-donor supporting ligands, we wondered if this two-step synthetic sequence could be broadened to allow us to access a dicobalt paddlewheel-type structure with O-donor axial ligands. We report here preparation of the new complex $Co_2(TPA)_4(Et_2O)_2$ (**2**) via this route, where TPA = triphenylacetate, as well as synthesis of $Co_2(TPA)_4(THF)_2$ (**3**) using a single-step synthetic route directly from $CoCl_2$ using air free techniques. To our knowledge, **2** is the first Co_2 tetracarboxylate yet reported to contain diethyl ether axial ligands. Also, regarding compound **3**: the only other example of a Co_2 tetracarboxylate paddlewheel structure containing THF ligands is the complex $Co_2(O_2CCCo_3(CO)_9)_4(THF)_2$, in which the central Co atoms are derived from degradation of one of the carboxylate metalloligands. The new complexes reported here have been characterized crystallographically, and we report magnetic characterization on one of them as a representative example. In contrast to the well-studied Cu_2 tetracarboxylates, there are few reported magnetic measurements on paddlewheel-type Co_2 species.[115] Single-crystal magnetic susceptibility

measurements on Co_2(benzoate)$_4$(4-methyl-quinoline)$_2$ have suggested a dominating superexchange pathway involving interaction of δ-symmetry d_{xy} magnetic orbitals with the delocalized π system of the benzoate ligands.[116, 117] We reinvestigate the mechanism of magnetic exchange here, and present evidence for a strong direct exchange pathway involving overlap of the σ-symmetry Co(II) d_{z^2} orbitals. Electronic structure calculations support this proposal. Additionally, we report on carbene transfer reactivity of **3**. In addition to cyclopropanation, as has been reported for the $Co_2(esp)_2(EtOH)_2$ catalyst, **3** is capable of insertion of a carbene group into a C–H bond of cyclohexane. But, critically for catalytic applications, EtOH and water are both carbene traps. We have therefore continued to seek out straightforward synthetic methods to prepare dicobalt compounds with simple carboxylate ligands bearing labile, O-donor ligands that do not contain O–H groups in the axial sites. No such compounds have previously been reported.

We were therefore intrigued by a report from Golubnachaya and co-workers[72] outlining a stepwise synthetic procedure to form pyridine adducts of Co_2 tetracarboxylate paddlewheel compounds (Scheme 2.1.1). This method is a three-step process in which $Co(OAc)_2 \cdot 4H_2O$ and a carboxylic acid (pivalic acid) are initially combined to form an uncharacterized “polymeric material”. This material is then treated with an excess of pyridine to form a dicobalt bridging aquo complex, which may then be dehydrated to yield the corresponding dicobalt paddlewheel dimer.

Considering that there are numerous carboxylate-supported dicobalt bridging aquo complexes known,[55, 73-114] including some that do not contain N-donor supporting ligands, we wondered if this two-step synthetic sequence could be broadened to allow us to access a dicobalt paddlewheel-type structure with O-donor axial ligands. We report here preparation of the new complex $Co_2(TPA)_4(Et_2O)_2$ (**2**) via this route, where TPA = triphenylacetate, as well as synthesis of $Co_2(TPA)_4(THF)_2$ (**3**) using a single-step synthetic route directly from $CoCl_2$ using air free techniques. To our knowledge, **2** is the first Co_2 tetracarboxylate yet reported to contain diethyl ether axial ligands. Also, regarding compound **3**: the only other example of a Co_2 tetracarboxylate paddlewheel structure containing THF ligands is the complex $Co_2(O_2CCCo_3(CO)_9)_4(THF)_2$, in which the central Co atoms are derived from degradation of one of the carboxylate metalloligands. The new complexes reported here have been characterized crystallographically, and we report magnetic characterization on one of them as a representative example. In contrast to the well-studied Cu_2 tetracarboxylates, there are few reported magnetic measurements on paddlewheel-type Co_2 species.[115] Single-crystal magnetic susceptibility measurements on $Co_2(benzoate)_4(4\text{-methyl-quinoline})_2$ have suggested a dominating superexchange pathway involving interaction of δ-symmetry d_{xy} magnetic orbitals with the delocalized π system of the benzoate ligands.[116, 117] We reinvestigate the mechanism of magnetic exchange here, and present evidence for a strong direct exchange pathway involving overlap of the σ-symmetry Co(II) d_{z^2} orbitals. Electronic structure calculations support this proposal. Additionally, we report on carbene

transfer reactivity of **3**. In addition to cyclopropanation, as has been reported for the $Co_2(esp)_2(EtOH)_2$ catalyst, **3** is capable of insertion of a carbene group into a C–H bond of cyclohexane.

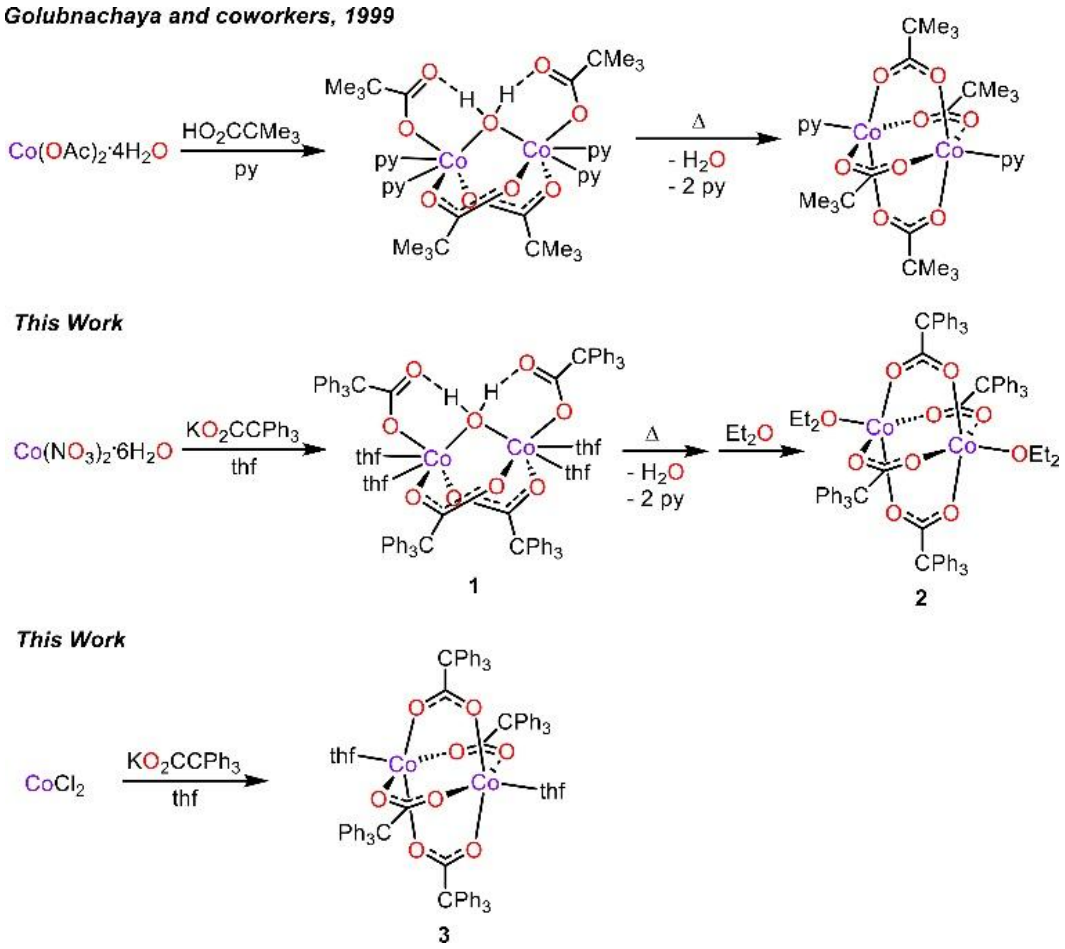

Scheme 2.1.1. *Preparation of dicobalt paddlewheel complexes. Top: Precedent from Golubnachaya and coworkers for the stepwise preparation of $Co_2(pivalate)_4(py)_2$ (py = pyridine). Middle: Modification of the Golubnachaya method for the preparation of $Co_2(triphenylacetate)_4(Et_2O)_2$ (**2**). Bottom: Direct synthesis of $Co_2(triphenylacetate)_4(thf)_2$ (**3**) using anhydrous, air-free conditions.*

Section 2: Results and discussion

Synthesis and structural characterization. The bridging aquo complex [Co_2(μ-OH_2)$(TPA)_4(THF)_4$], **1**, was synthesized in air by treating a THF solution of $Co(NO_3)_2{\cdot}6H_2O$ with two equivalents of the salt K(TPA). Subsequent crystallization from THF/hexanes provided **1** in 62% yield. The bridging water molecule of **1** was removed via azeotropic distillation in toluene and the resulting material was crystalized from Et_2O to afford X-ray quality crystals of [$Co_2(TPA)_4(Et_2O)_2$], **2**, with quantitative conversion. Attempts to crystalize **2** from hot MeOH led to the formation of the monomeric species $Co(TPA)_2(MeOH)_4$ (Figure S2 in Appendix).

Intrigued by the possibility of bypassing the bridging aquo intermediate by using strictly anhydrous conditions, we found that complex [$Co_2(TPA)_4(THF)_2$], **3**, could be synthesized in a single step by treating a suspension of K(TPA) in THF with 0.5 equivalent of anhydrous $CoCl_2$. The dark violet mixture was concentrated and filtered and pentane was added to precipitate a dichroic microcrystalline material that appeared both pink and blue under various lighting environments. The material was crystalized from vapor diffusion of benzene/pentane to provide X-ray quality crystals of **3** in 88% yield.

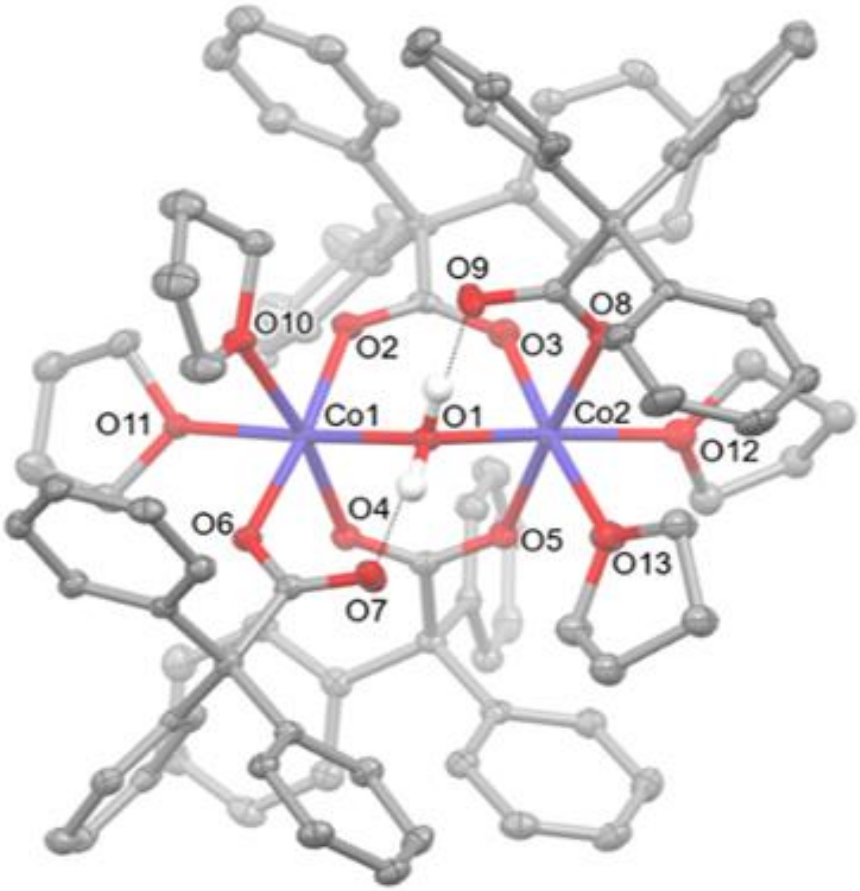

*Figure 2.1.1. Molecular structure of **1** with only the aquo hydrogen atoms shown and intramolecular hydrogen bonds highlighted with dotted lines. Thermal displacement ellipsoids are drawn at the 50% level.*

The two Co centers of **1** (Fig 2.2.1), with a non-bonded Co···Co distance of 3.489(2) Å, are linked through two anionic TPA ligands (Co–O, 2.0399(18)-2.0859(17) Å) and a bridging water molecule (Co–O, 2.0676(17), 2.0892(17) Å). The distorted octahedral environment around each Co(II) center is completed by coordination of two THF molecules (Co–O 2.116(5)-2.166(1) Å) and a terminal TPA anion (Co–O, 2.0640(17), 2.1096(17) Å). The uncoordinated O atoms of the two monodentate TPA

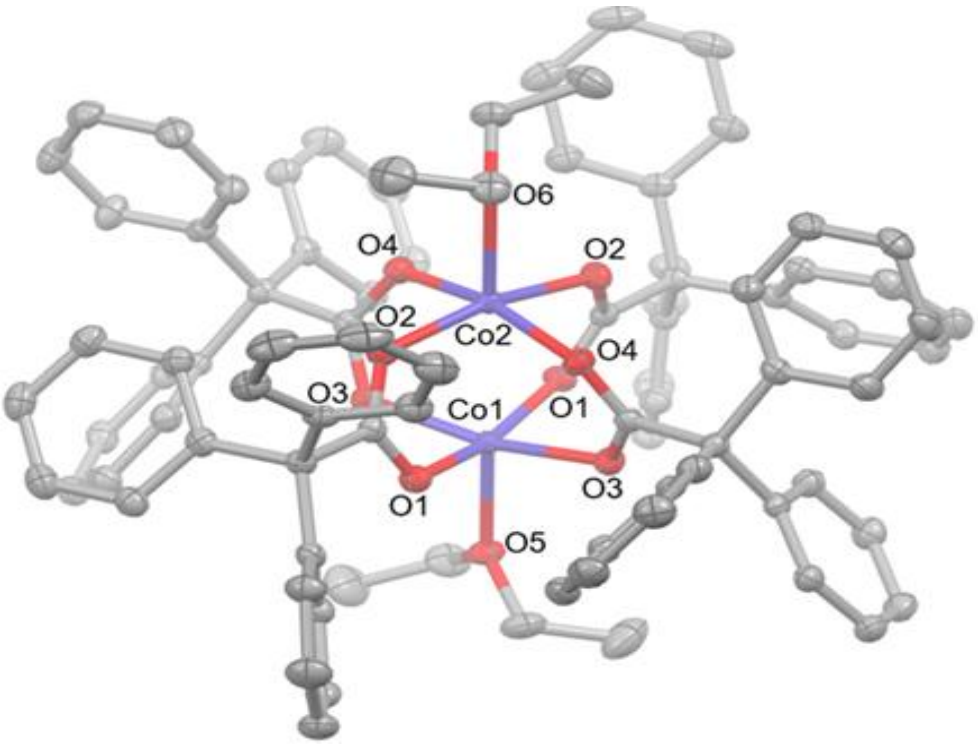

*Figure 3.2.2 Molecular structure of **2** with hydrogen atoms removed and thermal displacement ellipsoids drawn at the 50% level.*

ligands form short intramolecular hydrogen bonds with the hydrogen atoms of the bridging water molecule.

The binuclear paddlewheel complexes **2**, Figure 2.2.2, and **3**, Figure S3 in Appendix, are dimers with four bidentate and bridging TPA ligands between two Co^{II} centers. The two Co atoms possess non-bonding distances of 2.6175(10) and 2.6455(14) Å for **2** and **3**, respectively, in agreement with other reported tetracarboxylate Co paddlewheel structures,[34-68] which do not contain a Co–Co bond. The coordination geometry about each Co atom is distorted square pyramidal, with four O atoms from four different carboxylate ligands (Co–O, 2.0099(13) – 2.0331(11) Å) forming the basal plane and an O atom from a coordinated solvent molecule occupying the axial positions. In **2**, there are two axially coordinated Et_2O molecules

(Co–O, 2.0412(15), 2.0429(15) Å) and in **3** there are THF ligands (Co–O, 2.052(5), 2.054(5) Å). The Co–O axial bond lengths are notable in that they are slightly shorter than the average Co–O bond lengths for THF complexes, (2.11 Å, ranging from 1.97 – 2.45 Å), and Et_2O complexes, (2.08 Å, range from 1.99 – 2.12 Å), in all Co complexes found in the CSD. In contrast, Rh_2 tetracarboxylates bearing axial THF ligands have an average Rh–O distance of 2.29 Å, slightly longer than the average, 2.26 Å, of all Rh–THF complexes in the CSD. These comparisons indicate that the slight *trans* influence of the Rh–Rh bond in Rh_2 tetracarboxylates is absent in Co_2 tetracarboxylate structures. The UV-Vis spectra for complexes **2** and **3** are shown in Figure S4. These spectra are identical, displaying a multiplet of ligand field transitions centered at ~17,000 cm^{-1}. The similarity of the spectra indicate that the identity of the axial ligand does not affect the ligand field splitting in a meaningful way.

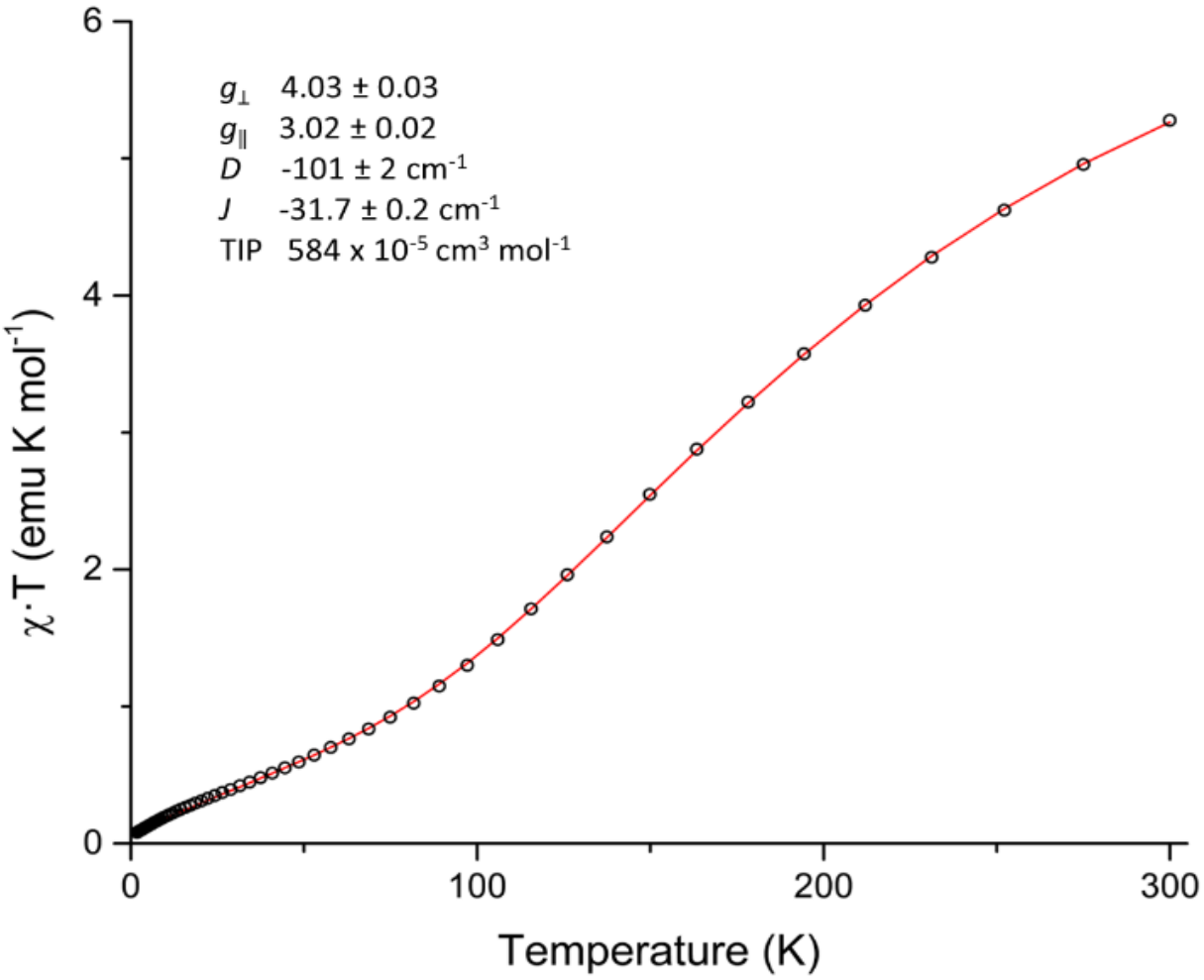

*Figure 2.3.1. Plot of χ·T vs T for **3**: the red line is a best fit to the data (black circles) using the model described in the text.*

Section 3:Magnetometry. Another significant difference between Co_2 and Rh_2 tetracarboxylates is that the former are paramagnetic while the latter complexes are diamagnetic. The electronic ground state configuration of the Rh_2 dimers is well described as $\sigma^2\pi^4\,\delta^2\delta^{*2}\pi^{*4}$; Rh_2 compounds are diamagnetic containing a $(d_{z^2} - d_{z^2})$ σ bond. In contrast, the Co atoms in **2** and **3** are too spatially separated to consider strong metal-metal interactions. Each Co(II) ion can therefore be considered as a five-coordinate, high-spin ion having a local spin of S_{Co} = 3/2. The spins of the two

Co(II) ions may couple ferromagnetically or antiferromagnetically. Previous literature examples indicate a preference for an antiferromagnetic spin-spin interaction.[118] A superexchange mechanism for spin coupling was proposed for Co_2(benzoate)$_4$(4-methylquinoline)$_2$ on the basis of single-crystal magnetic susceptibility measurements. The dominant mechanism of exchange was proposed to be via interaction of the δ-symmetry d_{xy} orbitals on the Co(II) ions with the delocalized π system of the benzoate ligands, resulting in a strong antiferromagnetic interaction. In order to test whether such a mechanism is applicable here, we probed the nature of the magnetic interaction in **3** using magnetic susceptibility measurements

Magnetic susceptibility data were measured for complex **3** from 1.8 – 300 K and a plot of χ·T vs. T is given in Figure 2.3.1. The room temperature χ·T value of ~5.3 emu K mol^{-1} is larger than expected for two non-interacting high-spin Co(II) centers (spin only χ·T = 3.75 emu K mol^{-1}), suggesting average *g* values greater than 2, as expected for d^7 Co(II) centers. The value of χ·T decreases monotonically with decreasing temperature and approaches a value of 0 emu K mol^{-1} at 1.8 K.

As shown in Fig. 2.3.1, the data were fitted to a model taking into account both axial zero-field splitting (*D*) of the two Co(II) ions and the antiferromagnetic exchange interaction (*J*) between them. This model provides g_{avg} = 3.69, D = −101 cm^{-1}, and J = −31.7 cm^{-1}, indicating a large zero-field splitting and antiferromagnetic coupling. Inclusion of an approximate 5% high spin impurity and a temperature independent paramagnetic (TIP) component improved the fit further. Notably, we do not find an acceptable fit of the data with D >0, suggesting that D is negative, similar to the

previously reported $Co_2(esp)_2(EtOH)_2$ (D = -55 cm^{-1}).[54] For comparison, we find the intramolecular exchange coupling (J) is over twice as large as that of $Co_2(esp)_2(EtOH)_2$ (-31.7 cm^{-1} vs -13.2 cm^{-1}). It is possible the exchange constant is higher in **3** than in the esp analog due to a shorter Co · · · Co distance (by 0.08 – 0.12 Å), suggestive of a direct orbital overlap exchange mechanism, rather than superexchange. This possibility was investigated computationally.

Section 4: Computational Studies. Broken symmetry density functional theory (BS-DFT) calculations were performed on two sets of structures to determine the nature of the orbitals involved in the magnetic exchange: a set of single point (SP) calculations for **2** and $Co_2(esp)_2(EtOH)_2$ frozen at the geometry of their crystal structures (crystallographic disorder precluded the use of such a geometry for **3**), and a set of geometry optimized structures for **2**, **3**, and $Co_2(esp)_2(EtOH)_2$ (Opt). The Opt structures are substantially displaced from the crystallographic (and therefore the SP structures) with the most notable changes being the Co-Co distances elongating from 2.7245(6) Å and 2.646(1) Å to 2.819 Å and 2.852 Å for $Co_2(esp)_2(EtOH)_2$ and **3**, respectively.

Despite differences in the J values computed for the SP and Opt structures (Table 2.4.1), all (other than $Co_2(esp)_2$opt, which becomes ferromagnetically coupled) are best described as containing a pair of antiferromagnetically-coupled high spin Co(II) ions.

	J (cm^{-1})	Co-Co (Å)	Avg. L-Co-Co (°)
$Co_2(esp)_2(EtOH)_2$ Exp.	-13.2 (±0.1)	2.7245(6)	162(3)
3 Exp.	-31.7 (±0.2)	2.646(1)	176.9(3)
$Co_2(esp)_2(EtOH)_2$ SP	-22	2.725	162
$Co_2(esp)_2(EtOH)_2$ Opt	4.75	2.819	145
2 SP	-112.18	2.618	180
2 Opt.	-36.45	2.819	172
3 Opt.	-33.87	2.852	169

Table 2.4.1 Selected experimental and computational bond lengths and coupling constants

To probe the nature of these antiferromagnetic interactions, we examined the magnetic orbitals for **2,** displayed in Figure 2.4.1.

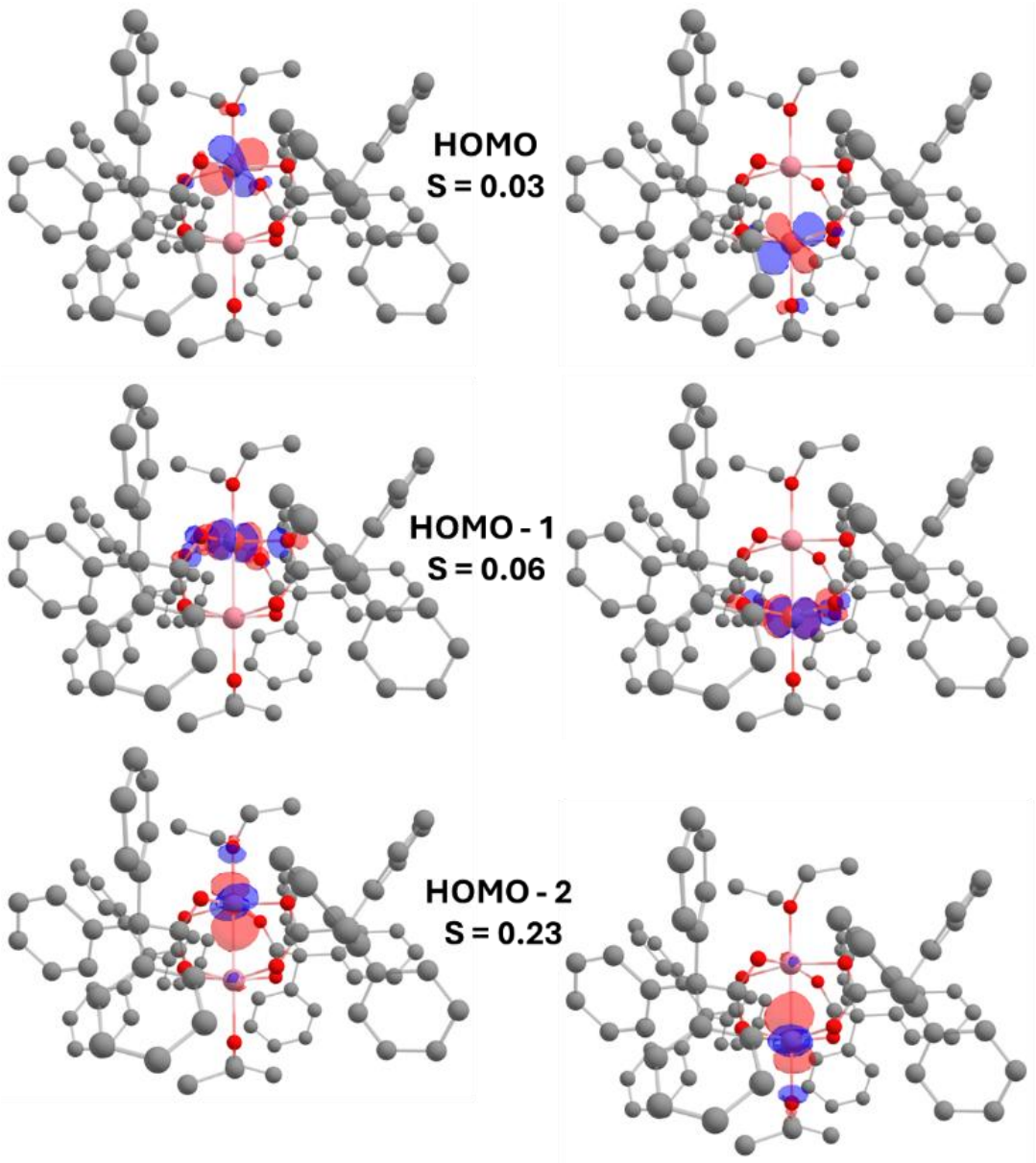

Figure 2.4.1. *Calculated magnetic orbitals from the single point calculations of* ***2*** *of both α (left) and β (right) spin. In between the pairs of orbitals are both the overlap integral S, and the orbital's position relative to the highest occupied molecular orbital (HOMO). Hydrogen atoms omitted for clarity. Grey = carbon, Red = oxygen, Salmon = Cobalt.*

There are show three distinct orbital interactions. The d_{xz} orbitals on each Co engage in a π symmetry interaction that contributes to a direct exchange interaction between the metal atoms. The δ symmetry $d_{x^2-y^2}$ orbitals show antibonding (out of phase) interactions with the carboxylate σ-symmetry orbitals, pointing to a superexchange mechanism, as seen for dicopper carboxylates.[119] There is also a third orbital interaction between d_{z^2} orbitals of σ symmetry, which is yet another direct exchange interaction. The nature of the magnetic orbitals in **2** are representative of the magnetic orbitals in **3**, and in $Co_2(esp)_2(EtOH)_2$. Notably, we do not find δ-symmetry d_{xy} magnetic orbitals, as postulated by Gerloch and coworkers.[120] The identity of the magnetic orbitals is invariant to whether we use SP or Opt geometries. However, the substantial structural changes that occur upon optimization, as can be see in **Table 2.4.1**, do have an impact on the predicted *J* values. The quantitative results of the BS-DFT on both Opt and SP structures are shown in **Table 2.4.1.**[121]

In contrast to the earlier proposed superexchange mechanism for Co_2 paddlewheel-type compounds, we find a combination of direct exchange and superexchange pathways for magnetic coupling between the two Co^{2+} ions.[54] In support of this idea, the exchange coupling parameter, *J*, shows two weak, but distinct, magneto-structural relationships in both the experimental and calculated structures. As Co-

Co distance decreases, the strength of the exchange coupling increases (see Appendix **S5**), and as the Co-Co-L angle (where L is the oxygen of the axial ligand) approaches 180°, the strength of the exchange coupling increases. (see Appendix **S6**).

This second effect has been previously observed in paddlewheel-type Ni_2 carboxylate systems as well, but not for Cu_2 carboxylates. Notably, paddlewheel-type Ni_2 carboxylates should also have the σ-d_{z^2} direct exchange and δ-$d_{x^2-y^2}$ superexchange pathways available to them, whereas Cu_2 complexes only display δ-$d_{x^2-y^2}$ superexchange.[45] We attribute both structural relationships seen here in the Co_2 system to the same underlying cause: changing either Co–Co distance or the Co–Co–L angle modify the overlap between the σ symmetry Co d_{z^2} orbitals and thereby increase the strength of the σ direct exchange component of the total magnetic exchange. This hypothesis is corroborated in our DFT model by the fact that the calculated orbital overlap of the d_{z^2} orbitals is heavily correlated (R^2 = 0.97) with the magnitude of the calculated total exchange coupling. (**Fig. 2.4.2.**)

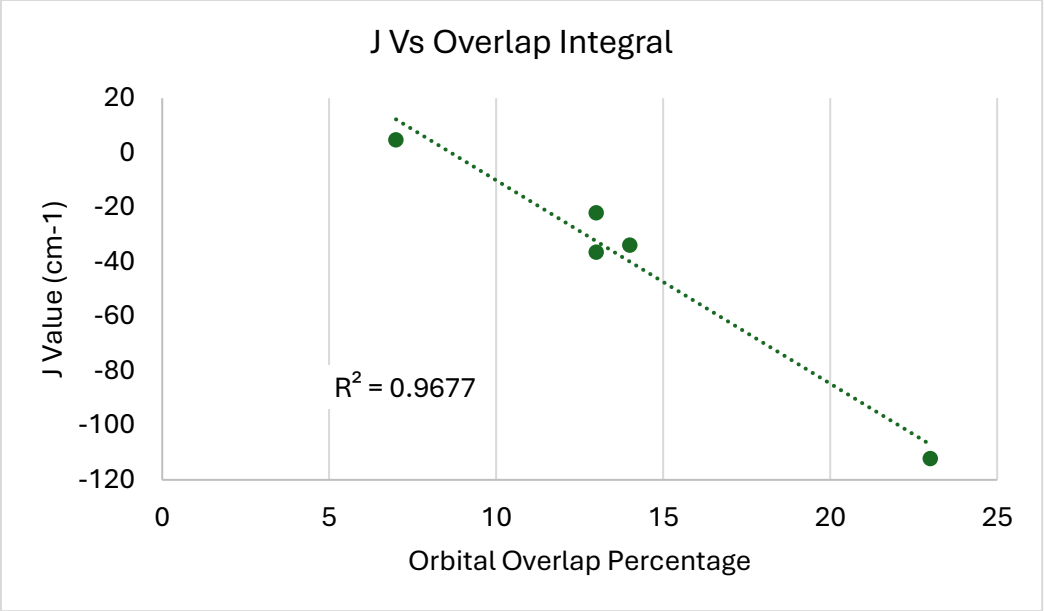

Figure 2.4.2. – Plot of exchange coupling values for calculated dicobalt complexes against the overlap integral for the HOMO-2, the t_2g-derived orbitals. A line of best fit, with the R^2 for the fit is shown in green.

Section 5: Catalytic Studies. We further investigated **3** as a catalyst for diazo decomposition reactions, and were particularly keen to test the ability to functionalize C–H bonds, since this type of reactivity has not been previously reported for Co_2 tetracarboxylates. Figure 2.5.1 displays the results of experiments aimed to assess the feasibility of catalytic cyclopropanation and C–H functionalization reactions. We chose the diazo ester trichloroethyl *p*-bromophenyldiazoacetate as a diazo substrate due to its ability to favor intermolecular reactions with exogenous substrates. In reactions with substrates

styrene (**5**) and 1-hexene (**4**), the cyclopropane products were observed in yields > 65% in the presence of 10 mol% **3**. These yields are comparable to the yield for styrene cyclopropanation by $Co_2(esp)_2(EtOH)_2$ and by "Co_2(*S*-TPPTTL)$_4$", which is presumed to have a paddlewheel type structure but was not crystallographically characterized.[55, 122] C–H functionalization reactions have not previously been reported for Co_2 tetracarboxylate catalysts. Nevertheless, cyclohexane (**6**) is functionalized by **3**, albeit in only 28% yield. Yields of reactions with substituted toluenes (**7,8**) indicate that benzylic C–H functionalization is favored with more electron-rich substrates, indicating an electrophilic Co-carbene intermediate. However, *p*-dimethylaminotoluene (**9**) showed no reactivity, likely due to poisoning of the catalyst by the amine groups. Reactions with competition substrates, 1-isopropyl-4-methylbenzene (**11**) and 1-ethyl-4-methylbenzene (**10**) yielded mixtures of products, indicating a lack of inherent selectivity for specific C–H bonds. This lack of selectivity is not surprising, considering that Rh_2 C–H functionalization catalysts require very bulky supporting ligands to affect differentiation between primary, secondary, and tertiary C–H bonds.[120, 123-125] Even though it is promising that the dicobalt catalysts are capable of catalyzing C-H functionalization reactions with aryldiazoacetates, they are still far less reactive than the corresponding dirhodium catalysts, which have been shown to be capable of achieving high yields of C-H functionalization at catalyst loading as low as 0.001 mol%.[126]

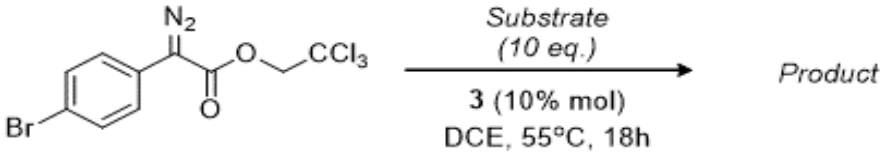

Substrate	Product
 **4**	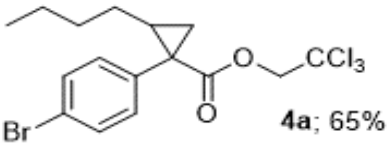 **4a**; 65%
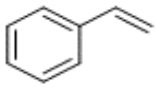 **5**	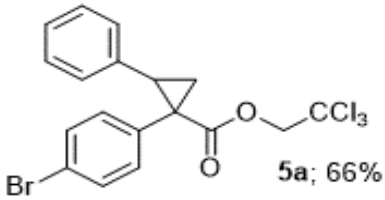 **5a**; 66%
 **6**	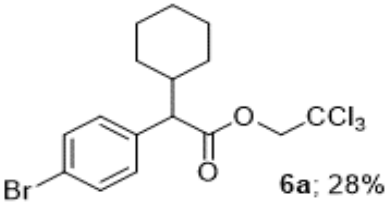 **6a**; 28%
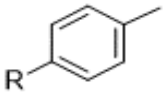 **7**: R = Br **8**: R = OMe **9**: R = NMe_2	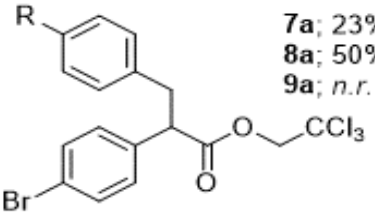 **7a**; 23% **8a**; 50% **9a**; *n.r.*
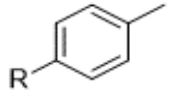 **10**: R = Et **11**: R = *i*Pr	Intractable mixture of C-H activation products

*Figure 2.5.1. Results of diazo decomposition in the presence of **3** (10% mol) and substrates **4** – **11** (10 eq.). Yields reported are that of isolated products.*

Conclusions

We have reported the synthesis and characterization of new dinuclear Co carboxylate complexes containing labile *O*-donor axial ligands. Importantly, we have been able to use this method to prepare Co_2 complexes with labile THF and diethyl ether axial ligands, which are important for catalytic studies because they are not carbene traps. The magnetic properties and their temperature dependence demonstrate an antiferromagnetic interaction between the two Co atoms in the paddlewheel structures, which is distinct from Rh_2 analogues that contain a formal Rh–Rh bond. We have analyzed the magnetic properties in terms of three magnetic exchange interactions, two that involve direct exchange (σ and π symmetry), and the δ-symmetry superexchange pathway that is well known from Cu_2 carboxylates. In contrast to early studies on Co_2(benzoate)$_4$(4-methylquinoline)$_2$ in which a d_{xy} superexchange mechanism for spin coupling was postulated, we find the d_{z^2} direct exchange mechanism to be more dominant. The Co_2 complex **3** was studied with respect to catalytic applications involving C–H functionalization and cyclopropanation reactions with diazo starting materials. These catalysts were poisoned by the presence of strongly coordinating *N*-donating groups such as pyridine or acetonitrile, demonstrating the importance of labile axial ligands for catalyst efficacy. Further work to determine the generalizability of this synthetic approach is underway toward the development of other catalysts for C–H functionalization that employ Earth abundant metals.

Experimental

Materials and Methods

All reagents were obtained from commercial sources and used as received, except as noted. All work was performed with oven-dried glassware under a dry, nitrogen atmosphere using standard Schlenk technique, except as noted. Anhydrous THF was distilled under nitrogen and stored over 4 Å molecular sieves for at least 48 h prior to use.

Synthetic Procedures

K[(TPA)]. In air, triphenylacetic acid (2.88 g; 10.0 mmol) was dissolved in THF (35 mL) at ambient temperature. To this solution, a separately prepared solution of KOtBu (1.12 g; 10.0 mmol) in THF (50 mL) was added over 5 mins. Slight heat was sometimes necessary to completely dissolve all base before transferring. Once completely transferred, a thick white precipitate formed, and the stirring was increased to ensure thorough mixing. The mixture was allowed to stir for 15 mins at ambient temperature and then filtered. The white solid was washed with Et_2O (2 x 30 mL), air dried, then placed under vacuum at r.t. for 16 h before using in the next step without further purification (3.06 g; 9.36 mmol; 94% yield).

$[Co_2(\mu\text{-}OH_2)(TPA)_4(THF)_4]$, (1). In air, K(TPA) (653 mg; 2.00 mmol) was suspended in THF (20mL). To this mixture, a solution of $Co(NO_3)_2 \cdot 6H_2O$ (183 mg; 1.00 mmol) in THF (20 mL) was added dropwise over ~5 mins. The suspension was allowed to stir

for 16h at ambient temperature before being filtered. The solid was washed with THF until the washings ran colorless and then the filtrate was concentrated to dryness. The residue was reconstituted in a minimal amount of THF and layered with hexanes, providing X-ray quality crystals after 2 days (489 mg; 62% yield). Analysis calc'd for $C_{96}H_{94}Co_2O_{13}$: C, 73.27%; H, 6.02%. Found: C, 73.05%; H, 6.11%.

$[Co_2(TPA)_4(Et_2O)_2]$, (2). In air, **1** (393 mg; 0.250 mmol) was dissolved in toluene (10 mL) and then heated to reflux for 0.5 h resulting in a slight color change from dark burgundy to violet. The solution was then cooled and concentrated to dryness. Upon addition of Et_2O (~5-10 mL), spontaneous crystallization occurred providing a nearly quantitative conversion of **1** to **2**. Analysis calc'd for $C_{88}H_{80}Co_2O_{10}$: C, 74.67%; H, 5.70%. Found: C, 74.79%; H, 5.61%. MS (MALDI-TOF) *m/z* calc'd for $C_{80}H_{60}Co_2O_8$ [M – $2(Et_2O)]^+$: 1266.3; found 1266.6.

$[Co_2(TPA)_4(THF)_2]$, (3). $CoCl_2$ (130 mg; 1.00 mmol) was partially dissolved in anhydrous THF (12 mL). This suspension was transferred via pipette into a suspension of K(TPA) (653 mg; 2.00 mmol) in THF (10 mL) resulting in a dark violet-blue colored mixture that was allowed to stir at ambient temperature for 16 h. The reaction mixture was then filtered, and washed with THF until the washings ran colorless. The filtrate was concentrated to ~3 mL and then pentane (~15 mL) was added to while stirring to precipitate a dichroic microcrystalline solid. The material was collected by filtration and crystalized from vapor diffusion of benzene/pentane

to provide X-ray quality crystals (621 mg; 88% yield). Analysis calc'd for $C_{88}H_{76}Co_2O_{10}$: C, 74.89%; H, 5.43%. Found: C, 74.72%; H, 5.49%. MS (MALDI-TOF) *m/z* calc'd for $C_{80}H_{60}Co_2O_8$ $[M - 2(THF)]^+$: 1266.3; found 1266.7.

Catalytic Reactions

General Procedure 1. To a flame dried vial equipped with a stir bar and 4Å MS (100 weight%) under inert atmosphere was added trap (10 equiv). Then, **3** (25.2 mg, 10 mol%) was dissolved in DCE (2 mL) and added to the vial. The solution was heated to 55 °C. Finally, trichloroethyl p-bromophenyldiazoacetate (78.4 mg, 0.200 mmol) was dissolved in DCE (2 mL) and was added via syringe pump over a period of 2 h. The reaction was left for 18 h after the addition of the diazo compound. After the allotted time, the reaction was passed over a small silica plug, concentrated, and purified via column chromatography to yield the desired product.

2,2,2-trichloroethyl (1S,2S)-1-(4-bromophenyl)-2-butylcyclopropane-1-carboxylate, (4a). General procedure 1 was employed for the cyclopropanation of 1-hexene (250 µL, 2.0 mmol) with trichloroethyl p-bromophenyldiazoacetate (78.4 mg, 0.200 mmol) and **3** (25.2 mg, 10 mol%) as catalyst. Purification by column chromatography (0-18% diethyl ether/hexane) affording the product as a colorless oil (55.5 mg, 65%). Spectra matched reported literature precedent.[127] ^{1}H NMR (400 MHz, $CDCl_3$) δ 7.48 (d, J = 8.4 Hz, 2H), δ 7.21 (d, J = 8.5 Hz, 2H), δ 4.82 (1H, J = 11.9 Hz, 1H), δ 4.58 (d, J = 11.9 Hz, 1H), δ 1.97 (tdd, J = 8.8, 6.6, 4.4 Hz, 1H), δ 1.89 (dd, J = 9.0, 4.1 Hz), δ 1.39 (tdd, J = 10.4, 7.8, 5.3 Hz, 3H), δ 1.28 (m, 2H), δ 1.21 (dd, J = 6.8, 4.2 Hz, 1H), δ 0.86 (t, J = 7.3 Hz, 3H), δ 0.61 (m, 1H).

2,2,2-trichloroethyl (1S,2R)-1-(4-bromophenyl)-2-phenylcyclopropane-1-carboxylate, (5a). General procedure 1 was employed for the cyclopropanation of styrene (230 µL, 2.0 mmol) with trichloroethyl p-bromophenyldiazoacetate (78.4 mg, 0.200 mmol) and 3 (25.2 mg, 10 mol%) as catalyst. Purification by column chromatography (0-18% diethyl ether/hexane) affording the product as a colorless oil (59.3 mg, 66%). Spectra matched reported literature precedent.[128] ^{1}H NMR (400 MHz, $CDCl_3$) δ 7.29 (m, 2H), δ 7.14 (m, 2H), δ 6.97 (d, J = 8.5 Hz, 2H), δ 6.83 (m, 2H), δ 4.86 (d, J = 11.9 Hz, 1H), δ 4.67 (d, J = 11.9 Hz, 1H), δ 3.25 (dd, J = 9.4, 7.5 Hz, 1H), δ 2.31 (dd, J = 9.4, 5.2 Hz, 1H), δ 2.00 (dd, J = 7.5, 5.2 Hz, 1H).

2,2,2-trichloroethyl 2-(4-bromophenyl)-2-cyclohexylacetate (6a). General procedure 1 was employed for the C–H insertion of cyclohexane (220 µL, 2.0 mmol) with trichloroethyl p-bromophenyldiazoacetate (78.4 mg, 0.200 mmol) and **3** (25.2 mg, 10 mol%) as catalyst. Purification by column chromatography (0-3% diethyl ether/hexane) affording the product was a colorless oil (24.1 mg, 28%). Spectra matched reported literature precedent.[126] ^{1}H NMR (600 MHz, $CDCl_3$**)** δ 7.47 (d, J = 8.5 Hz, 2H), 7.26 (d, J = 8.4 Hz, 2H), 4.78 (d, J = 12.0 Hz, 1H), 4.65 (d, J = 12.0 Hz, 1H), 3.37 (d, J = 10.7 Hz, 1H), 2.08 (qt, J = 11.1, 3.4 Hz, 1H), 1.89 (dtd, J = 10.5, 3.7, 1.7 Hz, 1H), 1.78 (dtd, J = 13.3, 3.6, 1.8 Hz, 1H), 1.66 (m, 2H), 1.35(m, 2H), 1.15 (m, 3H), 0.79 (m, 1H).

2,2,2-trichloroethyl 2,3-bis(4-bromophenyl)propanoate, (7a). General procedure 1 was employed for the C–H insertion of 1-bromo-4-methylbenzene (342 mg, 2.0 mmol) with trichloroethyl p-bromophenyldiazoacetate (78.4 mg, 0.200 mmol) and **3** (25.2 mg, 10 mol%) as catalyst. Purification by column chromatography (0-3% diethyl ether/hexane) affording the product was a colorless oil (24.1 mg, 23%). Spectra matched reported literature

precedent.[129] ^{1}H NMR (400 MHz, $CDCl_3$) δ 7.45 (d, J = 8.4 Hz, 2H), 7.23 (d, J = 8.5 Hz, 2H), 7.04 (d, J = 8.7 Hz, 2H), 6.78 (d, J = 8.7 Hz, 2H), 4.82 (d, J = 11.9 Hz, 1H), 4.69 (d, J = 12.0 Hz, 1H), 3.93 (dd, J = 8.6, 7.0 Hz, 1H), 3.76 (s, 3H), 3.40 (dd, J = 13.6, 5.0 Hz, 1H), 3.03 (dd, J = 13.9, 7.0 Hz, 1H).

2,2,2-trichloroethyl 2-(4-bromophenyl)-3-(4-methoxyphenyl)propanoate, (8a). General procedure 1 was employed for the C–H insertion of 1-methoxy-4-methylbenzene (250 µL, 2.0 mmol) with trichloroethyl p-bromophenyldiazoacetate (78.4 mg, 0.200 mmol) and **3** (25.2 mg, 10 mol%) as catalyst. Purification by column chromatography (0-3% diethyl ether/hexane) affording the product was a colorless oil (46.8 mg, 50%). Spectra matched reported literature precedent.[130] ^{1}H NMR (400 MHz, $CDCl_3$) δ 7.45 (d, J = 8.4 Hz, 1H), 7.36 (d, J = 8.4 Hz, 1H), 7.20 (d, J = 8.5 Hz, 1H), 7.00 (d, J = 8.4 Hz, 1H), 4.68 (d, J = 12.0 Hz, 1H), 4.64 (d, J = 12.0 Hz, 1H), 3.92 (dd, J = 8.5, 7.2 Hz, 1H), 3.39 (dd, J = 13.9, 8.5 Hz, 1H), 3.03 (dd, J = 13.9, 7.2 Hz, 1H).

Electronic Structure Calculations

Calculations were performed using the ORCA program, version 5.0.0.[131] The B3LYP functional was used with the Def2-TZVP basis set on all atoms.[132-135] The D3 dispersion correction, as well as the resolution of identity and chain-of-spheres approximations were employed, using the D3 and RIJCOSX keywords respectively.[136, 137] For both **2** and **$Co_2esp_2(EtOH)_2$** the crystallographic coordinates were used for the single point geometries, the .xyz coordinates used can be found in the SI. These crystallographic coordinates were also employed in the geometry optimizations conducted on these structures. **3** used the

geometry of the equatorial ligands and metal core, with the THF ligands being added to the axial positions. The broken symmetry formalism was used to model the electronic structure of **2** and **$Co_2esp_2(EtOH)_2$** with 3 α and 3 β weakly interacting electrons. These interactions were analysed using the corresponding orbital transformation.[138] The Yamaguchi method was used for the prediction of *J* in both complexes, with the results given in Table 1.[139, 140] Molecular orbitals were visualized using Chemcraft version 1.8.[141]

Instrumentation

Mass spectral data were collected using a Bruker ULTRAFLEX III MALDI-TOF mass spectrometer equipped with a SmartBeam laser. IR spectra were collected on a Bruker Tensor 27 FTIR spectrometer using the ATR technique. Elemental analyses were measured at Midwest Microlab, LLC in Indianapolis, Indiana, USA.

X-ray Crystallography

Crystallographic data were measured at the Molecular Structure Laboratory of the Chemistry Department of the University of Wisconsin-Madison. Crystals were selected under oil under ambient conditions and attached to the tip of a MiTeGen MicroMount. Each crystal was mounted in a stream of cold nitrogen at 100(1) K and centered in the X-ray beam using a video camera. The crystal evaluation and data

collection were performed on a Bruker Quazar SMART APEX-II diffractometer with Cu Kα (λ = 1.54178 Å) or Mo K_α (λ = 0.71073 Å) radiation. The data were collected using a routine to survey an entire sphere of reciprocal space and indexed by the SMART program. The structures were solved using the Olex2 program via direct methods or charge flipping and refined by iterative cycles of least-squares refinement on F^2 followed by difference Fourier synthesis. All H atoms were included in the final structure factor calculation at idealized positions and allowed to ride on the neighboring atoms with relative isotropic displacement coefficients, except as noted.

Crystallographic data have been deposited with the Cambridge Crystallographic Data Center under CCDC 2370354-2370357.

Magnetic Susceptibility Measurements

Samples were handled with glass and plastic tools to avoid contamination from metallic materials. Crystalline samples were placed in a glass vial with a glass ball bearing and ground into powders using a vortex mixer. The powdered samples were weighed and placed inside of plastic capsules mounted in plastic drinking straws. Variable-temperature DC magnetization was measured using a Quantum Design MPMS 3 SQUID magnetometer over a temperature range of 2–300 K at an applied magnetic field of 1000 G (0.1 T). Magnetization data were converted to magnetic susceptibility via $\chi \approx M/H$. The data were fitted using the PHI software program.[142] Diamagnetic corrections[143] for each sample were calculated using the equation:

$$\chi_{dia} \approx -\frac{\mathrm{MW}}{2} \text{ x } 10^{-6} \text{ emu mol}^{-1}$$

and were applied to the experimental data along with a correction for the intrinsic diamagnetism of the sample holder. Magnetic susceptibility data were additionally corrected for temperature independent paramagnetism.

Notes and references

1. H. M. L. Davies and E. G. Antoulinakis, in *Organic Reactions*, DOI: https://doi.org/10.1002/0471264180.or057.01, pp. 1-326.
2. H. M. L. Davies and E. G. Antoulinakis, *J. Organomet. Chem.*, 2001, **617-618**, 47-55.
3. H. M. L. Davies and R. E. J. Beckwith, *Chem. Rev.*, 2003, **103**, 2861-2904.
4. H. M. L. Davies and J. R. Denton, *Chem. Soc. Rev.*, 2009, **38**, 3061-3071.
5. H. M. L. Davies and J. R. Manning, *Nature*, 2008, **451**, 417-424.
6. H. M. L. Davies and D. Morton, *Chem. Soc. Rev.*, 2011, **40**, 1857-1869.
7. M. P. Doyle, *Chem. Rev.*, 1986, **86**, 919-939.
8. M. P. Doyle and D. C. Forbes, *Chem. Rev.*, 1998, **98**, 911-935.
9. J. Hansen and H. M. L. Davies, *Coord. Chem. Rev.*, 2008, **252**, 545-555.
10. K. P. Kornecki, J. F. Briones, V. Boyarskikh, F. Fullilove, J. Autschbach, K. E. Schrote, K. M. Lancaster, H. M. L. Davies and J. F. Berry, *Science*, 2013, **342**, 351-354.

11. H. Lebel, J. F. Marcoux, C. Molinaro and A. B. Charette, *Chem. Rev.*, 2003, **103**, 977-1050.

12. G. A. Sulikowski, K. L. Cha and M. M. Sulikowski, *Tetrahedron: Asymmetry*, 1998, **9**, 3145-3169.

13. T. Ye and M. A. McKervey, *Chem. Rev.*, 1994, **94**, 1091-1160.

14. H. M. L. Davies, *J. Org. Chem.*, 2019, **84**, 12722-12745.

15. H. M. L. Davies and K. Liao, *Nat. Rev. Chem.*, 2019, **3**, 347-360.

16. Y. Chen, K. B. Fields and X. P. Zhang, *J. Am. Chem. Soc.*, 2004, **126**, 14718-14719.

17. A. Chirila, M. B. Brands and B. de Bruin, *J. Catal.*, 2018, **361**, 347-360.

18. W. I. Dzik, X. Xu, X. P. Zhang, J. N. H. Reek and B. de Bruin, *J. Am. Chem. Soc.*, 2010, **132**, 10891-10902.

19. W. I. Dzik, X. P. Zhang and B. de Bruin, *Inorg. Chem.*, 2011, **50**, 9896-9903.

20. R. F. J. Epping, M. M. Hoeksma, E. O. Bobylev, S. Mathew and B. de Bruin, *Nat. Chem.*, 2022, **14**, 550-557.

21. Y. Hu, K. Lang, J. Tao, M. K. Marshall, Q. Cheng, X. Cui, L. Wojtas and X. P. Zhang, *Angew. Chem., Int. Ed.*, 2019, **58**, 2670-2674.

22. T. Ikeno, I. Iwakura and T. Yamada, *J. Am. Chem. Soc.*, 2002, **124**, 15152-15153.

23. D. Intrieri, A. Caselli and E. Gallo, *Eur. J. Inorg. Chem.*, 2011, **2011**, 5071-5081.

24. W.-C. C. Lee, D.-S. Wang, C. Zhang, J. Xie, B. Li and X. P. Zhang, *Chem*, 2021, **7**, 1588-1601.

25. H. Lu, W. I. Dzik, X. Xu, L. Wojtas, B. de Bruin and X. P. Zhang, *J. Am. Chem. Soc.*, 2011, **133**, 8518-8521.

26. B. W. Musselman and N. Lehnert, *Chem. Commun.*, 2020, **56**, 14881-14884.

27. H. Pellissier and H. Clavier, *Chem. Rev.*, 2014, **114**, 2775-2823.

28. A. Penoni, R. Wanke, S. Tollari, E. Gallo, D. Musella, F. Ragaini, F. Demartin and S. Cenini, *Eur. J. Inorg. Chem.*, 2003, **2003**, 1452-1460.

29. J. V. Ruppel, X. Cui, X. Xu and X. P. Zhang, *Org. Chem. Front.*, 2014, **1**, 515-520.

30. C. te Grotenhuis and B. de Bruin, *Synlett*, 2018, **29**, 2238-2250.

31. N. P. van Leest, F. J. de Zwart, M. Zhou and B. de Bruin, *JACS Au*, 2021, **1**, 1101-1115.

32. M. Zhou, M. Lankelma, J. I. van der Vlugt and B. de Bruin, *Angew. Chem., Int. Ed.*, 2020, **59**, 11073-11079.

33. S. Zhu, J. A. Perman and X. P. Zhang, *Angew. Chem., Int. Ed.*, 2008, **47**, 8460-8463.

34. H. Abu Ali, A. Abu Shamma and S. Kamel, *J. Mol. Struct.*, 2017, **1142**, 40-47.

35. M. Affronte, I. Casson, M. Evangelisti, A. Candini, S. Carretta, C. A. Muryn, S. J. Teat, G. A. Timco, W. Wernsdorfer and R. E. P. Winpenny, *Angew. Chem., Int. Ed.*, 2005, **44**, 6496-6500.

36. P. A. Ajibade, G. A. Kolawole, P. O'brien, J. Raftery and M. Helliwell, *J. Coord. Chem.*, 2008, **61**, 328-340.

37. N. Benbellat, K. S. Gavrilenko, Y. Le Gal, O. Cador, S. Golhen, A. Gouasmia, J.-M. Fabre and L. Ouahab, *Inorg. Chem.*, 2006, **45**, 10440-10442.

38. M. Benslimane, Y. K. Redjel, G. Denes and H. Merazig, *Acta Crystallogr., Sect. E:Struct. Rep. Online*, 2013, **69**, m517-m518.

39. S. A. Boer, W. Cao, B. K. Glascott and D. R. Turner, *Chemistry*, 2020, **2**, 613-625.

40. J. Catterick, M. B. Hursthouse, P. Thornton and A. J. Welch, *J. Chem. Soc., Dalton Trans.*, 1977, DOI: 10.1039/DT9770000223, 223-226.

41. E.-Y. Choi, K. Park, C.-M. Yang, H. Kim, J.-H. Son, S. W. Lee, Y. H. Lee, D. Min and Y.-U. Kwon, *Chem. - Eur. J.*, 2004, **10**, 5535-5540.

42. H. Chun, H. Jung and J. Seo, *Inorg. Chem.*, 2009, **48**, 2043-2047.

43. Y. Cui, F. Zheng and J. Huang, *Acta Crystallogr., Sect. C:Struct. Chem.*, 1999, **55**, 1067-1069.

44. J. E. Davies, A. V. Rivera and M. Sheldrick, *Acta Crystallogr., Sect. B:Struct. Sci., Cryst. Eng. Mater.*, 1977, **33**, 156-158.

45. N. V. Gogoleva, G. G. Aleksandrov, A. A. Pavlov, M. A. Kiskin, A. A. Sidorov and I. L. Eremenko, *Russ. J. Coord. Chem.*, 2018, **44**, 91-102.

46. A. J. Gosselin, C. A. Rowland, K. P. Balto, G. P. A. Yap and E. D. Bloch, *Inorg. Chem.*, 2018, **57**, 11847-11850.

47. S. A. Hilderbrand and S. J. Lippard, *Inorg. Chem.*, 2004, **43**, 5294-5301.

48. T. Hokelek, E. G. Saglam, B. Tercan, O. Aybirdi and H. Necefoglu, *Acta Crystallogr., Sect. E:Crystallogr. Commun.*, 2011, **67**, m28-m29.

49. N. Klein, I. Senkovska, I. A. Baburin, R. Grünker, U. Stoeck, M. Schlichtenmayer, B. Streppel, U. Mueller, S. Leoni, M. Hirscher and S. Kaskel, *Chem. - Eur. J.*, 2011, **17**, 13007-13016.

50. S. W. Lee, H. J. Kim, Y. K. Lee, K. Park, J.-H. Son and Y.-U. Kwon, *Inorg. Chim. Acta*, 2003, **353**, 151-158.

51. H. Li, Y. Yang, X. Jing, C. He and C. Duan, *Chem. - Asian J.*, 2021, **16**, 1237-1244.

52. G. R. Lorzing, A. J. Gosselin, B. A. Trump, A. H. P. York, A. Sturluson, C. A. Rowland, G. P. A. Yap, C. M. Brown, C. M. Simon and E. D. Bloch, *J. Am. Chem. Soc.*, 2019, **141**, 12128-12138.

53. S. E. Nefedov, E. S. Chernetsova, A. A. Sidorov, S. L. Ioffe, I. L. Eremenko and I. I. Moiseev, *Proc. Nat. Acad. Sci. USSR*, 2001, **377**, 645.

54. R. J. Pakula and J. F. Berry, *Dalton Trans.*, 2018, **47**, 13887-13893.

55. R. J. Pakula, A. M. Martinez, E. A. Noten, C. F. Harris and J. F. Berry, *Polyhedron*, 2019, **161**, 93-103.

56. I.-H. Park, H. Ju, T. S. Herng, Y. Kang, S. S. Lee, J. Ding and J. J. Vittal, *Cryst. Growth Des.*, 2016, **16**, 7278-7285.

57. Y. Qi and Y. Wang, *Inorg. Chem. Commun.*, 2013, **35**, 83-85.

58. B.-W. Qin, B.-L. Zhou, Z. Cui, L. Zhou, X.-Y. Zhang, W.-L. Li and J.-P. Zhang, *CrystEngComm*, 2019, **21**, 1564-1569.

59. J. Qin, F. L. Xue, N. Lei, Q.-L. Ren, D.-Y. Wang and H.-L. Zhu, *Acta Chim. Slov.*, 2014, **61**, 170-176.

60. J.-Q. Shen, P.-Q. Liao, D.-D. Zhou, C.-T. He, J.-X. Wu, W.-X. Zhang, J.-P. Zhang and X.-M. Chen, *J. Am. Chem. Soc.*, 2017, **139**, 1778-1781.

61. P. Sikiti, C. X. Bezuidenhout, D. P. van Heerden and L. J. Barbour, *Inorg. Chem.*, 2019, **58**, 8257-8262.

62. H. E. Skipper, C. V. May, A. L. Rheingold, L. H. Doerrer and M. Kamenetska, *J. Am. Chem. Soc.*, 2021, **143**, 16439-16447.

63. D.-H. Wang, X. Li and X.-G. Liu, *Acta Crystallogr., Sect. E:Struct. Rep. Online*, 2004, **60**, m703-m704.

64. Y. Wang and Z. Zhou, *J. Solid State Chem.*, 2015, **228**, 117-123.

65. G. F. S. Whitehead, J. Ferrando-Soria, L. Carthy, R. G. Pritchard, S. J. Teat, G. A. Timco and R. E. P. Winpenny, *Dalton Trans.*, 2016, **45**, 1638-1647.

66. Q. Yao, J. Sun, K. Li, J. Su, M. V. Peskov and X. Zou, *Dalton Trans.*, 2012, **41**, 3953-3955.

67. Z. Zhang, L. Zhang, L. Wojtas, M. Eddaoudi and M. J. Zaworotko, *J. Am. Chem. Soc.*, 2012, **134**, 928-933.

68. R. Zou, P.-Z. Li, Y.-F. Zeng, J. Liu, R. Zhao, H. Duan, Z. Luo, J.-G. Wang, R. Zou and Y. Zhao, *Small*, 2016, **12**, 2334-2343.

69. R. C. M. a. R. Bohra, *Metal Carboxylates*, Academic Press, London, 1983.

70. H. Taube, *Chemical Reviews*, 1952, **50**, 69-126.

71. J. Kang, M. J. Lee, N. G. Oh, J. Shin, S. J. Kwon, H. Chun, S.-J. Kim, H. Yun, H. Jo, K. M. Ok and J. Do, *Chem. Mater.*, 2021, **33**, 2804-2813.

72. M. A. Golubnichaya, A. A. Sidorov, I. G. Fomina, L. T. Eremenko, S. E. Nefedov, I. L. Eremenko and Moiseev, II, *RUSSIAN JOURNAL OF INORGANIC CHEMISTRY*, 1999, **44**, 1401-1410.

73. P. Alborés and E. Rentschler, *Dalton Trans.*, 2009, DOI: 10.1039/B820594A, 2609-2615.

74. G. Aromí, A. S. Batsanov, P. Christian, M. Helliwell, A. Parkin, S. Parsons, A. A. Smith, G. A. Timco and R. E. P. Winpenny, *Chem. - Eur. J.*, 2003, **9**, 5142-5161.

75. D. A. Brown, W. K. Glass, N. J. Fitzpatrick, T. J. Kemp, W. Errington, G. J. Clarkson, W. Haase, F. Karsten and A. H. Mahdy, *Inorg. Chim. Acta*, 2004, **357**, 1411-1436.

76. J. C. Burley and T. J. Prior, *Acta Crystallogr., Sect. E:Struct. Rep. Online*, 2005, **61**, m1422-m1424.

77. M. Fontanet, M. Rodríguez, X. Fontrodona, I. Romero, F. Teixidor, C. Viñas and N. Aliaga-Alcalde, *Dalton Trans.*, 2016, **45**, 10916-10927.

78. K. S. Hagen, R. Lachicotte and A. Kitaygorodskiy, *J. Am. Chem. Soc.*, 1993, **115**, 12617-12618.

79. K. S. Hagen, R. Lachicotte, A. Kitaygorodskiy and A. Elbouadili, *Angew. Chem., Int. Ed.*, 1993, **32**, 1321-1324.

80. S.-C. Hsu, P.-S. Chiang, H.-K. Liu, S.-H. Lo and C.-H. Lin, *J. Chin. Chem. Soc.*, 2012, **59**, 18-27.

81. J. Hudák, R. Boča, J. Moncol and J. Titiš, *Inorg. Chim. Acta*, 2013, **394**, 401-409.

82. L. L. Johnston, K. A. Brown, D. P. Martin and R. L. LaDuca, *J. Mol. Struct.*, 2008, **882**, 80-87.

83. A. Karmakar, R. J. Sarma and J. B. Baruah, *Eur. J. Inorg. Chem.*, 2007, **2007**, 643-647.

84. S. Kennedy, G. Karotsis, C. M. Beavers, S. J. Teat, E. K. Brechin and S. J. Dalgarno, *Angew. Chem., Int. Ed.*, 2010, **49**, 4205-4208.

85. M. A. Kiskin, G. G. Aleksandrov, A. S. Bogomyakov, V. M. Novotortsev and I. L. Eremenko, *Inorg. Chem. Commun.*, 2008, **11**, 1015-1018.

86. J. Kühnert, T. Rüffer, P. Ecorchard, B. Bräuer, Y. Lan, A. K. Powell and H. Lang, *Dalton Trans.*, 2009, DOI: 10.1039/B821407G, 4499-4508.

87. C.-S. Liu, J.-J. Wang, L.-F. Yan, Z. Chang, X.-H. Bu, E. C. Sañudo and J. Ribas, *Inorg. Chem.*, 2007, **46**, 6299-6310.

88. L.-F. Ma, L.-Y. Wang, M. Du and S. R. Batten, *Inorg. Chem.*, 2010, **49**, 365-367.

89. Q. Miao, M.-L. Hu and F. Chen, *Acta Crystallogr., Sect. E:Struct. Rep. Online*, 2004, **60**, m1314-m1316.

90. E. E. Moushi, A. Kourtellaris, I. Spanopoulos, M. J. Manos, G. S. Papaefstathiou, P. N. Trikalitis and A. J. Tasiopoulos, *Cryst. Growth Des.*, 2015, **15**, 185-193.

91. K. Müller, M. Korb, C. Koo, R. Klingeler, D. Miesel, A. Hildebrandt, T. Rüffer and H. Lang, *Polyhedron*, 2017, **138**, 185-193.

92. P. Nockemann, B. Thijs, K. V. Hecke, L. V. Meervelt and K. Binnemans, *Cryst. Growth Des.*, 2008, **8**, 1353-1363.

93. J. Overgaard, J. P. S. Walsh, V. R. Hathwar, M. R. V. Jørgensen, C. Hoffman, J. A. Platts, R. Piltz and R. E. P. Winpenny, *Inorg. Chem.*, 2014, **53**, 11531-11539.

94. F. Papi, A. Rosado, O. Vallcorba, A. E. Lanza, M. Gemmi, N. Portolés-Gil, A. M. López-Periago, C. Domingo and J. A. Ayllón, *Cryst. Growth Des.*, 2022, **22**, 4463-4471.

95. S. Perontsis, E. Geromichalou, F. Perdih, A. G. Hatzidimitriou, G. D. Geromichalos, I. Turel and G. Psomas, *J. Inorg. Biochem.*, 2020, **212**, 111213.

96. F. P. Pruchnik, U. Dawid and A. Kochel, *Polyhedron*, 2006, **25**, 3647-3652.

97. Y. A. Satskaya, N. P. Komarova, K. S. Gavrilenko, O. V. Manoylenko, M. A. Kiskin, S. V. Kolotilov, I. L. Eremenko and V. M. Novotortsev, *Russ. Chem. Bull.*, 2015, **64**, 630-635.

98. C. Shen, T. Sheng, Q. Zhu, S. Hu and X. Wu, *CrystEngComm*, 2012, **14**, 3189-3198.

99. J.-B. Shen, X.-Y. Wu, X.-J. Chen and G.-L. Zhao, *Acta Crystallogr., Sect. E:Struct. Rep. Online*, 2011, **67**, m558-m559.

100. S. Singh, D. Saini, S. K. Mehta and D. Choquesillo-Lazarte, *J. Coord. Chem.*, 2011, **64**, 1544-1553.

101. Z. Tomkowicz, S. Ostrovsky, S. Foro, V. Calvo-Perez and W. Haase, *Inorg. Chem.*, 2012, **51**, 6046-6055.

102. U. Turpeinen, M. Ahlgren and R. Hamalainen, *Acta Crystallogr., Sect. B:Struct. Sci., Cryst. Eng. Mater.*, 1982, **38**, 1580-1583.

103. U. Turpeinen, R. Hamalainen and M. Ahlgren, *Acta Crystallogr., Sect. A*, 1984, **40**, C303.

104. U. Turpeinen, R. Hämäläinen and J. Reedijk, *Polyhedron*, 1987, **6**, 1603-1610.

105. S. Vanicek, H. Kopacka, K. Wurst, S. Vergeiner, L. Oehninger, I. Ott and B. Bildstein, *Zeitschrift für anorganische und allgemeine Chemie*, 2015, **641**, 1282-1292.

106. X. Wang, G. Liu, B. Chen, Y. Bi and H. Lin, *J. Coord. Chem.*, 2008, **61**, 1635-1644.

107. X.-L. Wang, Y.-Q. Chen, G.-C. Liu, H.-Y. Lin, W.-Y. Zheng and J.-X. Zhang, *J. Organomet. Chem.*, 2009, **694**, 2263-2269.

108. X.-L. Wang, L.-L. Hou, J.-W. Zhang, G.-C. Liu and H.-Y. Lin, *Polyhedron*, 2013, **61**, 65-72.

109. C.-S. Wu, B.-S. Zhang, Y.-X. Li and J.-P. Qiu, *Zeitschrift für Kristallographie - New Crystal Structures*, 2014, **229**, 303-304.

110. B. Xu, P. Cen and D. Tian, *Inorg. Chem. Commun.*, 2020, **116**, 107912.

111. N. Xu, X.-H. Qiu, C. Wang, J. Tang, P. Cheng and D.-Z. Liao, *Inorg. Chem. Commun.*, 2013, **36**, 122-125.

112. Z.-X. Xu, M.-F. Shi, Y. Wan and X. Gu, *Polyhedron*, 2022, **224**, 116001.

113. B.-Y. Zhang, T.-G. Xu and D.-J. Xu, *Acta Crystallogr., Sect. E:Struct. Rep. Online*, 2006, **62**, m2186-m2188.

114. I. Zimmermann, T. D. Keene, A. Neels and S. Decurtins, *Acta Crystallogr., Sect. E:Struct. Rep. Online*, 2008, **64**, m845-m846.

115. O. Kahn, *Molecular Magnetism*, Wiley, 1993.

116. P. D. W. Boyd, J. E. Davies and M. Gerloch, *Proc. R. Soc. London, Ser. A*, 1978, **360**, 191-210.

117. P. D. W. Boyd, M. Gerloch, J. H. Harding and R. G. Woolley, *Proc. R. Soc. London, Ser. A*, 1978, **360**, 161-189.

118. J. Hudák, R. Boča, Ľ. Dlháň, J. Kožíšek and J. Moncoľ, *Polyhedron*, 2011, **30**, 1367-1373.

119. M. Gerloch, J. H. Harding and J. H. Lewis, *Proc. R. Soc. London, Ser. A*, 1978, **360**, 211-227.

120. W. Liu, Z. Ren, A. T. Bosse, K. Liao, E. L. Goldstein, J. Bacsa, D. G. Musaev, B. M. Stoltz and H. M. L. Davies, *J. Am. Chem. Soc.*, 2018, **140**, 12247-12255.

121. Due to high disorder in the crystal of 2, single point calculations were not attempted.

122. J. K. Sailer, J. C. Sharland, J. Bacsa, C. F. Harris, J. F. Berry, D. G. Musaev and H. M. L. Davies, *Organometallics*, 2023, **42**, 2122-2133.

123. K. Liao, T. C. Pickel, V. Boyarskikh, J. Bacsa, D. G. Musaev and H. M. L. Davies, *Nature*, 2017, **551**, 609-613.

124. K. Liao, Y.-F. Yang, Y. Li, J. N. Sanders, K. N. Houk, D. G. Musaev and H. M. L. Davies, *Nat. Chem.*, 2018, **10**, 1048-1055.

125. C. Qin and H. M. L. Davies, *J. Am. Chem. Soc.*, 2014, **136**, 9792-9796.

126. Z. Ren, T. L. Sunderland, C. Tortoreto, T. Yang, J. F. Berry, D. G. Musaev and H. M. L. Davies, *ACS Catal.*, 2018, **8**, 10676-10682.

127. J. C. Sharland, D. Dunstan, D. Majumdar, J. Gao, K. Tan, H. A. Malik and H. M. L. Davies, *ACS Catal.*, 2022, **12**, 12530-12542.

128. B. Wei, J. C. Sharland, D. G. Blackmond, D. G. Musaev and H. M. L. Davies, *ACS Catal.*, 2022, **12**, 13400-13410.

129. L. Fu, D. M. Guptill and H. M. L. Davies, *J. Am. Chem. Soc.*, 2016, **138**, 5761-5764.

130. C.-J. Yoo, D. Rackl, W. Liu, C. B. Hoyt, B. Pimentel, R. P. Lively, H. M. L. Davies and C. W. Jones, *Angew. Chem., Int. Ed.*, 2018, **57**, 10923-10927.

131. F. Neese, *WIREs Computational Molecular Science*, 2012, **2**, 73-78.

132. A. D. Becke, *Phys. Rev. A*, 1988, **38**, 3098-3100.

133. J. P. Perdew, *Phys. Rev. B*, 1986, **33**, 8822-8824.

134. F. Weigend, *Phys. Chem. Chem. Phys.*, 2006, **8**, 1057-1065.

135. F. Weigend and R. Ahlrichs, *Phys. Chem. Chem. Phys.*, 2005, **7**, 3297-3305.

136. S. Grimme, J. Antony, S. Ehrlich and H. Krieg, *J. Chem. Phys.*, 2010, **132**.

137. S. Grimme, S. Ehrlich and L. Goerigk, *J. Comput. Chem.*, 2011, **32**, 1456-1465.

138. F. Neese, *J. Phys. Chem. Solids*, 2004, **65**, 781-785.

139. T. Soda, Y. Kitagawa, T. Onishi, Y. Takano, Y. Shigeta, H. Nagao, Y. Yoshioka and K. Yamaguchi, *Chem. Phys. Lett.*, 2000, **319**, 223-230.

140. K. Yamaguchi, Y. Takahara and T. Fueno, Dordrecht, 1986.

141. Chemcraft - graphical software for visualization of quantum chemistry computations. Version 1.8, build 682., (accessed 5/21, 2025).

142. N. F. Chilton, R. P. Anderson, L. D. Turner, A. Soncini and K. S. Murray, *J. Comput. Chem.*, 2013, **34**, 1164-1175.

143. G. A. Bain and J. F. Berry, *J. Chem. Educ.*, 2008, **85**, 532.

Chapter 3: Investigating Metal-Metal Bonding in Hexa-Iron Cluster Complex

Reprinted with permission of Alessio Nicolini, Trey C. Pankratz, Marco Borsari, Rodolphe Clérac, Antonio Ranieri, Mathieu Rouzières, John F. Berry, and Andrea Cornia, *Inorganic Chemistry* **2023** *62* (26), 10171-10184

TCP contributed the Mössbauer spectroscopy, subsequent analysis and the DFT studies on the complex.

Abstract: Oligo-α-pyridylamides offer an appealing route to polyiron complexes with short Fe–Fe separations and large room-temperature magnetic moments. A derivative of tris(2-aminoethyl)amine (H_6tren) containing three oligo-α-pyridylamine branches and 13 nitrogen donors (H_6L) reacts with $[Fe_2(Mes)_4]$ to yield an organic nanocage built up by two tripodal ligands with interdigitated branches (HMes = mesitylene). The nanocage has crystallographic D_3 symmetry but hosts a remarkably unsymmetric hexairon–oxo core, with a central $Fe_5(\mu_5\text{-}O)$ square pyramid, two oxygen donors bridging basal sites, and an additional Fe center residing in one of the two tren-like pockets. Bond valence sum (BVS) analysis, density functional theory (DFT) calculations, and electrochemical data were then used to establish the protonation state of oxygen atoms and the formal oxidation states of the metals. For this purpose, a specialized set of BVS parameters was devised for Fe^{2+}–N^{3-} bonds with nitrogen donors of oligo-α-pyridylamides. This allowed us to formulate the compound as $[Fe_6O_2(OH)(H_3L)L]$, with nominally four Fe^{II} ions and two Fe^{III} ions. Mössbauer

spectra indicate that the compound contains two unique Fe^{II} sites, identified as a pair of closely spaced hydroxo-bridged metal ions in the central $Fe_5(\mu_5\text{-}O)$ pyramid, and a substantially valence-delocalized $Fe^{II}_2Fe^{III}_2$ unit. Broken-symmetry DFT calculations predict strong ferromagnetic coupling between the two iron(II) ions, leading to a local $S = 4$ state that persists to room temperature and explaining the large magnetic moment measured at 300 K. The compound behaves as a single-molecule magnet, with magnetization dynamics detectable in zero static field and dominated by an Orbach-like mechanism with activation parameters $U_{eff}/k_B = 49(2)$ K and $\tau_0 = 4(2) \times 10^{-10}$ s.

Section 1: Introduction: A frontier in the chemistry of metal-metal bonds is the deliberate construction of compounds containing extended metal atom chains (EMACs).[1–9] Oligo-α-pyridylamido ligands have been foundational to this area of research. The simplest example is the anion of di(pyridin-2-yl)amine (Hdpa, Scheme 3.1.1),[10] which is known to support over 300 EMAC entries in the Cambridge Structural Database (CSD).[11] Also shown in Scheme 3.1.1 is H_2tpda, an extended proligand whose dianionic form can afford pentametallic EMACs.[12]

Although extremely rare, iron-based EMACs are of special significance, because short Fe–Fe separations can stabilize high-spin states that persist to room temperature.[13–15] In 2018, we discovered that $tpda^{2-}$ can support linear, tetrairon(II) chains of the type $[Fe_4(tpda)_3X_2]$ with X = Cl (**1**) or Br (**2**).[16,17] In these EMACs, the three $tpda^{2-}$ ligands wrap around the metal atom chain to give a helical structure with threefold symmetry.[#] This type

of symmetry is comparatively rare in EMAC structures and was previously encountered only in copper(I) chemistry.[18,19] It is also rare among metal–metal bonded dimers supported by N-donor ligands, with $[Fe_2(form)_3]$ and $[Co_2(form)_3]$ representing early examples (Hform = *N*,*N*′-diphenylformamidine),[20–22] which have been followed by a spectacular Cr_2 compound having a Cr–Cr quintuple bond.[23–26] However, the incorporation of only four out of five possible metals in **1** and **2** results in large Fe–Fe separations (2.94–2.99 Å) and weak magnetic interactions. More recently, Guillet and co-workers used a sterically-hindered derivative of 2,6-diaminopyridine to enforce much shorter Fe–Fe distances (2.44 Å) in a trigonally symmetrical triiron(II) EMAC, which in fact exhibits a well-isolated $S = 6$ state.[13]

In 2014, Bill, Gagliardi, Lu, and coworkers utilized H_3py_3tren, a triply arylated derivative of tris(2-aminoethyl)amine (H_6tren), to promote short M–M distances (2.29–2.53 Å) in complexes $[M^1M^2Cl(py_3tren)]$ with $M^i = Fe^{2+}$, Co^{2+} or Mn^{2+} (Scheme 1).[27] Building off of this precedent, we imagined that an extended version of the H_3py_3tren proligand could be used to support trigonally symmetrical EMACs. Therefore, we designed, synthesized, and isolated in good yield (~60%) the new polynucleating tripod H_6L (Scheme 1), which contains thirteen nitrogen donors of four different types, and one more α-pyridylamino unit per branch than H_3py_3tren.[28]

In this work, we report our first attempt to use H_6L to form iron(II)-based EMACs. To our surprise, we failed to isolate the expected neutral complex $[Fe_3L]$ or longer species. Instead, we reproducibly obtained a remarkably low-symmetry hexairon-oxo core hosted in a threefold-symmetrical organic nanocage provided by two tripodal ligands with

interpenetrating branches. Combining compositional analysis, Electrospray Ionization Mass Spectrometry (ESI-MS), X-ray crystallography, electrochemistry, and Mössbauer spectroscopy with Density Functional Theory (DFT) and Bond Valence Sum (BVS) calculations, we reached at the formula $[Fe_6O_2(OH)(H_3L)L]$ (**3**) for this compound. Based on our current understanding, in **3** a central pyramidal $Fe_5(\mu_5\text{-}O)$ core is embraced by two organic ligands (H_3L^{3-} and L^{6-}) and coordinated by two additional oxo groups, one of which is protonated. The fully deprotonated L^{6-} ligand hosts a sixth Fe center in its tren-like pocket, while the same coordination site in H_3L^{3-} remains unmetalated. The compound nominally contains *four* Fe^{2+} and *two* Fe^{3+} ions with extensive valence delocalization. It has a large room-temperature magnetic moment (14.8 μ_B) and exhibits slow relaxation of its magnetization at low temperature, detectable even in zero static field.

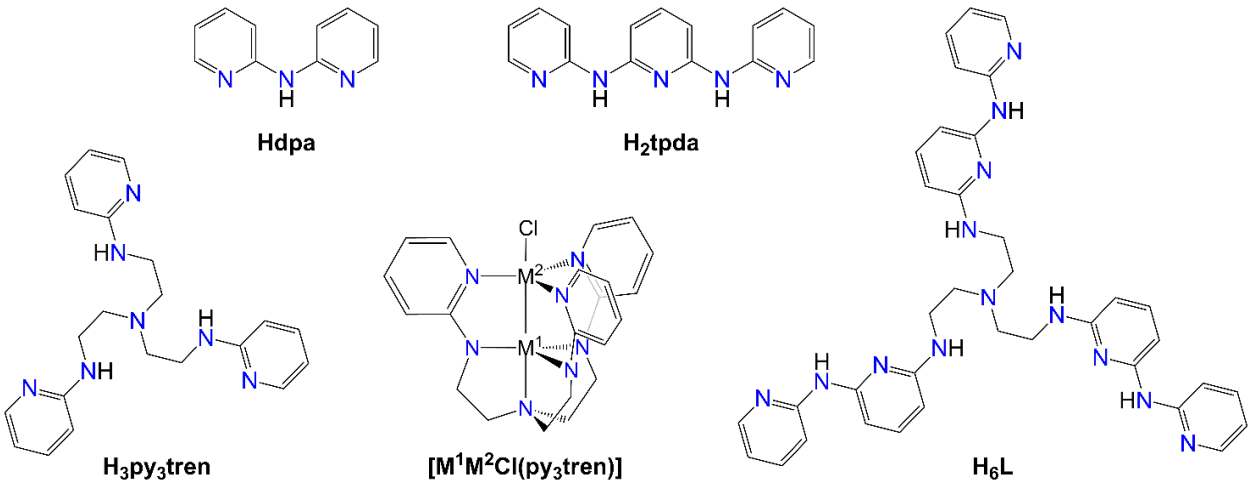

Scheme 3.1.1. Structures of Hdpa, H_2tpda, H_3py_3tren, H_6L, and complexes $[M^1M^2Cl(py_3tren)]$ (M^i = Fe^{2+}, Co^{2+}, Mn^{2+}).[27]

Section 2: Synthesis and solution studies. H_6L (Scheme 3.1.1) was designed with the idea of preparing stable arrays of three or more metal ions, wrapped by its fully deprotonated Hdpa-like branches and perhaps arranged linearly to form new EMACs. In an attempt to access neutral triiron(II) species $[Fe_3L]$, we followed a synthetic procedure that is similar to that leading to halide-terminated iron(II) EMACs **1** and **2** (Eq. 3.2.1),[16,17] but omitting the metal halide FeX_2 precursor (Eq. 3.2.2).

$$2FeX_2 + 3[Fe_2(Mes)_4] + 6H_2tpda \rightarrow 2[Fe_4(tpda)_3X_2]\ (\mathbf{1}, \mathbf{2}) + 12HMes \qquad (3.2.1)$$

$$3[Fe_2(Mes)_4] + 2H_6L \rightarrow 2[Fe_3L] + 12HMes \qquad (3.2.2)$$

Therefore, H_6L was admixed with a slight excess of $[Fe_2(Mes)_4]$ (1:1.6 molar ratio) in toluene, and the mixture was heated to reflux for 3 hours in a glovebox (HMes = mesitylene). This reaction, in which the organoiron compound serves both as a metal source and as a strong base, yielded an orange solid that was separated by filtration and extensively extracted with thf. Evaporation of the solvent led to a red, powdery solid that was characterized by elemental analysis (EA), ESI-MS, and UV-Vis-NIR spectroscopy (see below). Obtaining X-ray quality crystals of this material proved extremely challenging. Many recrystallization attempts were conducted based on slow liquid or gas diffusion of Et_2O, *n*-hexane or toluene into thf, 1,4-dioxane or CH_3CN solutions, which mostly gave only spherulites of a very dark microcrystalline material. However, slow liquid diffusion of Et_2O into a thf solution afforded dark red plates, which are exceedingly air-sensitive but sufficiently stable to be handled in immersion oil. The compound was structurally validated by X-ray crystallography (see below) and the main species was identified as the hexairon complex

$[Fe_6O_2(OH)(H_3L)L]$ (**3**), containing unexpected oxygen atoms from adventitious sources. In a similar attempt to prepare triiron(II) EMACs supported by dpa^- ligands, Cotton *et al.* reacted $FeCl_2$ with Lidpa but failed to obtain the sought-for linear compound. Instead, they isolated complex $[Fe_4(\mu_4\text{-}O)(dpa)_6]$ (**4**) with a tetrahedral $[Fe_4(\mu_4\text{-}O)]^{6+}$ unit (the corresponding tetramanganese(II) complex was also obtained starting from $MnCl_2$). The authors attributed the central oxygen atom to a partial hydrolysis of the LiMe reactant used to prepare Lidpa.[29] McKenzie and co-workers reported the occasional low-yield isolation of **4** co-crystallized with the diiron(II) species $[Fe_2(dpa)_3Cl]$ upon reacting $[Fe_2(Mes)_4]\cdot Et_2O$ with Hdpa in toluene, both the O^{2-} and the Cl^- ligands being in this case adventitious.[30] In contrast with this, compound **3** was reproducibly obtained in two different labs (Modena and Madison) and with significant yields.

The ESI-MS and UV-Vis-NIR spectra in thf suggest that the powder and the crystals are the same compound (Figure S1 and S2 in the published SI), though samples in solution are NMR silent (Figure S3). The ESI-MS peaks with $m/z > 1500$ in the positive-ion spectra (Figure S1) can be attributed to species containing two tripodal ligands, three oxygen atoms, a penta- to heptairon core, and a variable degree of protonation ($[Fe_nO_3H_mL_2]^+$ with n = 5, 6, 7 and m = 1–5). Both spectra are dominated by a strong peak around m/z = 1680, whose isotopic pattern can be well simulated as a linear combination of contributions from $[Fe_6O_3H_2L_2]^+$, $[Fe_6O_3H_3L_2]^+$, $[Fe_6O_3H_4L_2]^+$, and $[Fe_6O_3H_5L_2]^+$ (though with different combination coefficients for the powder and the crystals). Minority signals at m/z = 1626 and 1735 are well simulated by penta- and heptanuclear species, respectively ($[Fe_5O_3H_4L_2]^+$ + $[Fe_5O_3H_5L_2]^+$; $[Fe_7O_3HL_2]^+$). Below m/z = 1500 the strongest peaks are from $[Fe_3ClL]^+$ (850

and $[Fe_3L]^+$ (815), with the former presumably reflecting chloride traces from the synthesis of $[Fe_2(Mes)_4]$ or adventitious chloride ions in the mass spectrometer.

The UV-Vis-NIR spectrum of crystalline **3** dissolved in thf (Figure S2 in the published SI) presents two intense absorptions with maxima at λ_{max} = 242 and 341 nm, along with three shoulders around 268, ~380, and ~500 nm. The powder sample exhibits remarkably similar spectral features. As long as contact with air is rigorously excluded, these spectra do not change over long time periods, suggesting high stability of the complex in thf solution.

Section 3: X-ray Crystallography. Although crystals of **3** are very weak diffractors, a single-crystal X-ray investigation was successfully completed at 115(2) K (Table S1 in the published SI). The final structural model is depicted in Figures 3.3.1 and S5 in the published SI while selected interatomic distances and angles are presented in Table 3.3.1. The complex is located on a crystallographic site with D_3 symmetry in space group $P\bar{3}1c$ (Z = 2) and contains two tripodal ligands with imposed threefold symmetry and interpenetrating branches (Figure 3.3.1). All branches are helically wrapped around the threefold axis, with ~25° angles between the mean planes of adjacent pyridine rings. Since the two ligands are symmetry-related by the three dyads orthogonal to the threefold axis, they have the same handedness. However, the space group is centrosymmetric and the crystal thus contains both enantiomers in 1:1 proportion. The distance of the tertiary N atoms (N1 and $N1^{III}$) from the center of the structure is 6.738(9) Å and the molecular size exceeds 1.6 nm.

The most difficult part of the crystallographic analysis was modelling the inner core of **3** (details are provided in the Experimental Section). The two tripodal ligands in fact

encapsulate a hexairon-oxo core that is massively disordered around the D_3 symmetry site, meaning that the actual molecular symmetry is lower than D_3. The final model encompasses a central $Fe_5(\mu_5\text{-}O)$ cluster with a distorted square-pyramidal geometry (τ = 0.36 for the central O atom), orientationally disordered around the threefold axis (Figure 3.3.2). The Fe1 and Fe2 sites thus show partial occupancies of 2/3 and 1/3, respectively, while O1 has full occupancy and lies on the D_3 symmetry site. On either side of the central core, two additional full-occupancy O atoms (O2 and $O2^{III}$) are located on the threefold axis at 2.796(7) Å from O1 (Figure 3.3.1.).

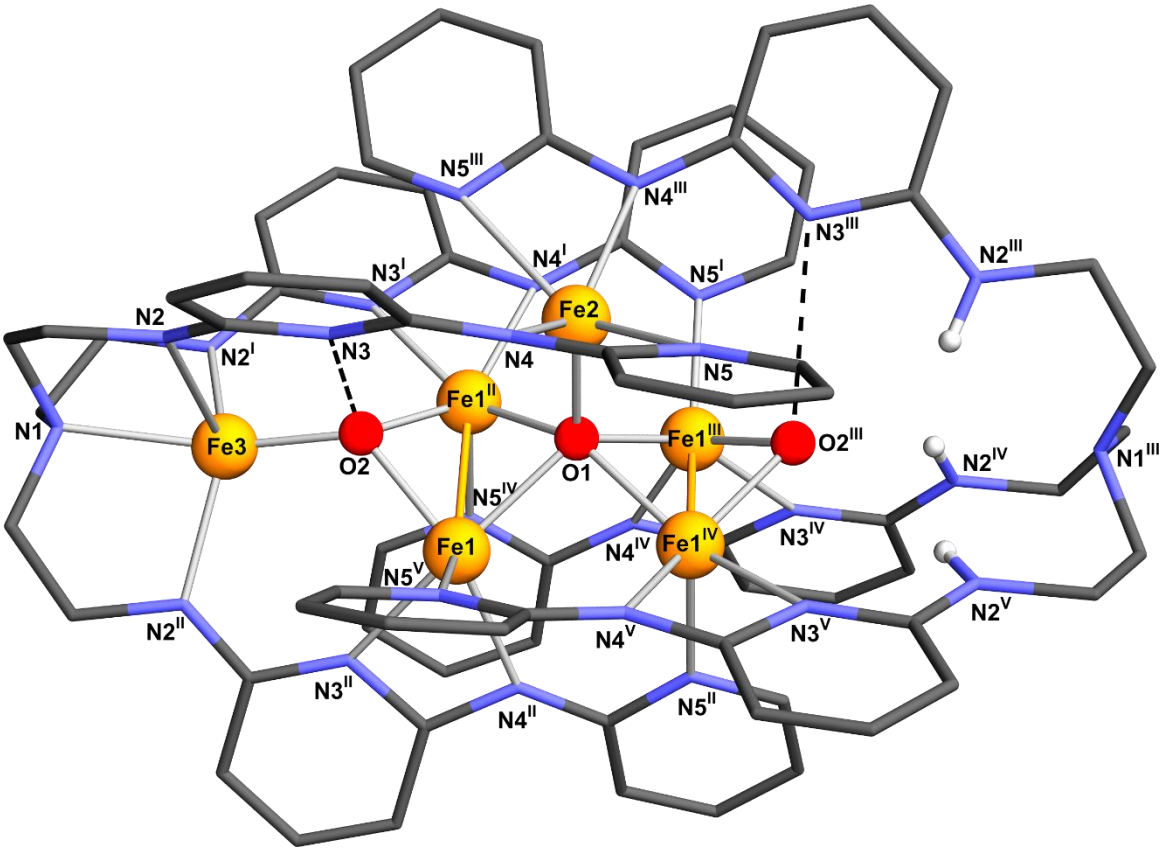

Figure 3.3.1. Molecular structure of **3**. The organic ligands are represented with the wireframe model, while Fe and O atoms are drawn using a ball-and-stick model (an ellipsoid representation can be found in Figure S5 in the published SI). The dotted lines connecting O2 and O2^{III} with a N_{py} donor represent possible OH···N_{py} hydrogen bonds. Color code: orange, Fe; red, O; blue, N; dark gray, C; light gray, H. Only the hydrogen atoms bonded to N2^{III}, N2^{IV}, and N2^{V} are displayed in the figure. Symmetry codes: I = 1–*x*+*y*, 1–*x*, *z*; II = 1–*y*, *x*–*y*, *z*; III = 1–*x*+*y*, *y*, 0.5–*z*; IV = *x*, *x*–*y*, 0.5–*z*; V = 1–*y*, 1–*x*, 0.5–*z*.

The base of the pyramid is nonplanar, with internal angles Fe1–Fe1^{II}–Fe1^{III} = 84.85(4)° and Fe1^{II}–Fe1–Fe1^{IV} = 93.065(13)°. The length of the minor edge is 2.629(2) Å, suggesting a

possible M–M bond within the Fe1,Fe1^{II} and Fe1^{III},Fe1^{IV} pairs. This distance is in fact comparable with the mean Fe–Fe separation (2.64 Å) in a variety of carbonyl-containing polyiron complexes,[31] and shorter than the partial Fe–Fe bonds (2.70 Å) in iron-sulfur clusters such as Roussin's black salt.[32] On the other hand, the Fe1···Fe1^{IV} and Fe1^{II}···Fe1^{III} distances are much longer (3.028(3) Å) and indicate no M–M bond. Each Fe1 atom is five-coordinate with two pyridine-type nitrogen atoms (N_{py}) and one amido-type nitrogen atom (N_{am}), *plus* O1 and O2 as ligands (Fe1–N = 2.129–2.151 Å, Fe1–O = 1.997–2.133 Å). The apical site of the $Fe_5(\mu_5\text{-}O)$ pyramid is occupied by Fe2, whose distances to the basal metal sites are in the range 3.232–3.451 Å. Fe2 is also five-coordinate with two pairs of symmetry-equivalent N_{am} and N_{py} atoms, and O1 as donors (Fe2–N_{am} = 2.019(5) Å, Fe2–N_{py} = 2.331(5) Å, Fe2–O1 = 1.931(3) Å). The rough square pyramidal geometry has Fe2 lying ~0.86 Å from the mean plane defined by its four basal N donors.

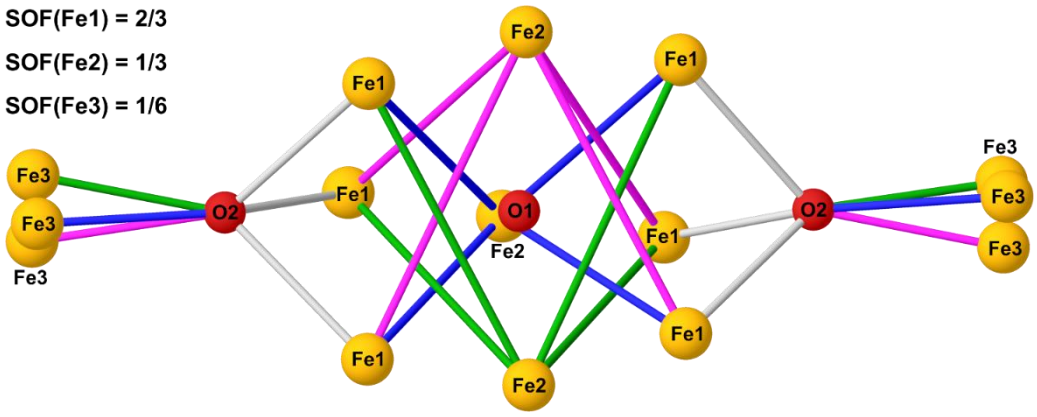

Figure 3.3.2. Orientational disorder of the metal core of **3** around the crystallographic threefold axis (ball-and-stick model, SOF = site occupancy factor). O1 and O2 have full occupancy (SOF = 1) and lie on the D_3 symmetry site and on the threefold axis, respectively. Atom color code is the same as in Figure 1. The three disordered components are drawn with different colors (violet, green, and blue).

Table 3.3.1. Selected interatomic distances (Å) and angles (°) in **3**.[a]

Distances (Å)		Angles (°)	
Fe1–Fe1^{II}	2.629(2)	Fe1–Fe1^{II}–Fe1^{III}	84.85(4)
Fe1···Fe1^{IV}	3.028(3)	Fe1^{II}–Fe1–Fe1^{IV}	93.065(13)
Fe1···Fe2	3.451(3)	Fe1–O1–Fe1^{II}	76.10(5)
Fe1^{II}···Fe2	3.232(3)	Fe1–O1–Fe1^{IV}	90.47(7)
Fe1–O1	2.1327(13)	Fe1–O1–Fe2	116.18(4)
Fe1–O2	1.997(4)	Fe1^{II}–O1–Fe2	105.25(4)
Fe1–N3^{II}	2.151(5)	Fe1–O2–Fe1^{II}	82.3(2)
Fe1–N4^{II}	2.129(5)	Fe1–O2–N1	130.53(15)
Fe1–N5^{V}	2.149(5)	N3^{II}–Fe1–N4^{II}	63.2(2)
Fe2–O1	1.931(3)	N3^{II}–Fe1–N5^{V}	97.1(2)
Fe2–N4	2.019(5)	N4^{II}–Fe1–N5^{V}	101.5(2)
Fe2–N5	2.331(5)	N4–Fe2–N5	62.3(2)
Fe3–O2	1.851(8)	N4–Fe2–N5^{III}	98.9(2)
Fe3–N1	2.162(10)	N1–Fe3–O2	158.4(3)
Fe3–N2	2.679(8)	N1–Fe3–N2	70.45(18)
Fe3–N2^{I}	2.180(12)	N1–Fe3–N2^{I}	81.1(3)
Fe3–N2^{II}	2.129(11)	N1–Fe3–N2^{II}	82.3(3)
O1···O2	2.796(7)		
O1···N1	6.738(9)		
O2···N3	2.979(5)		

[a]Symmetry codes: I = 1–*x*+*y*, 1–*x*, *z*; II = 1–*y*, *x*–*y*, *z*; III = 1–*x*+*y*, *y*, 0.5–*z*; IV = *x*, *x*–*y*, 0.5–*z*; V = 1–*y*, 1–*x*, 0.5–*z*.

The central O^{2-} ion (O1) is found at 0.75 Å from the mean plane defined by the four Fe1 ions. As mentioned above it forms short contacts with the four Fe1 atoms (2.1327(13) Å), and an even shorter one with Fe2 (1.931(3) Å). Similar square-pyramidal $Fe_5(\mu_5\text{-}O)$ units were previously observed in compounds $[Fe_5(\mu_5\text{-}O)(\mu\text{-}OEt)_8(OEt)_5]$[33] (**5**) and $[Fe_5(\mu_5\text{-}O)(\mu\text{-}O^iPr)_8Cl_5]$[34] (**6**). The cores of **5** and **6** are almost identical to each other, with square-like basal planes (internal Fe···Fe···Fe angles = 89.7–90.3°) and Fe···Fe separations > 3 Å, indicating no Fe–Fe bonds. Therefore, to the best of our knowledge, **3** is the first example of a complex with a distorted-square-pyramidal $Fe_5(\mu_5\text{-}O)$ core and potential M–M bonds.

Fe3 is located in the coordination pocket of the tren-like moiety, ~0.37 Å off the threefold axis, and is consequently disordered over three positions. Additionally, it is only half occupied, affording an average number of *six* Fe centers per molecule. This is in accordance with EA and with the clear observation of a residual electron density peak attributable to H(N2) hydrogen atom in ΔF maps (see Experimental Section). Most likely, then, a *single* tren-like pocket per molecule (N1,N2,$N2^{I}$,$N2^{II}$ in Figure 1) undergoes deprotonation and hosts a metal ion, while the remaining one ($N1^{III}$,$N2^{III}$,$N2^{IV}$,$N2^{V}$ in Figure 3.3.1) retains its secondary NH groups and is unmetalated. Alternative scenarios cannot be excluded, like the occurrence of penta- and heptairon species mixed together in 1:1 proportion in the crystal lattice. Clearly, X-ray diffraction and EA cannot distinguish between these limiting situations and all the intermediate possibilities. Ionic species containing from five to seven metal centers were indeed detected by ESI-MS (see above), but signals from hexairon species were by far the most intense, suggesting that Fe_6

complexes are dominant, under the assumption that Fe_5, Fe_6, and Fe_7 species are equally as easily ionized and fly equally well in the ESI-MS spectrometer.

The tren-like portion of the structure is different from that found in complexes of triply-deprotonated H_3py_3tren, the shorter congener of H_6L.[27] In these complexes, the three secondary N atoms (N_{am}) and the tertiary N donor of py_3tren^{3-} simultaneously coordinate to a metal ion lying on the idealized threefold axis of the ligand. In **3**, the bulky iron-oxo core increases the divergence between the ligand's three branches, affording larger distances between N_{am} atoms (3.93 vs. 3.2–3.4 Å) and precluding their simultaneous coordination to Fe3. As a result, Fe3 has four short coordination bonds with O2, N1, and two N_{am} donors (1.851(8), 2.162(10), 2.180(12) and 2.129(11) Å, respectively), and a much longer contact with a third N_{am} atom (2.679(8) Å). Considering that the ligand's geometry is averaged over metalated and empty tren-like pockets, these bond distances may not accurately reflect the actual coordination geometry, as confirmed by the distinctly prolate displacement ellipsoid of N2 (Figure S5 in the published SI).

An intriguing structural feature is that, in spite of the severely disordered core, O2 is found exactly on the threefold axis within experimental resolution and has no abnormal displacement ellipsoid. Its protonation state could not be directly determined by inspection of ΔF maps, but was inferred using BVS calculations and DFT studies (see below). Worth noting is also the acute Fe1–O2–$Fe1^{II}$ angle of 82.3(2)°, which can be explained by the short Fe–Fe separation. A similar coordination geometry was recently observed in hydroxo-bridged triosmium complex $[Os_3(CO)_8(\mu\text{-OH})(\mu\text{-H})(\mu\text{-dppm})]$ (**7**, where

dppm is bis(diphenylphosphino)methane).[35] In complex **7**, an OH^- ion coordinates two Os atoms engaged in a M–M bond (Os–Os = 2.7896(17) Å) and the Os–O–Os angle is as small as 81.1(2)°.

Section 4: Bond Valence Sum Calculations. The massive disorder effects described in the previous Section may easily lead to inaccurate bond lengths. Nevertheless, we attempted to validate the proposed structural model using BVS calculations (Table S2 in the published SI).[36] The observed bond lengths support the assignment of the central oxygen (O1) as a μ_5-O^{2-} ligand (BVS = 1.95/2.08 for Fe^{2+}/Fe^{3+} parameters). The two identical Fe1–O2 distances instead afford BVSs of 0.98/1.05 for O2 and are thus suggestive of a μ-OH^- group when the neighboring tren-like pocket is unmetalated. What makes this hypothesis more realistic is the fact that O2 is surrounded by three N_{py} atoms almost exactly coplanar with it. The arrangement of these N_{py} atoms and the N_{py}–O2 distance of 2.979(5) Å would favour an OH···N_{py} hydrogen bond of moderate strength (according to the classification of Jeffrey), as shown by the dashed lines in Figure 1.[37,38] Addition of the Fe3–O2 contribution leads to BVS = 1.71/1.83, for O2, which is suggestive of a μ_3-O^{2-} group when the neighboring tren-like pocket is metalated. These protonation states were confirmed by DFT calculations (see below). Since no counterions were detected in the X-ray diffraction analysis, and conductivity measurements indicate nonelectrolyte behaviour (see next Section), we formulate the compound as $[Fe_6O_2(OH)(H_3L)L]$ (**3**), which requires mixed valency with nominally *four* Fe^{2+} and *two* Fe^{3+} ions (average oxidation state = +2.33).

Calculations on Fe1, Fe2, and Fe3 with standard BVS parameters yield BVS = 1.90/2.14, 2.01/2.30, and 1.84/2.09, respectively (Table S2). As a possible refinement, high-quality CSD data for high-spin (HS) Fe^{2+} complexes with dpa^{-} or $tpda^{2-}$ ligands were also used to determine a specialized R_0 parameter for Fe^{2+}–N^{3-} bonds with N_{py} and N_{am} donors (Table S2 and Figure S6). The calculated BVS values are ca. 0.1 valence units higher than the previous set based on standard Fe^{2+} parameters (Table S2). We conclude that the oxidation state of the metal ions in **3** is close to +2 and that any mixed valence must be heavily delocalized.

Section 5: Electrochemistry. The cyclic voltammetry (CV) curve for **3** in thf is shown in Figure 3.5.1. It presents five consecutive major reduction peaks with the corresponding oxidation counterparts (hereafter indicated as signals I, II, III, IV, V+VI at decreasing potential values). The strictly similar total currents of these groups suggest that signals I, II, III, IV and V+VI are due to the same species containing several redox centers (Fe^{3+}/Fe^{2+}) and undergoing successive reduction/oxidation processes. The signals marked with an asterisk in Figure 3 have much lower peak currents and may arise from trace amounts of additional species. The overall CV response thus supports our proposal that hexairon complexes are largely dominant in **3**, with penta- and heptairon complexes as possible minority components (see ESI-MS results). The major signals seem to be paired into three groups of redox couples, partially or completely overlapped. The first group consists of two distinct redox couples (signals I and II) that partially overlap. Also, the second group comprises two redox couples that, however, are better resolved. Signal III features an intense anodic current, which is about the sum of the cathodic currents of signals III and IV. The anodic peak of signal IV is rather low, but it grows at the detriment of anodic signal III with

increasing scan rate (*v*). This suggests that the corresponding iron center changes its coordination environment upon reduction and that the reduced species re-oxidizes at a potential very similar to that of signal III. The more negative signal (signal V+VI) is very intense and characterized by a cathodic peak current remarkably higher than those of the other cathodic signals, while the anodic current is similar to that of signal III and to the sum of the anodic currents of signals I and II. The peak-to-peak separation varies for the different signal couples, but in all cases, it increases with *v*. The cathodic peak currents are proportional to the square root of *v*. This means that the electrochemistry of **3** consists of five quasi-reversible, diffusion-controlled redox processes. The formal potential values $E^{\circ\prime}$ and the standard heterogeneous electron transfer (ET) rate constants k_{ET} associated with the redox processes are reported in Table 3.5.1.

Complex **3** shows an unusual redox behaviour since its ET processes span a very large potential window, about 2.2 V. The occurrence in the CV of reversible processes that appear to be coupled in pairs suggests the presence of electronic interactions between the iron ions and minor structural reorganization upon changing the redox state, except for signal IV whose reduced form is unstable.[39] The separations between $E^{\circ\prime}$ values of consecutive ET processes ($\Delta E^{\circ\prime}$) are mostly large, and only signal I and II are partially overlapped (Table 3.5.1). This possibly reflects the stabilization energy imparted to the complex by electron delocalization.[40,41] The $\Delta E^{\circ\prime}$ values mostly correspond to very large comproportionation constants ($K_c = \exp[nF(E^{\circ}_1 - E^{\circ}_2)/(RT)]$)[42,43] ranging between 10^8 and 10^{16},

and only the K_c value related to signals I and II is quite small ($K_c = 9.01 \cdot 10^2$). Large values of K_c indicate high thermodynamic stability of the redox-active forms of the complex toward disproportionation (Table 3.5.1).[44] The negative $E°'$ values, although distributed over a wide range, are comparable to those found for other related iron-complexes.[45,46] The k_{ET} values for the observed ET processes are low and rather similar (Table 3.5.1). This could be related to a high reorganization energy λ, already observed for other mixed valence complexes.[47]

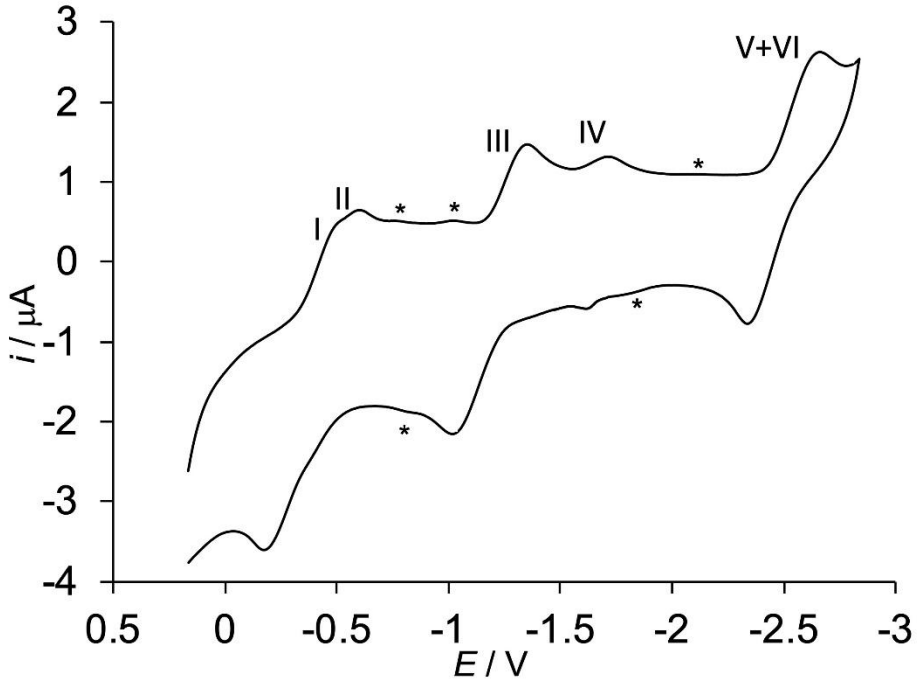

Figure 3.5.1. CV of **3** (0.025 mM in thf) at −10 °C. Glassy carbon (GC) working electrode, base electrolyte 0.05 M tetra-*n*-butylammonium tetrafluoborate (TBATFB), scan rate 0.05 V s^{-1}, ferrocenium/ferrocene reference.

Table 3.5.1**.** Electrochemical data from CV for the consecutive ET processes of **3** (0.25 mM in thf) at −10 °C, using a GC working electrode and TBATFB 0.05 M as base electrolyte.[a]

	$E°'$ / V	$\Delta E°'$ / V	K_c	k_{ET} / cm s^{-1}
E(I)	–0.314			0.0028
		0.157	$9.01 \cdot 10^{2}$	
E(II)	–0.471			0.0033
		0.706	$1.93 \cdot 10^{13}$	
E(III)	–1.177			0.0027
		0.457	$3.98 \cdot 10^{8}$	
E(IV)	–1.634			0.0046
		0.871	$2.45 \cdot 10^{16}$	
E(V+VI)	–2.505			0.0026

[a] $E°'$ = formal reduction potential (referenced to the ferrocenium/ferrocene redox couple), $\Delta E°'$ = separation between $E°'$ values of consecutive ET processes, K_c = comproportionation constant, k_{ET} = heterogeneous ET rate constant. The average errors on $E°'$, $\Delta E°'$, K_c, and k_{ET} are ±0.002 V, ±0.004 V, ±16%, and ±8%, respectively.

The molar conductivity measured between –23 and 2 °C on a 0.25 mM solution in thf is of the order of 0.1 $ohm^{-1}\ cm^2\ mol^{-1}$ and depends only slightly on temperature (Table S3 in the published SI). Being much lower than found for ionic complexes in the same solvent[48] or in other organic solvents,[49] it suggests that **3** is a nonelectrolyte in thf.

Section 6: Mössbauer Spectroscopy. To assist in assigning oxidation states and spin states to the Fe ions in **3**, Mössbauer spectra were recorded on a polycrystalline sample at 77 (Figure 4) and 10 K (Figure S7 in the published SI). The 10 K spectrum appears to be broadened by magnetic relaxation effects and will not be discussed further. Thus, we focus our discussion on the spectrum recorded at 77 K, which contains three major features at 0.07, 1.27, and 2.27 mm s^{-1}. These features are much broader than the typical Mössbauer linewidth for a single Fe site ($\Gamma_{FWHM} \sim 0.3$ mm s^{-1}), indicating that multiple Fe sites contribute to each of them. This is not surprising, since crystallographic symmetry already requires three different Fe centers in a 4:1:1 ratio, namely the set of basal sites (Fe1, $Fe1^{II}$, $Fe1^{III}$, $Fe1^{IV}$), the apical site Fe2 and the peripheral site Fe3 located in the tren-like pocket (Figure 3.1.1). Several models for the 77 K spectrum were investigated using three unique quadrupole doublets with adjustable relative areas. Here, we focus on fits in which the spectral peak at 2.27 mm s^{-1} was modelled with two overlapping subspectra (**Fit1** and **Fit2** in Figure 3.6.1), though models with a single quadrupole doublet (**FitS1** and **FitS2** in Figure S8 in the published SI) were considered. In either case, there are two nearly identical overall fits depending on whether the two quadrupole doublets that more extensively overlap are offset (**Fit1** and **FitS1**) or nested (**Fit2** and **FitS2**). Unfortunately, it is not possible to determine whether the offset or the nested models are more correct.

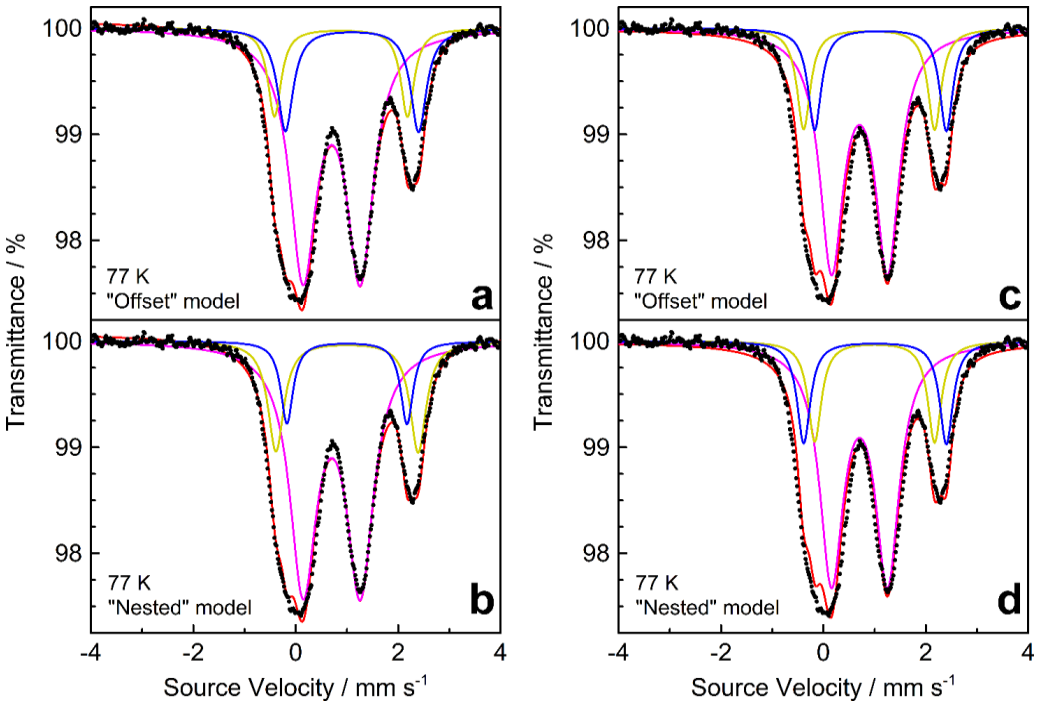

Figure 3.6.1. Mössbauer spectrum of **3** at 77 K (solid dots) with accompanying **Fit1** (a), **Fit2** (b), **Fit3** (c), and **Fit4** (d) as red lines. The red traces are additionally divided into three quadrupole doublets (purple, yellow, and blue lines). The areas of sites 1, 2, and 3 in (c) and (d) are constrained to 66.7%, 16.7%, and 16.7%, respectively.

In **Fit1** and **Fit2** (Figure 3.6.1.) the two dominant lines are reproduced by a single, broad quadrupole doublet that accounts for 69% of the total iron content. The best-fit parameters (isomer shift δ = 0.70 mm s^{-1} and quadrupole splitting ΔE_Q = 1.11–1.12 mm s^{-1}) are consistent with mixed HS iron(II)/iron(III) character.[50] However, the large linewidth of this signal (Γ_{FWHM} ~ 0.63 mm s^{-1}) suggests contributions from multiple Fe sites. Efforts to use more than one quadrupole doublet afforded multiple equally stable solutions and no new

information was gained from such overparameterized fits. Two unique quadrupole doublets with larger δ and ΔE_Q and a more normal linewidth (~ 0.3 mm s^{-1}) are needed to fit the remaining features of the spectrum, namely, the low velocity edge of the main signal and the smaller high velocity feature. An offset model (**Fit1**) yields different isomer shifts for these doublets (0.88 and 1.10 mm s^{-1}), but the same quadrupole splitting (2.60 mm s^{-1}). **Fit2** has nested doublets with the same isomer shift (1.00 mm s^{-1}), and different quadrupole splittings (2.78 and 2.34 mm s^{-1}). In both cases, the Mössbauer parameters are typical for HS iron(II) ions.[50] The integrated intensity of each of these doublets corresponds to 11–19% of the total area of the spectrum. Overall, the relative areas of the three subspectra in **Fit1** and **Fit2** deviate only slightly from the 4:1:1 pattern (66.7 : 16.7 : 16.7%) of Fe sites in the crystal structure. As a consequence, two additional models (**Fit3** and **Fit4** in Figure 3.6.1.) were considered with a fixed 4:1:1 population. The best-fit parameters so obtained are fairly similar to those in the unconstrained models. As in **Fit1** and **Fit2**, the two major features may be fitted to a broad quadrupole doublet with δ = 0.71 mm s^{-1} and ΔE_Q = 1.09 mm s^{-1}, accounting for 2/3 of the total iron content. The remainder of the spectrum is fitted to two quadrupole doublets with populations fixed at 1/6 that are either offset or nested. The offset model (**Fit3**) has different isomer shifts (0.89 and 1.11 mm s^{-1}) and similar quadrupole splittings (2.56–2.57 mm s^{-1}). The nested model (**Fit4**) has similar isomer shifts (1.00–1.01 mm s^{-1}) and distinct quadrupole splittings (2.79 and 2.34 mm s^{-1}).

Comparing the extracted Mössbauer parameters, which are gathered in Table S4 in the published SI, to those of known, structurally related compounds is difficult. Most of the Fe site geometries in **3** are highly unique and have little direct structural precedent. The Fe site

located within the tren-like pocket (Fe3) is reminiscent of similar sites in dinuclear compounds [Fe_2(py_3tren)Cl] (**8**) and [FeMn(py_3tren)Cl] (**9**).[27] However, the Mössbauer parameters in these complexes may be heavily affected by metal–metal bonding. For instance, the isomer shifts in **8** and **9** (0.46–0.48 mm s^{-1}) are unusually low and fall outside the expected range for HS iron(II), while the quadrupole splittings (1.31–1.69 mm s^{-1}) lie at the lower edge of the range typical for HS iron(II) ions.[50]

In summary, the Mössbauer spectrum of **3** is complex, as expected for the large number of independent Fe sites. We have attempted to find a physically meaningful fit with the least number of independent parameters. Stable fits with an approximate 4:1:1 ratio of Fe signals indicate the presence of two unique Fe sites with large quadrupole splitting values and predominant HS iron(II) character. The Mössbauer parameters for the remainder of the Fe sites are instead suggestive of a mixed HS iron(II)/iron(III) character. These results are thus consistent with the proposed occurrence of four HS iron(II) ions and two HS iron(III) ions in the structure. This assignment is reasonable considering that strong delocalization of a mixed valent system causes both isomer shifts and quadrupole splittings to be observed in the range between what is expected for HS iron(II) and iron(III).

Section 7: Magnetic Susceptibility Measurements. The variable-temperature molar magnetic susceptibility (χ_M) of **3** is shown in the main panel of Figure 3.7.1 as a $\chi_M T$ vs. T plot, while the isothermal molar magnetization (M_M) measured at low temperature is plotted in the inset as a function of H/T. A $\chi_M T$ value of 27.4 cm^3 K mol^{-1} is found at room temperature. With lowering temperature, the $\chi_M T$ product at 1000 Oe gradually increases

reaching a maximum of 29.7 cm^3 K mol^{-1} at 22 K before dropping precipitously to 11.6 cm^3 K mol^{-1} at 1.8 K. The magnetization data at 1.86 K increase to 18.3 $N_A\mu_B$ at the highest applied field without saturating, pointing to a ground electronic state with at least 18 unpaired electrons. The overall shape of the $\chi_M T$ vs. T curve at low temperature suggests that both ferromagnetic and antiferromagnetic interactions are operative in the compound. Using the proposed oxidation state assignment of four HS iron(II) ions (S = 2) plus two HS iron(III) ions (S = 5/2), the high-temperature value expected for $\chi_M T$ is 20.8 cm^3 K mol^{-1} with g = 2.00 for all metal ions, or 22.6 cm^3 K mol^{-1} with g = 2.15/2.00 for Fe^{2+}/Fe^{3+} ions (Figure 3.7.1., black dashed line). These values are significantly lower than observed at room temperature (27.4 cm^3 K mol^{-1}) and suggest the presence of a strong ferromagnetic interaction influencing the room temperature $\chi_M T$ value.

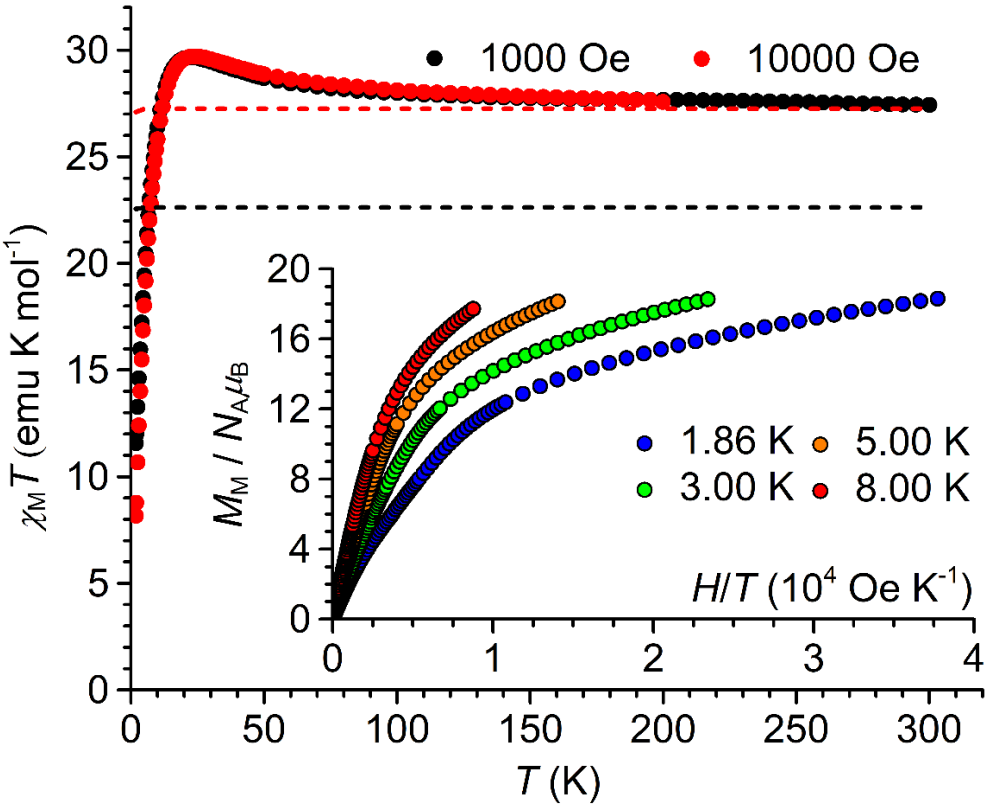

Figure 3.7.1. $\chi_M T$ vs. T data for **3** recorded at 1000 and 10000 Oe. The dashed lines are the expected magnetic responses for one S = 4, two S = 2, and two S = 5/2 uncorrelated spins (red), and for four S = 2 and two S = 5/2 uncorrelated spins (black), taking g = 2.15 for S = 4 and S = 2, and g = 2.00 for S = 5/2. Inset: Reduced magnetization curves at 1.86 (blue), 3.00 (green), 5.00 (orange), and 8.00 K (red).

Considering the relatively short Fe1···Fe1^{II} distance of 2.63 Å (equivalent to the Fe1^{III}···Fe1^{IV} distance), the room temperature $\chi_M T$ value could be explained by the presence of a ferromagnetically coupled iron(II)–iron(II) partially bonded dimer. A full bond between two HS iron(II) ions at a distance of 2.46 Å was indeed described to afford a thermally persistent S = 4 ground state.[51,52] If **3** is considered to contain such an S = 4 contribution, along with two isolated HS iron(II) and two isolated HS iron(III) centers, then the expected room

temperature $\chi_M T$ value is 24.8 cm^3 K mol^{-1} with g = 2.00 for all metal ions, or 27.3 cm^3 K mol^{-1} with g = 2.15/2.00 for Fe^{2+}/Fe^{3+} ions (Figure 3.7.1., red dashed line). These calculated data provide a much better match for the experimental value of 27.4 cm^3 K mol^{-1} (Figure 3.7.1). The existence of such a strongly ferromagnetically coupled iron(II) pair within the hexairon-oxo core of **3** was corroborated by DFT calculations described in the next Section. To probe any slow magnetic relaxation, the alternating current (ac) magnetic susceptibility of **3** was measured at low temperature. Both in-phase (χ') and out-of-phase (χ'') components depend on frequency (ν) in zero dc field indicating that the compound is a single-molecule magnet (Figure S9 in the published SI). The fitting of the χ' vs. ν and χ'' vs. ν plot leads to a relaxation time (τ) that follows an activated behaviour between 1.9 and 2.8 K with an energy barrier (U_{eff}/k_B) of 49(2) K and a pre-exponential factor (τ_0) of $4(2)\cdot10^{-10}$ s (Figures S9-S13 in the published SI). Considering the very small temperature domain that is available to study the relaxation, it is difficult to be absolutely sure that the relaxation follows an Orbach process. Nevertheless, the small field dependence of the relaxation time at 2 K up to 2 T supports this interpretation (Figures S11-S13 in the published SI).

Section 8: Density Functional Theory Calculations. To interrogate the protonation state of oxygen atoms inferred from crystallographic data and BVS values, DFT calculations were employed. The crystallographic coordinates of **3** were used as a starting point for the construction of a pair of computational models containing two HS iron(III) and four HS iron(II) ions, but different proton distributions on the three O atoms (O2, O1, and $O2^{III}$): (oxo, oxo, hydroxo) in model **DFT1**, and (hydroxo, oxo, oxo) in model **DFT2** (see Table 3.8.1 and Figure 3.8.1). Notice that the Fe site labelling in Figure 3.8.1 does not follow the

crystallographic scheme of Figure 3.1.1: 1 is the metal site within the tren-like pocket, while 2 and 3–6 are the apical and basal metal sites in the pentairon core, respectively. The HS states for each structure were used to avoid convergence problems anticipated for spin-coupled states, and all of the hydrogen atom positions were optimized. The electronic energy of **DFT2** calculated using B3LYP functional is 15 kcal mol^{-1} higher than that of **DFT1**, showing that the (oxo, oxo, hydroxo) isomer is energetically more stable than the (hydroxo, oxo, oxo) isomer. Owing to its higher electronic energy, **DFT2** was not considered in any of the following analyses, nor did we consider this proton distribution in our full geometry optimizations.

Table 3.8.1. Computational details for models **DFT1** to **DFT5**.

Model	Metal content and formal oxidation states	*S*	Oxygen ligands (O2, O1, $O2^{III}$)	(*i*, *j*); $J_{i,j}$ (cm^{-1})[a]	Functional
DFT1	$Fe^{II}_4Fe^{III}_2$	13	oxo, oxo, hydroxo	-	B3LYP
DFT2	$Fe^{II}_4Fe^{III}_2$	13	hydroxo, oxo, oxo	-	B3LYP
DFT3	$Fe^{II}_4Fe^{III}_2$	13	oxo, oxo, hydroxo	-	BP86
DFT4	$Fe^{II}_2Ga^{III}_2Zn^{II}_2$[b]	4	oxo, oxo, hydroxo	(5, 6); 930	BP86

[a]The Heisenberg Hamiltonian is defined as in PHI program,[53] i.e. $-2J_{i,j}\hat{\mathbf{S}}_i\cdot\hat{\mathbf{S}}_j$. [b]The model encompasses Fe at sites 5 and 6, Ga at sites 1 and 2, and Zn at the remaining metal sites.

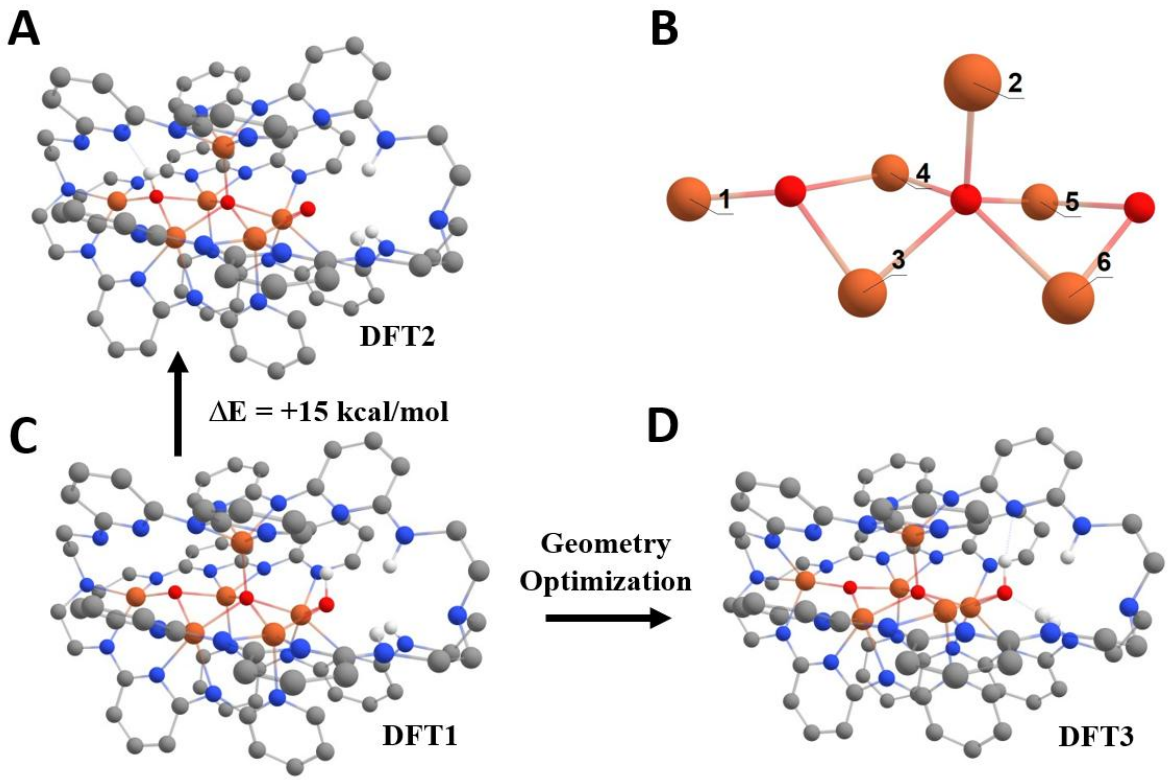

Figure 3.8.1. (**A**,**C**) Models **DFT1** and **DFT2** with hydrogen atom positions optimized. (**B**) Labeling scheme for metal ion sites. (**D**) Model **DFT3** with optimized positions for all atoms. In these diagrams, all hydrogen atoms bound to carbon have been omitted for clarity. See Supporting Information for full structural descriptions of **DFT1** to **DFT3**.

All atomic positions of **DFT1** were successfully optimized at the BP86 level of theory to give model **DFT3**. To evaluate the structural match of **DFT3** with X-ray diffraction data, we calculated the root mean square deviation (RMSD) of atomic positions from the crystallographic coordinates. This structural overlay considered the Fe, O, and N atoms only and gave RMSD = 0.26 Å. Despite the low RMSD, **DFT3** does exhibit some distortion from the crystallographic coordinates, most notably in the contraction of the Fe3–N2

distance (see Figure 3.8.1 and Table S5 in the published SI). The shortest Fe–Fe separation (2.71 Å) is found between sites 5 and 6, i.e. along the OH-bridged base edge of the $Fe_5(\mu_5\text{-}O)$ square pyramid, whereas the distance between sites 3 and 4 along the opposite base edge is 2.84 Å and the length of two remaining base edges is 2.95–3.07 Å.

The valence distribution in **DFT3** was checked by BVS calculations[36,54] and spin-population analysis. BVS values (Table 3.8.2) indicate clearly that sites 5 and 6 have the largest iron(II) character among the six metal sites. Spin-population analyses supports this assignment, indicating that sites 5 and 6 have the lowest spin population of the Fe atoms, consistent with HS iron(II) vs. HS iron(III) (see Table S6 in the published SI for full analysis). This optimized structure was subsequently used in a single-point calculation to predict Mössbauer parameters from the calculated wavefunction, specifically isomer shifts (δ), which are highly diagnostic of oxidation state, and quadrupole splittings (ΔE_Q), which report on the electric field gradient at each Fe site. It has been noted that quadrupole splittings for HS iron(II) and iron(III) are generally underestimated by GGA functionals such as BP86.[55] Indeed, the calculated ΔE_Q values (Table S7 in the published SI) do not help us to discriminate between the possible Mössbauer models. Mössbauer isomer shifts for **DFT3**, calculated using the methods outlined by Neese and coworkers,[56] are shown in Table 3.8.2. The calculated isomer shift for site 1 (0.58 mm s^{-1}) is at the high end of the HS iron(III) range, but at the low end for the HS iron(II) range.[50] This intermediate δ value may indicate some delocalization of the mixed valency. Notably, the average of the four lowest calculated isomer shifts is 0.71 mm s^{-1}, while the other two calculated δ values are 0.86 and 0.97 mm s^{-1}. Considering the expected error associated with the prediction of

Mössbauer isomer shifts using BP86 (~0.1 mm s^{-1}), these three values are in satisfactory agreement with the experimental values from **Fit3** and **Fit4** (0.71 mm s^{-1}, 0.89–1.00 mm s^{-1}, and 1.01–1.11 mm s^{-1}). From these results, we can establish that Mössbauer parameters from model **DFT3** with four HS iron(II) ions and two HS iron(III) ions are consistent with the available experimental data. Furthermore, in combination with BVS and spin-population analyses, they help assigning a prevalent HS iron(II) character to metal sites 5 and 6, while the remaining four metal sites ($Fe_2^{II}Fe_2^{III}$) display substantial valence delocalization.

An extensive network of weak Fe–Fe bonding interactions is indeed found in **DFT3**, as evidenced by Mayer bond order (*MBO*) values less than one, but greater than 0.1 (Table S8).[57] There are interactions (*MBO* = 0.14–0.45) between site 2 and two of the four Fe atoms that make up the roughly square basal plane of the pentairon core (sites 3, 4, 5, and 6). Several relatively strong interactions (*MBO* = 0.16–0.35) also occur between adjacent Fe atoms in the square base.

Table 3.8.2. BVS and isomer shift values (mm s^{-1}) for the six metal sites in **3** as obtained from model **DFT3**. Experimental isomer shifts from **Fit3** and **Fit4** are also reported for comparison.

Metal site[a]	BVS(Fe^{2+})[b]	BVS(Fe^{3+})[b]	BVS(Fe^{2+})[c]	δ from **DFT3**	δ from **Fit3** and **Fit4**[d]
1	2.165	2.471	2.276	0.58	
2	2.014	2.318	2.153	0.75	0.71 (4)
3	2.141	2.417	2.249	0.76	
4	2.110	2.388	2.221	0.76	
5	1.932	2.190	2.037	0.86	0.89–1.00 (1)
6	1.785	2.021	1.880	0.97	1.01–1.11 (1)

[a]For the labelling of metal sites, see Figure 3.8.1. [b]Using the standard set of Fe^{2+} or Fe^{3+} BVS parameters from file bvparm2020.cif available at https://www.iucr.org/resources/data/datasets/bond-valence-parameters and including only bond distances within 3.0 Å. See Table S2 in the published SI for details. [c]Using the specialized R_0 value for HS Fe^{2+} complexes with N_{py} and N_{am} donors and including only bond distances within 3.0 Å. See Table S2 and Figure S6 in the published SI for details. [d]Numbers in parentheses are the relative areas of the three subspectra.

We have further utilized DFT methods to probe magnetic interactions in **3**. Specifically, we decided to test the hypothesis, suggested by the magnetic susceptibility data, that the

compound contains a ferromagnetically coupled diiron(II,II) unit with a local *S* = 4 state that persists to room temperature. A full analysis of the spin ladder is impractical and would also be inaccurate. As an alternative, starting from optimized structure **DFT3**, we assigned sites 5 and 6 as iron(II) ions and magnetically isolated this metal pair by replacing all other metal ions with diamagnetic substitutes of similar ionic radius, namely gallium(III) for sites 1 and 2 and zinc(II) for the remaining metal sites (Figure 3.8.1). We do not expect this method to be quantitatively accurate, but we are confident it can be used to highlight any strong ferromagnetic within the given metal pair. We then performed broken symmetry single-point calculations on the resulting model (**DFT4**) to predict the exchange-coupling parameter *J* between these two Fe sites under the Heisenberg Hamiltonian (Table 3). The results indeed indicate very strong ferromagnetic exchange coupling, with a *J* value of several hundreds of wavenumbers. This diiron(II) unit is thus expected to remain ferromagnetically coupled to give an *S* = 4 state thermally persistent up to room temperature, consistent with the magnetic susceptibility data.

CONCLUSIONS

With their arrays of spatially organized N donors, oligo-α-pyridylamides and related ligands offer a viable route to polymetallic complexes showing a linear structure and, in many cases, metal–metal bonding (EMACs). Among first-row metals, iron is of special interest since short Fe–Fe separations often produce strong ferromagnetic couplings and large room temperature magnetic moments.[13,14] However, nuclearity is often lower (and Fe–Fe

distances are often longer) than expected from the ligand's structure.[14,16,17,30,58] Moreover, the high oxophilicity of Fe leads to the easy incorporation of adventitious oxygen atoms to yield iron-oxo cores.[29,30]

Our findings indicate that these tendencies can be further accompanied by partial oxidation of Fe. Attempts to access iron(II)-based EMACs were made by reacting the organometallic precursor $[Fe_2(Mes)_4]$ with a tridecadentate proligand containing a tren-like aliphatic pocket and three Hdpa-like arms (H_6L). The ligand's structure was designed to favor the assembling of Fe^{2+} ions into closely spaced linear arrays with metal–metal bond distances. The reaction instead resulted in the build up of an organic nanocage containing two tripodal ligands with interpenetrating branches and hosting a mixed-valence hexairon-oxo core. The formula and structure of the compound, $[Fe_6O_2(OH)(H_3L)L]$ (**3**), were inferred by combined use of EA, ESI-MS, electrochemical studies, X-ray crystallography, BVS analysis, and DFT calculations. In spite of the trigonal symmetry of the organic envelope, **3** displays a remarkably unsymmetric iron-oxo core orientationally disordered around a crystallographic D_3 position. The core was modelled as $[Fe(\mu_3\text{-}O)Fe_5(\mu_5\text{-}O)(\mu\text{-}OH)]^{9+}$, with a central $Fe_5(\mu_5\text{-}O)$ square pyramid supported by two additional oxygen bridges and a sixth Fe center located in the tren-like pocket of L^{6-}. Mössbauer spectra confirmed that **3** is a mixed-valence $Fe_4^{II}Fe_2^{III}$ species, containing two predominantly HS Fe^{II} sites and an extensively valence-delocalized $Fe_2^{II}Fe_2^{III}$ unit. Using BVS analysis and DFT calculations, the two unique metal sites were identified as a pair of closely spaced OH-bridged metals in the central $Fe_5(\mu_5\text{-}O)$ pyramid. Significantly, broken-symmetry DFT calculations anticipate strong ferromagnetic coupling within this pair to give a thermally persistent $S = 4$ state,

which explains the large magnetic moment of **3** at room temperature. As a final point of interest, slow magnetic relaxation was detected in the compound even in zero static field, with Orbach activation parameters U_{eff}/k_B= 49(2) K and $\tau_0 = 4(2)\cdot10^{-10}$ s.

EXPERIMENTAL

General procedures. All synthetic operations involving iron complexes were carried out inside an MBraun UNIlab glovebox under an inert and controlled dinitrogen atmosphere, continuously purified over activated charcoal, molecular sieves, and a copper oxygen scavenger (H_2O and O_2 < 1 ppm). All chemicals were of reagent grade and used as received, unless otherwise noted. Anhydrous toluene and 1,4-dioxane were purchased and used exclusively for operation inside the glovebox. Thf and Et_2O were pre-dried over KOH[59] and $CaCl_2$,[60] respectively, and subsequently distilled from their sodium diphenylketyl solutions before use. All the solvents (including thf-d_8) used inside the glovebox were deoxygenated through three freeze-pump-thaw cycles and stored over 4A molecular sieves (except for EtOH, which was simply stored over 3A molecular sieves). H_6L was prepared heating together *N*-(6-fluoropyridin-2-yl)pyridin-2-amine, H_6tren, and Cs_2CO_3 at 130 °C for 3 days in solvent-free conditions, as described elsewhere.[28] The purified material was isolated as H_6L·0.44EtOH. [$Fe_2(Mes)_4$] was synthesized from $Fe_4Cl_8(thf)_6$ [61] and MesMgBr in thf/1,4-dioxane.[62] TBATFB used as base electrolyte for electrochemical studies was recrystallized twice from EtOH/Et_2O (1:1 v/v) at −50 °C. The crystalline solid was filtered, washed with Et_2O, and dried under vacuum.[60]

Unless otherwise noted, all characterization data were collected with strict exclusion of air under a dinitrogen atmosphere. CHN content was determined using a ThermoFisher Scientific Flash 2000 analyzer, and implied the unavoidable exposure of the sample to the air for 30–60 s, whereupon it immediately turned from dark-red to black. The Fe content was determined by complexometric titration on a sample of **3** accurately weighted inside the glovebox and digested with HNO_3 and H_2O_2 in aerobic conditions (titrant: $Na_2EDTA{\cdot}2H_2O$, standardized using $Pb(NO_3)_2$ as a primary standard; indicator: xylenol orange).[63] ESI-MS measurements were conducted on a 6310A Ion Trap LC-MS(n) instrument (Agilent Technologies) by direct infusion of thf solutions, in positive ion mode. The electronic spectra in thf solution were recorded up to 2000 nm on a double beam UV-Vis-NIR Jasco V-570 spectrometer, using a quartz cuvette sealed with an air-tight Teflon® cap (optical path length l = 0.1 cm). The ^{1}H NMR spectrum was recorded at 298 K in thf-d_8 using a Bruker Avance400 FT-NMR spectrometer (400.13 MHz) and an air-tight Young-valved NMR tube. The chemical shifts are expressed in ppm downfield from Me_4Si as external standard, by setting the residual CH_2(3,4) signal of thf-d_8 at 1.72 ppm.[64] Abbreviation used: br = broad. Spectrum analysis was carried out with TopSpin 4.0.6 software.[65]

Synthesis. Inside a glovebox, $[Fe_2(Mes)_4]$ (265.6 mg, 0.4514 mmol) and $H_6L{\cdot}0.44EtOH$ (184.8 mg, 0.2742 mmol) were refluxed together in toluene (7 mL) for 3 h. During the reflux the suspension progressively turned from orange to dark red/brown. The reaction mixture was allowed to cool to room temperature, and the solution was then eliminated by filtration through a fritted glass filter (G4 porosity). The dark red solid was washed with fresh toluene

(1 mL) and extracted with thf (4 × 10 mL). One additional overnight extraction was performed with 20 mL of thf. The combined red extracts were evaporated under vacuum, to give the product as a red solid (134.0 mg, 0.07964 mmol, 58.1%). Anal. Calcd for **3**: C, 51.40; H, 4.19; N, 21.64; Fe, 19.91%. Calcd for **3**·0.4C_7H_8: C, 52.25; H, 4.29; N, 21.18; Fe, 19.49%. Found: C, 52.44; H, 4.18; N, 21.42; Fe, 19.70%. This red solid can be recrystallized from thf/Et_2O by slow liquid diffusion to afford small, dark red, trapezoidal plates of **3** (recrystallization yield ~50%). For all the following characterizations, except X-ray crystallography, crystals of **3** were removed from the mother solution, washed with a few drops of Et_2O, and well dried under vacuum.

Calcd for **3**·0.3Et_2O: C, 51.57; H, 4.32; N, 21.36; Fe, 19.65%. Found: C, 51.86; H, 4.12; N, 21.43%. ^{1}H NMR (thf-d_8, 298 K, 400.13 MHz): δ_H (ppm) = 3.38 (4H, br, Et_2O, CH_2), 1.11 (6H, br, Et_2O, CH_3). ESI-MS (thf, positive ion mode), *m*/*z*: 1680.2−1681.2 ($[Fe_6O_3H_2L_2]^+$ and $[Fe_6O_3H_3L_2]^+$, 0.8:0.2 ratio, 100); 1626.3−1627.3 ($[Fe_5O_3H_4L_2]^+$ and $[Fe_5O_3H_5L_2]^+$, 0.9:0.1 ratio, 10); 850.1 ($[Fe_3ClL]^+$, 3). UV-Vis-NIR (thf, $1.43 \cdot 10^{-4}$ M): λ_{max} (ε) = 242 nm ($1.03 \cdot 10^5$ M^{-1} cm^{-1}), 268 nm (sh), 341 nm ($6.83 \cdot 10^4$ M^{-1} cm^{-1}), ~380 nm (sh), ~500 nm (sh).

X-ray Crystallography. A plate-like crystal of **3** was covered with NVH immersion oil (Jena Bioscience), which efficiently protects the compound against degradation. Subsequently it was mounted on a MiTeGen Microloop™ and transferred to a Bruker-Nonius X8APEX diffractometer equipped with Mo-Kα generator, area detector and Kryoflex liquid dinitrogen cryostat for data collection at 115(2) K. Acquisition of matrix frames and data collection were carried out using APEX2 v1.0-22 software.[66] Data reduction used SAINT v7.06A program[66] and was followed by multi-scan absorption correction applied with SADABS

v2.10.[66] Programs SUPERFLIP[67,68] and SHELXL-2014/7,[69] implemented in the WINGX v2020.1 suite,[70] were used for structure solution and refinement on F_o^2, respectively. The measured crystal, and likewise all tested samples, was weakly diffracting and data collection was extended to a resolution of 0.84 Å ($2\theta_{max}$ = 50.0°) to give $\langle I/\sigma(I)\rangle$ = 6.74. The unit cell metrics and the symmetry of the diffraction pattern were consistent with trigonal crystal system, with *R*(merge) = 0.078, 0.073 and 0.048 in Laue classes $\bar{3}1m$ (hex), $\bar{3}$ (hex) and $\bar{1}$, respectively. Systematic absences were found to affect *hhl* reflections, which had $\langle I/\sigma(I)\rangle$ = −0.16 for odd *l* (320 reflections) and 10.29 for even *l* (311 reflections), strongly suggesting extinction symbol *P*- - *c* and space groups *P*31c (noncentric) or $P\bar{3}1c$ (centric). Structure solution in the centric space group followed by a Fourier synthesis gave the positions of all non-hydrogen atoms. All non-hydrogen atoms in the model were treated anisotropically, except for Fe3. Hydrogen atoms were added in calculated positions with U(H) = 1.2U_{eq}(C,N), including the half-occupancy secondary NH hydrogen of the 50-% unmetalated tren-like pocket, which was directly located in ΔF maps.

The structure of the central core was best revealed by a Fourier synthesis with phases based on the organic ligands alone (Figure S4). The most intense peak (Q1 = 8.11 eÅ^{-3}) and its symmetry equivalents define a slightly distorted trigonal prism, with the shortest separations of 2.67 and 3.12 Å. Each longer edge of the prism is capped by an additional peak (Q2 = 5.56 eÅ^{-3}) lying exactly on a twofold axis at 1.61 Å from the vertices. Other significant electron density residuals were found on the threefold axis, namely in the tren-like pockets of the ligands (Q3 = 4.57 eÅ^{-3}), at the center of the prism (Q4 = 4.52 eÅ^{-3}), and in triangular-face capping positions (Q5 = 3.93 eÅ^{-3}). Q1 and Q2 are at coordination-bond

distance from N atoms (2.02–2.33 Å) as well as from Q4 and Q5 (1.92–2.18 Å), suggesting that the former are partially-occupied metal sites, while the latter are O atoms. The Q1–Q2 distance is indeed unphysically short for a metal–metal contact and requires the central core to be severely disordered. Full anisotropic refinement with the above-suggested assignments (Q1 = Fe1, Q2 = Fe2, Q3 = Fe3, Q4 = O1, Q5 = O2) and free site occupancy factors (SOFs) gave SOF/U_{iso}(Å^2) = 0.634(6)/0.0424(6), 0.310(6)/0.0303(15), and 0.440(10)/0.096(3) for Fe1, Fe2, and Fe3, respectively; SOF/U_{iso}(Å^2) = 0.92(4)/0.030(4) and 1.09(3)/ 0.047(3) for O1 and O2, respectively. These results suggest 2:1 occupancies for Fe1 and Fe2, approximately half occupancy for Fe3 and full occupancies for O1 and O2. Anisotropic displacement parameters (ADPs) had physically reasonable values except for Fe3, which displayed a very oblate ellipsoid. The ADPs for the secondary N donors of the tren-like pocket were also distinctly elongated towards the metal, suggesting an off-axis position for Fe3. Slant plane ΔF maps normal to the trigonal axis indeed confirmed a pronounced threefold modulation of electron density around Fe3, but not around O1 and O2. Fe3 was then allowed to move off the threefold axis and treated isotropically, affording SOF/U_{iso}(Å^2) = 0.141(3)/0.034(2) for Fe3 and virtually unvaried parameters for the remaining core atoms. This result indicates clearly that, independent of how Fe3 is modelled, the tren-like pocket of the ligand is only ca. 40–50% occupied. Since both EA and ESI-MS consistently indicate six metal centers per molecule, fixed occupancies of 2/3, 1/3, and 1/6 were assigned to Fe1, Fe2, and Fe3, respectively, thereby imposing half occupancy of the tren-like pocket. Unit occupancies were instead used for O1 and O2. The 2:1 occupancies of Fe1 and Fe2 suggest a distorted square-pyramidal $Fe_5(\mu_5\text{-}O)$ core orientationally

disordered around the trigonal axis, with Fe2 as the apical site. BVS calculations (Table S2) support the assignment of central oxygen O1 as a μ_5-O^{2-} ligand. Furthermore, they are consistent with O2 being a μ_3-O^{2-} group when the neighboring tren-like pocket is metalated, and a μ-OH^- group otherwise. The severely disordered core requires the electron density of hydroxide hydrogen to be spread over six positions, thus explaining why it could not be located in ΔF maps. For this reason, the OH^- hydrogen atom was not included in the refinement. The rather high final *R*-indices at least partially reflect unaccounted for electron density located in the solvent-accessible voids of the structure. In fact, ^{1}H NMR spectroscopy (Figure S3) indicate that crystals of **3** retain traces of Et_2O even after prolonged treatment in vacuum, in accordance with EA. The solvent-accessible voids in the structure were calculated using the SQUEEZE command[71] implemented in PLATON.[72] This calculation showed that four solvent-accessible voids exist per unit cell, namely two 216-Å^3 voids (each containing 40 electrons) and two 126-Å^3 voids (each containing 43 electrons). The latter host the highest electron density residuals (2.0 *e*Å^{-3}) in the final ΔF map. Therefore, each of these voids can in principle host one Et_2O molecule, which contains 42 electrons and has a van der Waals volume of ~86.6 Å^3 (calculated using the method proposed by Abraham *et al.*).[73] We found that use of solvent-corrected *hkl* data lowers the *R*1 factor for reflections with $I \geq 2\sigma(I)$ from 8.5 to 5.6%. However, differences in molecular geometry are insignificant and we decided to stick to the results of refinement on pristine, uncorrected data. Graphics utilized ORTEP-3 for Windows v2014.1,[70] POV-Ray for Windows v3.7,[74] and Olex2-1.5.[75]

CCDC XXXXXXX contains the supplementary crystallographic data for this paper. These data can be obtained free of charge from The Cambridge Crystallographic Data Centre via www.ccdc.cam.ac.uk/structures (accessed on XX XXXX 2022), or by emailing data_request@ccdc.cam.ac.uk, or by contacting The Cambridge Crystallographic Data Centre, 12 Union Road, Cambridge CB2 1EZ, UK; fax: +44 1223 336033.

Mössbauer Spectroscopy. Solid state Mössbauer spectra of **3** were collected at 77 K and 10 K with a SEE Co model W304 resonant gamma-ray 1024 channel spectrometer with a ^{57}Co on Rh foil source. The velocity range used was ±4 mm s^{-1} and the experimental spectra were referenced to α-Fe foil at room temperature. The data collection was conducted with the sample under vacuum. Mössbauer data were fitted using an adaptive nonlinear least-squares algorithm developed by Dennis *et al.* and available within the WMOSS4F software.[76] Three quadrupole doublets were used to fit the experimental data. The parameters fitted were the isomer shift (δ), the quadrupole splitting (ΔE_Q), and the linewidths (i.e. the full widths at half maximum, Γ_{FWHM}). The relative areas of the subspectra were either allowed to vary or fixed to 4:1:1, as initially suggested by crystallographic symmetry with four basal sites and two additional independent sites (apical and pocket sites). However, we note that the DFT-optimized model deviates from this simplistic assignment and suggests that it is two of the basal sites that have the unique Mössbauer parameters.

Magnetic measurements. The magnetic measurements were obtained with a Quantum Design MPMS-XL SQUID magnetometer and a PPMS-9 susceptometer. The MPMS-XL instrument works between 1.86 and 400 K with applied static fields (H) ranging from –7 to 7

T. The sample for magnetic measurements was prepared with strict exclusion of dioxygen and moisture in a glovebox under argon. A polycrystalline sample of **3** (7.1 mg) was covered with Paratone® oil (10.2 mg) to avoid magnetic torqueing and introduced in a sealed polypropylene bag (3 × 0.5 × 0.02 cm; 20.9 mg). Prior to the experiments, the field-dependent magnetization was measured at 100 K to exclude the presence of bulk ferromagnetic impurities. All magnetic data were corrected for the sample holder and the intrinsic diamagnetism. The dc magnetic susceptibility (χ) was obtained as *M/H* from magnetization (*M*) measurements at 0.1 and 1 T in the temperature range 1.86–300 K. Isothermal magnetization data were also recorded between 1.86 and 8 K in fields up to 7 T. Above 1.86 K, no hysteresis effects were observed in the field dependence of the magnetization for field sweep rates between about 50 and 600 Oe min^{-1}. The ac susceptibility measurements down to 1.9 K were performed using an oscillating field of 1–6 Oe for frequencies from 10 Hz to 10 kHz and applied static fields of zero to 2 T (PPMS-9). In the available temperature and frequency ranges, the sample displayed slow relaxation of the magnetization observable in zero and in finite applied dc fields. All ac measurements were fitted to the generalized Debye model (using χ' and χ'' vs. ν data) in order to extract the characteristic relaxation time (τ), the α parameter describing the width of the distribution of relaxation times, as well as the values of χ_0 and χ_∞.

Electrochemistry. CV curves were recorded in thf using a PARSTAT 2273 Potentiostat/Galvanostat (Princeton Applied Research, Oak Ridge, USA). Experiments at different scan rates (v = 0.02–1 V s^{-1}) were carried out using a cell for small volume samples (~3 mL). A Pt ring, an Ag wire, and a 1 mm-diameter GC disk (Princeton Applied Research)

were used as counter, quasi-reference and working electrode, respectively. The GC electrode was cleaned as previously reported.[77] For all experiments, the potential of the quasi-reference electrode was calibrated against the ferrocenium/ferrocene redox couple.[78] All the reported potential values are referred to ferrocenium/ferrocene redox couple. To avoid degradation of the complex, all the measurements were performed in a MBraun UniLAB glovebox under dinitrogen at –10 °C. The concentration of **3** and of the base electrolyte (TBATFB) were 0.25 mM and 0.05 M, respectively. To minimize the ohmic drop between the working and the reference electrodes, careful feedback correction was applied. All the formal potential values ($E°'$) were calculated as the semi-sum of the cathodic and anodic peak potentials, i.e. $E°' = (E_{pc}+E_{pa})/2$. The dependence of $\Delta E_p = E_{pa} - E_{pc}$ on v allowed to obtain the standard heterogeneous ET rate constant k_{ET},[79] which is the ET rate constant measured at the formal potential $E°'$. The experiments were repeated at least four times and the k_{ET} values obtained were found to be reproducible within 6%. When necessary, deconvolution of voltammetry signals was performed using EG&G Condecon Software Package.

Conductivity measurements. Conductivity measurements were carried out in thf with a CRISON (mod. *micro*CM2201) conductivity meter using a cell of constant 1.14 cm^{-1} with a precision of 0.5%. They were made in a thermostatic bath at different temperatures (from –23 to 2 °C) maintained constant within ±0.1 °C; the concentration of **3** was 0.25 mM. The nature of the complex (neutral or ionic) was determined by comparing its molar conductivity values with those of ionic complexes measured in the same solvent and conditions.

DFT calculations. The initial atomic coordinates used in DFT studies were obtained from X-ray diffraction data, omitting crystallographic disorder and adding a hydrogen atom to O2 or $O2^{III}$. All hydrogen atom positions were then optimized in **DFT1** and **DFT2** while fixing the positions of all heavier atoms, whereas in **DFT3** all atomic positions were fully optimized. All calculations were performed using the ORCA 4.2.1 software package using unrestricted Kohn-Sham (UKS) DFT.[80] The def2-SVP basis set was used on all atoms except Fe, where the def2-TZVP basis set was used.[81] The numerical grid was increased to "Grid 4" in ORCA notation. Calculations on **DFT1** and **DFT2** were performed using the B3LYP functional with the dispersion correction D3.[82,83] Calculations on **DFT3**, including the evaluation of Mössbauer parameters, were performed using the BP86 functional.[82,83] In addition, the NBO package was employed in **DFT3** to obtain the natural population values.[84] The broken-symmetry single point calculations done on **DFT4** were also performed using BP86. Additionally, the resolution of identity (RI) approximation was applied to all the calculations.[85]

REFERENCES

(1) Zhu, L.-G.; Peng, S.-M. Linear Metal String Complexes with Oligo-α-Pyridylamine Ligands. *Chin. J. Inorg. Chem.* **2002**, *18* (2), 117 – 124.

(2) Berry, J. F. Extended Metal Atom Chains. In *Multiple Bonds between Metal Atoms*, 3rd ed.; Cotton, F. A., Murillo, C. A., Walton, R. A., Eds.; Springer Science & Business Media, Inc.: New York, 2005; pp 669–706. https://doi.org/10.1007/0-387-25829-9_15.

(3) Yeh, C.-Y.; Wang, C.-C.; Chen, C.-H.; Peng, S.-M. Molecular Metal Wires Built from a

Linear Metal Atom Chain Supported by Oligopyridylamido Ligands. In *Redox Systems under Nano-Space Control*; Hirao, T., Ed.; Springer-Verlag: Berlin Heidelberg, 2006; pp 85–117. https://doi.org/10.1007/3-540-29580-1_5.

(4) Po-Chun Liu, I.; Wang, W.-Z.; Peng, S.-M. New Generation of Metal String Complexes: Strengthening Metal–Metal Interaction via Naphthyridyl Group Modulated Oligo-α-Pyridylamido Ligands. *Chem. Commun.* **2009**, No. 29, 4323–4331. https://doi.org/10.1039/b904719k.

(5) Berry, J. F. Metal–Metal Bonds in Chains of Three or More Metal Atoms: From Homometallic to Heterometallic Chains. *Struct. Bond.* **2010**, *136*, 1–28. https://doi.org/10.1007/978-3-642-05243-9.

(6) Hua, S.-A.; Tsai, Y.-C.; Peng, S.-M. A Journey of Metal-Metal Bonding beyond Cotton's Quadruple Bonds. *J. Chin. Chem. Soc.* **2014**, *61* (1), 9–26. https://doi.org/10.1002/jccs.201300417.

(7) Hua, S.-A.; Cheng, M.-C.; Chen, C.-H.; Peng, S.-M. From Homonuclear Metal String Complexes to Heteronuclear Metal String Complexes. *Eur. J. Inorg. Chem.* **2015**, *2015* (15), 2510–2523. https://doi.org/10.1002/ejic.201403237.

(8) Chipman, J. A.; Berry, J. F. Paramagnetic Metal–Metal Bonded Heterometallic Complexes. *Chem. Rev.* **2020**, *120* (5), 2409–2447. https://doi.org/10.1021/acs.chemrev.9b00540.

(9) Berry, J. F.; Roy, M. D. 2-Aminopyridine and Related Ligands to Support Metal-Metal

Bonded Compounds. In *Comprehensive Coordination Chemistry III, Vol.1*, 3rd ed.; Constable, E. C., Parkin, G., Que, Jr., L., Figueroa, J. S., Eds.; Elsevier: Amsterdam, 2021; pp 406–427. https://doi.org/10.1016/B978-0-08-102688-5.00075-1.

(10) Brogden, D. W.; Berry, J. F. Coordination Chemistry of 2,2'-Dipyridylamine: The Gift That Keeps on Giving. *Comments Inorg. Chem.* **2016**, *36* (1), 17–37. https://doi.org/10.1080/02603594.2015.1079522.

(11) Allen, F. H. The Cambridge Structural Database: A Quarter of a Million Crystal Structures and Rising. *Acta Crystallogr. Sect. B Struct. Sci.* **2002**, *58* (3), 380–388. https://doi.org/10.1107/S0108768102003890.

(12) Shieh, S.-J.; Chou, C.-C.; Lee, G.-H.; Wang, C.-C.; Peng, S.-M. Linear Pentanuclear Complexes Containing a Chain of Metal Atoms:$[Co_5^{II}(M_5\text{-}Tpda)_4(NCS)_2]$ and $[Ni_5^{II}(M_5\text{-}Tpda)_4Cl_2]$. *Angew. Chem. Int. Ed.* **1997**, *36* (1–2), 56–59. https://doi.org/10.1002/anie.199700561.

(13) Guillet, G. L.; Arpin, K. Y.; Boltin, A. M.; Gordon, J. B.; Rave, J. A.; Hillesheim, P. C. Synthesis and Characterization of a Linear Triiron(II) Extended Metal Atom Chain Complex with Fe–Fe Bonds. *Inorg. Chem.* **2020**, *59* (16), 11238–11243. https://doi.org/10.1021/acs.inorgchem.0c01625.

(14) Srinivasan, A.; Musgrave, R. A.; Rouzières, M.; Clérac, R.; McGrady, J. E.; Hillard, E. A. A Linear Metal–Metal Bonded Tri-Iron Single-Molecule Magnet. *Chem. Commun.* **2021**, *57* (98), 13357–13360. https://doi.org/10.1039/D1CC05043E.

(15) Szarek, P.; Wegner, W.; Grochala, W. Ferromagnetic Ground State for a Hypothetical Iron-Based Extended Metal Atom Chain. *J. Mol. Model.* **2016**, *22* (3), 63. https://doi.org/10.1007/s00894-016-2928-x.

(16) Nicolini, A.; Galavotti, R.; Barra, A.-L.; Borsari, M.; Caleffi, M.; Luo, G.; Novitchi, G.; Park, K.; Ranieri, A.; Rigamonti, L.; Roncaglia, F.; Train, C.; Cornia, A. Filling the Gap in Extended Metal Atom Chains: Ferromagnetic Interactions in a Tetrairon(II) String Supported by Oligo-α-Pyridylamido Ligands. *Inorg. Chem.* **2018**, *57* (9), 5438–5448. https://doi.org/10.1021/acs.inorgchem.8b00405.

(17) Nicolini, A.; Affronte, M.; SantaLucia, D. J.; Borsari, M.; Cahier, B.; Caleffi, M.; Ranieri, A.; Berry, J. F.; Cornia, A. Tetrairon(II) Extended Metal Atom Chains as Single-Molecule Magnets. *Dalton Trans.* **2021**, *50* (22), 7571–7589. https://doi.org/10.1039/D1DT01007G.

(18) Chan, Z.-K.; Wu, Y.-Y.; Chen, J.-D.; Yeh, C.-Y.; Wang, C.-C.; Tsai, Y.-F.; Wang, J.-C. Linear and Cyclic Tetranuclear Copper(I) Complexes Containing Anions of N,N'-Bis(Pyrimidine-2-Yl)Formamidine. *Dalton Trans.* **2005**, No. 5, 985–990. https://doi.org/10.1039/B417911K.

(19) Krämer, C.; Leingang, S.; Hübner, O.; Kaifer, E.; Wadepohl, H.; Himmel, H.-J. Construction of Copper Chains with New Fluorescent Guanidino-Functionalized Naphthyridine Ligands. *Dalton Trans.* **2016**, *45* (42), 16966–16983. https://doi.org/10.1039/C6DT03166H.

(20) Cotton, F. A.; Daniels, L. M.; Falvello, L. R.; Matonic, J. H.; Murillo, C. A. Trigonal-

Lantern Dinuclear Compounds of Diiron(I,II): The Synthesis and Characterization of Two Highly Paramagnetic Fe2(Amidinato)3 Species with Short Metal-Metal Bonds. *Inorg. Chim. Acta* **1997**, *256* (2), 269–275. https://doi.org/10.1016/S0020-1693(96)05469-2.

(21) Cotton, F. A.; Daniels, L. M.; Maloney, D. J.; Matonic, J. H.; Murillo, C. A. Dicobalt Trigonal Lanterns: Compounds Containing the Co23+ Core Co2[RC(NPh)2]3 (R = H, C6H5) and an Oxidized Compound {Co2[HC(NPh)2]3(CH3CN)2}PF6. *Inorg. Chim. Acta* **1997**, *256* (2), 283–289. https://doi.org/10.1016/S0020-1693(96)05471-0.

(22) Murillo, C. A. The δ Bond and Trigonal Paddlewheels Before the Dawn of the Quintuple Bond. *Comments Inorg. Chem.* **2015**, *35* (1), 39–58. https://doi.org/10.1080/02603594.2014.1002033.

(23) Tsai, Y.-C.; Hsu, C.-W.; Yu, J.-S. K.; Lee, G.-H.; Wang, Y.; Kuo, T.-S. Remarkably Short Metal-Metal Bonds: A Lantern-Type Quintuply Bonded Dichromium(I) Complex. *Angew. Chem. Int. Ed.* **2008**, *47* (38), 7250–7253. https://doi.org/10.1002/anie.200801286.

(24) Harisomayajula, N. V. S.; Nair, A. K.; Tsai, Y.-C. Discovering Complexes Containing a Metal–Metal Quintuple Bond: From Theory to Practice. *Chem. Commun.* **2014**, *50* (26), 3391–3412. https://doi.org/10.1039/C3CC48203K.

(25) Nair, A. K.; Harisomayajula, N. V. S.; Tsai, Y.-C. The Lengths of the Metal-to-Metal Quintuple Bonds and Reactivity Thereof. *Inorg. Chim. Acta* **2015**, *424*, 51–62. https://doi.org/10.1016/j.ica.2014.09.020.

(26) Noor, A.; Kempe, R. M5M – Key Compounds of the Research Field Metal–Metal Quintuple Bonding. *Inorg. Chim. Acta* **2015**, *424*, 75–82. https://doi.org/10.1016/j.ica.2014.08.030.

(27) Tereniak, S. J.; Carlson, R. K.; Clouston, L. J.; Young, V. G.; Bill, E.; Maurice, R.; Chen, Y.-S.; Kim, H. J.; Gagliardi, L.; Lu, C. C. Role of the Metal in the Bonding and Properties of Bimetallic Complexes Involving Manganese, Iron, and Cobalt. *J. Am. Chem. Soc.* **2014**, *136* (5), 1842–1855. https://doi.org/10.1021/ja409016w.

(28) Nicolini, A.; Anderlini, B.; Roncaglia, F.; Cornia, A. An Efficient Transition-Metal-Free Route to Oligo-α-Pyridylamines via Fluoroarenes. *C. R. Chim.* **2023**, *26* (G1), 51–62. https://doi.org/10.5802/crchim.223.

(29) Reis, D. M.; Nunes, G. G.; Sá, E. L.; Friedermann, G. R.; Mangrich, A. S.; Evans, D. J.; Hitchcock, P. B.; Leigh, G. J.; Soares, J. F. Iron(III) and Titanium(IV) Oxoalkoxide Chemistry: Synthetic, Structural, Magnetochemical and Spectroscopic Studies of [Ti3(M3-OPri)2(μ-OPri)3(OPri)6][FeCl4] and [Fe5(M5-O)(μ-OPri)8Cl5]. *New J. Chem.* **2004**, *28* (9), 1168–1176. https://doi.org/10.1039/B403899A.

(30) Kusserow, M.; Spandl, J. Alkoholyse von [Fe2(OtBu)6] Als Einfacher Weg Zu Neuen Eisen(III)-Alkoxo-Verbindungen: Synthesen Und Kristallstrukturen von [Fe2(OtAmyl)6], [Fe5OCl(OiPr)12], [Fe5O(OiPr)13], [Fe5O(OiBu)13], [Fe5O(OCH2CF3)13], [Fe5O(OnPr)13] Und [Fe9O3(OnPr)21] ·iPrOH. *Zeitschrift für Anorg. und Allg. Chemie* **2006**, *632* (5), 885–892. https://doi.org/10.1002/zaac.200500474.

(31) Simas, A. B. C.; Pereira, V. L. P.; Barreto Jr., C. B.; Sales, D. L. de; Carvalho, L. L. de. An Expeditious and Consistent Procedure for Tetrahydrofuran (THF) Drying and Deoxygenation by the Still Apparatus. *Quim. Nova* **2009**, *32* (9), 2473–2475. https://doi.org/10.1590/S0100-40422009000900042.

(32) Armarego, W. L. F. Purification of Laboratory Chemicals, 8th ed.; Elsevier, Ed.; Butterworth-Heinemann: Oxford, UK, 2017.

(33) Zhao, H.; Clérac, R.; Sun, J.-S.; Ouyang, X.; Clemente-Juan, J. M.; Gomez-Garcia, C. J.; Coronado, E.; Dunbar, K. R. A Comparative Structural and Magnetic Study of Three Compounds Based on the Cluster Unit M4Cl8(THF)6 (M=Mn, Fe, Co). *J. Solid State Chem.* **2001**, *159* (2), 281–292. https://doi.org/10.1006/jssc.2001.9157.

(34) Klose, A.; Solari, E.; Floriani, C.; Chiesi-Villa, A.; Rizzoli, C.; Re, N. Magnetic Properties Diagnostic for the Existence of Iron(II)-Iron(II) Bonds in Dinuclear Complexes Which Derive from Stepwise Insertion Reactions on Unsupported Iron-Aryl Bonds. *J. Am. Chem. Soc.* **1994**, *116* (20), 9123–9135. https://doi.org/10.1021/ja00099a030.

(35) Jeffery, G. H.; Basset, J.; Mendham, J.; Denney, R. C. Vogel's Textbook of Quantitative Chemical Analysis, 5th ed.; Technical, L. S.: Essex, UK, 1989.

(36) Fulmer, G. R.; Miller, A. J. M.; Sherden, N. H.; Gottlieb, H. E.; Nudelman, A.; Stoltz, B. M.; Bercaw, J. E.; Goldberg, K. I. NMR Chemical Shifts of Trace Impurities: Common Laboratory Solvents, Organics, and Gases in Deuterated Solvents Relevant to the Organometallic Chemist. *Organometallics* **2010**, *29* (9), 2176–2179.

https://doi.org/10.1021/om100106e.

(37) Bruker. TopSpin 4.0.6; Bruker AXS Inc.: Madison, Wisconsin, USA, 2018.

(38) APEX2, SADABS, SAINT; Bruker-AXS, Inc.: Madison, Wisconsin, USA, 2012.

(39) Palatinus, L.; Chapuis, G. SUPERFLIP – a Computer Program for the Solution of Crystal Structures by Charge Flipping in Arbitrary Dimensions. *J. Appl. Crystallogr.* **2007**, *40* (4), 786–790. https://doi.org/10.1107/S0021889807029238.

(40) Palatinus, L.; Prathapa, S. J.; van Smaalen, S. EDMA: A Computer Program for Topological Analysis of Discrete Electron Densities. *J. Appl. Crystallogr.* **2012**, *45* (3), 575–580. https://doi.org/10.1107/S0021889812016068.

(41) Sheldrick, G. M. Crystal Structure Refinement with SHELXL. *Acta Crystallogr. Sect. C Struct. Chem.* **2015**, *71* (1), 3–8. https://doi.org/10.1107/S2053229614024218.

(42) Farrugia, L. J. WinGX and ORTEP for Windows: An Update. *J. Appl. Crystallogr.* **2012**, *45* (4), 849–854. https://doi.org/10.1107/S0021889812029111.

(43) Spek, A. L. PLATON SQUEEZE: A Tool for the Calculation of the Disordered Solvent Contribution to the Calculated Structure Factors. *Acta Crystallogr. Sect. C Struct. Chem.* **2015**, *71* (1), 9–18. https://doi.org/10.1107/S2053229614024929.

(44) Spek, A. L. Single-Crystal Structure Validation with the Program PLATON. *J. Appl. Crystallogr.* **2003**, *36* (1), 7–13. https://doi.org/10.1107/S0021889802022112.

(45) Zhao, Y. H.; Abraham, M. H.; Zissimos, A. M. Fast Calculation of van Der Waals Volume as a Sum of Atomic and Bond Contributions and Its Application to Drug

Compounds. *J. Org. Chem.* **2003**, *68* (19), 7368–7373. https://doi.org/10.1021/jo034808o.

(46) Persistence of Vision (TM) Raytracer (Version 3.7); Persistence of Vision Pty. Ltd.: Williamstown, Victoria, Australia, 2021.

(47) Dolomanov, O. V.; Bourhis, L. J.; Gildea, R. J.; Howard, J. A. K.; Puschmann, H. OLEX2: A Complete Structure Solution, Refinement and Analysis Program. *J. Appl. Crystallogr.* **2009**, *42* (2), 339–341. https://doi.org/10.1107/S0021889808042726.

(48) Dennis, J. E.; Gay, D. M.; Walsh, R. E. An Adaptive Nonlinear Least-Squares Algorithm. *ACM Trans. Math. Softw.* **1981**, *7* (3), 348–368. https://doi.org/10.1145/355958.355965.

(49) Belèn Meneses, A.; Antonello, S.; Arévalo, M. C.; Maran, F. Double-Layer Correction for Electron-Transfer Kinetics at Glassy Carbon and Mercury Electrodes in N,N-Dimethylformamide. *Electroanalysis* **2006**, *18* (4), 363–370. https://doi.org/10.1002/elan.200503419.

(50) Antonello, S.; Arrigoni, G.; Dainese, T.; De Nardi, M.; Parisio, G.; Perotti, L.; René, A.; Venzo, A.; Maran, F. Electron Transfer through 3D Monolayers on Au25 Clusters. *ACS Nano* **2014**, *8* (3), 2788–2795. https://doi.org/10.1021/nn406504k.

(51) Nicholson, R. S. Theory and Application of Cyclic Voltammetry for Measurement of Electrode Reaction Kinetics. *Anal. Chem.* **1965**, *37* (11), 1351–1355. https://doi.org/10.1021/ac60230a016.

(52) Neese, F. The ORCA Program System. *Wiley Interdiscip. Rev. Comput. Mol. Sci.* **2012**, *2* (1), 73–78. https://doi.org/10.1002/wcms.81.

(53) Weigend, F.; Ahlrichs, R. Balanced Basis Sets of Split Valence, Triple Zeta Valence and Quadruple Zeta Valence Quality for H to Rn: Design and Assessment of Accuracy. *Phys. Chem. Chem. Phys.* **2005**, *7* (18), 3297–3305. https://doi.org/10.1039/b508541a.

(54) Grimme, S.; Antony, J.; Ehrlich, S.; Krieg, H. A Consistent and Accurate Ab Initio Parametrization of Density Functional Dispersion Correction (DFT-D) for the 94 Elements H-Pu. *J. Chem. Phys.* **2010**, *132* (15), 154104. https://doi.org/10.1063/1.3382344.

(55) Grimme, S.; Ehrlich, S.; Goerigk, L. Effect of the Damping Function in Dispersion Corrected Density Functional Theory. *J. Comput. Chem.* **2011**, *32* (7), 1456–1465. https://doi.org/10.1002/jcc.21759.

(56) Weinhold, F. Natural Bond Orbital Analysis: A Critical Overview of Relationships to Alternative Bonding Perspectives. *J. Comput. Chem.* **2012**, *33* (30), 2363–2379. https://doi.org/10.1002/jcc.23060.

(57) Weigend, F. Accurate Coulomb-Fitting Basis Sets for H to Rn. *Phys. Chem. Chem. Phys.* **2006**, *8* (9), 1057–1065. https://doi.org/10.1039/b515623h.

(58) Cotton, F. A.; Daniels, L. M.; Jordan, G. T.; Murillo, C. A.; Pascual, I. Structural Variations in the Ligands around a Simple Oxo-Centered Building Block, the

Tetrahedral [M4O]6+ Unit, M=Mn and Fe. *Inorg. Chim. Acta* **2000**, *297* (1–2), 6–10. https://doi.org/10.1016/S0020-1693(99)00252-2.

(59) Sundberg, J.; Vad, M. S.; McGrady, J. E.; Björemark, P. M.; Håkansson, M.; McKenzie, C. J. Accessing Iron Amides from Dimesityliron. *J. Organomet. Chem.* **2015**, *786*, 40–47. https://doi.org/10.1016/j.jorganchem.2015.03.015.

(60) Addison, A. W.; Rao, T. N.; Reedijk, J.; van Rijn, J.; Verschoor, G. C. Synthesis, Structure, and Spectroscopic Properties of Copper(II) Compounds Containing Nitrogen–Sulphur Donor Ligands; the Crystal and Molecular Structure of Aqua[1,7-Bis(N-Methylbenzimidazol-2'-Yl)-2,6-Dithiaheptane]Copper(II) Perchlorate. *J. Chem. Soc., Dalton Trans.* **1984**, No. 7, 1349–1356. https://doi.org/10.1039/DT9840001349.

(61) Pauling, L. Metal-Metal Bond Lengths in Complexes of Transition Metals. *Proc. Natl. Acad. Sci.* **1976**, *73* (12), 4290–4293. https://doi.org/10.1073/pnas.73.12.4290.

(62) SantaLucia, D. J.; Berry, J. F. Antiferromagnetic Exchange and Metal–Metal Bonding in Roussin's Black Sulfur and Selenium Salts. *Inorg. Chem.* **2021**, *60* (21), 16241–16255. https://doi.org/10.1021/acs.inorgchem.1c02052.

(63) O'Keefe, B. J.; Monnier, S. M.; Hillmyer, M. A.; Tolman, W. B. Rapid and Controlled Polymerization of Lactide by Structurally Characterized Ferric Alkoxides. *J. Am. Chem. Soc.* **2001**, *123* (2), 339–340. https://doi.org/10.1021/ja003537l.

(64) Joy, M. T. R.; Bhoumik, N. C.; Ghosh, S.; Richmond, M. G.; Kabir, S. E. A New Synthetic Route for the Preparation of [Os3(CO)10(μ-OH)(μ-H)] and Its Reaction with

Bis(Diphenylphosphino)Methane (Dppm): Syntheses and X-Ray Structures of Two Isomers of [Os3(CO)8(μ-OH)(μ-H)(μ-Dppm)] and [Os3(CO)7(M3-CO)(μ 3-O)(μ-Dppm)]. *RSC Adv.* **2020**, *10* (73), 44699–44711. https://doi.org/10.1039/D0RA08783A.

(65) Brown, I. D. Recent Developments in the Methods and Applications of the Bond Valence Model. *Chem. Rev.* **2009**, *109* (12), 6858–6919. https://doi.org/10.1021/cr900053k.

(66) Steiner, T. The Hydrogen Bond in the Solid State. *Angew. Chem. Int. Ed.* **2002**, *41* (1), 48–76. https://doi.org/10.1002/1521-3773(20020104)41:1<48::AID-ANIE48>3.0.CO;2-U.

(67) Jeffrey, G. A. An Introduction to Hydrogen Bonding; Oxford University Press: New York, USA, 1997.

(68) Paredes-García, V.; Venegas-Yazigi, D.; Latorre, R. O.; Spodine, E. Electronic Properties of Mixed Valence Iron(II,III) Dinuclear Complexes with Carboxylate Bridges. *Polyhedron* **2006**, *25* (9), 2026–2032. https://doi.org/10.1016/j.poly.2006.01.006.

(69) Wałęsa-Chorab, M.; Banasz, R.; Marcinkowski, D.; Kubicki, M.; Patroniak, V. Electrochromism and Electrochemical Properties of Complexes of Transition Metal Ions with Benzimidazole-Based Ligand. *RSC Adv.* **2017**, *7* (80), 50858–50867. https://doi.org/10.1039/C7RA10451K.

(70) Wang, L.; Hao, J.; Zhai, L.-X.; Zhang, Y.; Dong, W.-K. Synthesis, Crystal Structure, Luminescence, Electrochemical and Antimicrobial Properties of Bis(Salamo)-Based Co(II) Complex. *Crystals* **2017**, *7* (9), 277. https://doi.org/10.3390/cryst7090277.

(71) Geiger, W. E.; Connelly, N. G. The Electron-Transfer Reactions of Polynuclear Organotransition Metal Complexes. *Adv. Organomet. Chem.* **1985**, *24*, 87–130. https://doi.org/10.1016/S0065-3055(08)60414-1.

(72) Daniel, C.; Hartl, H. Neutral and Cationic VIV/VV Mixed-Valence Alkoxo-Polyoxovanadium Clusters [V6O7(OR)12]N+ (R = −CH3, −C2H5): Structural, Cyclovoltammetric and IR-Spectroscopic Investigations on Mixed Valency in a Hexanuclear Core. *J. Am. Chem. Soc.* **2005**, *127* (40), 13978–13987. https://doi.org/10.1021/ja052902b.

(73) Gagne, R. R.; Spiro, C. L. An Electrochemical Method for Measuring Electronic Delocalization in Mixed-Valent Species. *J. Am. Chem. Soc.* **1980**, *102* (4), 1443–1444. https://doi.org/10.1021/ja00524a048.

(74) Richardson, D. E.; Taube, H. Determination of E20-E10 in Multistep Charge Transfer by Stationary-Electrode Pulse and Cyclic Voltammetry: Application to Binuclear Ruthenium Ammines. *Inorg. Chem.* **1981**, *20* (4), 1278–1285. https://doi.org/10.1021/ic50218a062.

(75) Santi, S.; Bisello, A.; Cardena, R.; Donoli, A. Key Multi(Ferrocenyl) Complexes in the Interplay between Electronic Coupling and Electrostatic Interaction. *Dalton Trans.* **2015**, *44* (12), 5234–5257. https://doi.org/10.1039/C4DT03581J.

(76) Ludi, A. Mixed-Valence Compounds: Theory and Applications in Chemistry, Physics, Geology, and Biology; Brown, D. B., Ed.; D. Reidel Publishing Company: Dordrecht, 1980.

(77) Zhao, Q.; Harris, T. D.; Betley, T. A. [(HL)2Fe6(NCMe)m]N+ (m = 0, 2, 4, 6; n = −1, 0, 1, 2, 3, 4, 6): An Electron-Transfer Series Featuring Octahedral Fe6 Clusters Supported by a Hexaamide Ligand Platform. *J. Am. Chem. Soc.* **2011**, *133* (21), 8293–8306. https://doi.org/10.1021/ja2015845.

(78) Zhao, Q.; Betley, T. A. Synthesis and Redox Properties of Triiron Complexes Featuring Strong Fe-Fe Interactions. *Angew. Chem. Int. Ed.* **2011**, *50* (3), 709–712. https://doi.org/10.1002/anie.201005198.

(79) Brodsky, C. N.; Hadt, R. G.; Hayes, D.; Reinhart, B. J.; Li, N.; Chen, L. X.; Nocera, D. G. In Situ Characterization of Cofacial Co(IV) Centers in Co4O4 Cubane: Modeling the High-Valent Active Site in Oxygen-Evolving Catalysts. *Proc. Natl. Acad. Sci.* **2017**, *114* (15), 3855–3860. https://doi.org/10.1073/pnas.1701816114.

(80) Atwood, J. L.; Hunter, W. E.; Rogers, R. D.; Holton, J.; McMeeking, J.; Pearce, R.; Lappert, M. F. Neutral and Anionic Silylmethyl Complexes of the Group 3a and Lanthanoid Metals; the X-Ray Crystal and Molecular Structure of [Li(Thf)4][Yb{CH(SiMe3)2}3Cl](Thf = Tetrahydrofuran). *J. Chem. Soc. Chem. Commun.* **1978**, No. 3, 140–142. https://doi.org/10.1039/c39780000140.

(81) Geary, W. J. The Use of Conductivity Measurements in Organic Solvents for the Characterisation of Coordination Compounds. *Coord. Chem. Rev.* **1971**, *7* (1), 81–

122. https://doi.org/10.1016/S0010-8545(00)80009-0.

(82) Gütlich, P.; Eckhard, B.; Trautwein, A. X. Mössbauer Spectroscopy and Transition Metal Chemistry: Fundamentals and Applications; Springer-Verlag: Berlin Heidelberg, 2011.

(83) Cotton, F. A.; Daniels, L. M.; Murillo, C. A. Divalent Iron Formamidinato Complexes: A Highly Distorted Dinuclear Compound. *Inorg. Chim. Acta* **1994**, *224* (1–2), 5–9. https://doi.org/10.1016/0020-1693(94)04146-6.

(84) Timmer, G. H.; Berry, J. F. Jahn-Teller Distortion, Ferromagnetic Coupling, and Electron Delocalization in a High-Spin Fe–Fe Bonded Dimer. *C. R. Chim.* **2012**, *15* (2–3), 192–201. https://doi.org/10.1016/j.crci.2011.09.001.

(85) Chilton, N. F.; Anderson, R. P.; Turner, L. D.; Soncini, A.; Murray, K. S. PHI: A Powerful New Program for the Analysis of Anisotropic Monomeric and Exchange-Coupled Polynuclear d- and f-Block Complexes. *J. Comput. Chem.* **2013**, *34* (13), 1164–1175. https://doi.org/10.1002/jcc.23234.

(86) Launay, M.; Boucher, F.; Gressier, P.; Ouvrard, G. A DFT Study of Lithium Battery Materials: Application to the β-VOXO4 Systems (X=P, As, S). *J. Solid State Chem.* **2003**, *176* (2), 556–566. https://doi.org/10.1016/S0022-4596(03)00331-1.

(87) Pápai, M.; Vankó, G. On Predicting Mössbauer Parameters of Iron-Containing Molecules with Density-Functional Theory. *J. Chem. Theory Comput.* **2013**, *9* (11), 5004–5020. https://doi.org/10.1021/ct4007585.

(88) Römelt, M.; Ye, S.; Neese, F. Calibration of Modern Density Functional Theory Methods for the Prediction of 57Fe Mössbauer Isomer Shifts: Meta-GGA and Double-Hybrid Functionals. *Inorg. Chem.* **2009**, *48* (3), 784–785. https://doi.org/10.1021/ic801535v.

(89) Mayer, I. Bond Order and Valence: Relations to Mulliken's Population Analysis. *Int. J. Quantum Chem.* **1984**, *26* (1), 151–154. https://doi.org/10.1002/qua.560260111.

(90) Korendovych, I. V.; Kryatov, S. V.; Reiff, W. M.; Rybak-Akimova, E. V. Diiron(II) μ-Aqua-μ-Hydroxo Model for Non-Heme Iron Sites in Proteins. *Inorg. Chem.* **2005**, *44* (24), 8656–8658. https://doi.org/10.1021/ic051739i.

(91) Yan Zang; Jang, H. G.; Chiou, Y.-M.; Hendrich, M. P.; Que, L. Structures and Properties of Ferromagnetically Coupled Bis(μ-Halo)Diiron(II) Complexes. *Inorg. Chim. Acta* **1993**, *213* (1–2), 41–48. https://doi.org/10.1016/S0020-1693(00)83812-8.

(92) Spiro, C. L.; Lambert, S. L.; Smith, T. J.; Duesler, E. N.; Gagne, R. R.; Hendrickson, D. N. Binuclear Complexes of Macrocyclic Ligands: Variation of Magnetic Exchange Interaction in a Series of Six-Coordinate Iron(II), Cobalt(II), and Nickel(II) Complexes and the x-Ray Structure of a Binuclear Iron(II) Macrocyclic Ligand Complex. *Inorg. Chem.* **1981**, *20* (4), 1229–1237. https://doi.org/10.1021/ic50218a053.

(93) Maddock, L. C. H.; Borilovic, I.; McIntyre, J.; Kennedy, A. R.; Aromí, G.; Hevia, E. Synthetic, Structural and Magnetic Implications of Introducing 2,2'-Dipyridylamide to Sodium-Ferrate Complexes. *Dalton Trans.* **2017**, *46* (20), 6683–6691. https://doi.org/10.1039/C7DT01319A.

Chapter 4: Asymmetric Ligand Field Effects in Electron-Rich Heterometallic Extended Metal Atom Chain Compounds

Rebecca K. Walde, Trey C. Pankratz, Amelia M. Wheaton, Milton Acosta, and John F. Berry

TCP conducted the DFT reaction mechanism studies of ligand rearrangement.

This work has been submitted and is under review to Chemistry – A European Journal.

Abstract: In heterometallic systems, electron donation from the ligands may influence the metal atoms in either a symmetric or asymmetric way, with the expected case being that the more electronegative metal is favored. Here, we describe a systematic study of heterometallic compounds here where this expectation is not observed. In this study, we use a modification of the symmetric 2,2'-dipyridylamine (dpa) ligand with electron donating ethyl groups, 4,4'-diethyl-2,2'-dipyridylamine ligand (dedpa), to prepare heterometallic extended metal atom chain (HEMAC) complexes with formula $Mo_2M'(dedpa)_4Cl_2$ (M' = Cr, Mn, Fe, Co, Ni). The effects of the electron donating substituents were studied through techniques including magnetometry, cyclic voltammetry, EPR, Mössbauer, electronic absorption spectroscopy, and DFT calculations. We find that the new HEMACs are indeed more electron rich, easier to oxidize, and, most interestingly, the impact of the ethyl substituents is not applied equally to all the metals in the chain. The ligand field is stronger at the Mo_2 site, but is surprisingly weaker at the M' center when compared to $Mo_2M'(dpa)_4Cl_2$ complexes. We also find that changing the ligand field allows for previously

unassigned electronic transitions to become visible, including excitations tentatively assigned to a triplet δ-δ* state within the Mo_2 unit.

Section 1: Introduction

Metal-metal bonded complexes have long been of interest for their unique properties and reactivity.[1-2] The simplest of these systems, homo-bimetallic complexes, have been well studied for many of the transition metals.[3-5] While many studies focus on metal identity as the primary driver of reactivity and electronic properties (a factor whose importance certainly cannot be denied), attention must also be given to the ligands that support the metal-metal bonds. Many bimetallic and larger clusters rely on easily modifiable ligands such as carboxylates,[6-13] NHCs,[14] pincer ligands,[15] nitrogen containing heterocycles,[4, 14] and many more.[16-19] As should be expected, these supporting ligands can have a large impact on the electronics of the resulting compound. However, studies on the impact of ligands with electron donating/withdrawing substituents have focused primarily on homometallic metal-metal bonded systems instead of heterometallic ones.[4, 14]

Consider, as a hypothetical example, a heterobimetallic system with a set of symmetric bridging ligands holding the core together. There are three possible scenarios for what can happen if a bridging ligand is modified to include an electron withdrawing or, as described in this work, electron donating substituent (Figure 4.1.1). In the first case, the impact of the ligand substituent on the two metals is symmetric, as would be expected if the complex were symmetric and homobimetallic. Several explicit studies of linear free energy relationships on metal-metal bonded homobimetallic complexes of this type have been

examined by Ren and coworkers.[20] For heterobimetallic complexes, a second possibility arises in which a ligand substituent effect is distributed unequally among the two metals, with the distribution being mainly based on the differing electronegativities of the metals themselves. Examples of this case appear mainly in theoretical works,[21] as most of the studies on substituent effects in heterobimetallic systems use asymmetric ligands that make assessing the impact on both metals difficult.[22-25] It is also possible that a ligand substituent effect could be distributed among two metals in such a way that is counter to what is expected from the electronegativities of the metals. It is this unusual third case that we describe in this work.

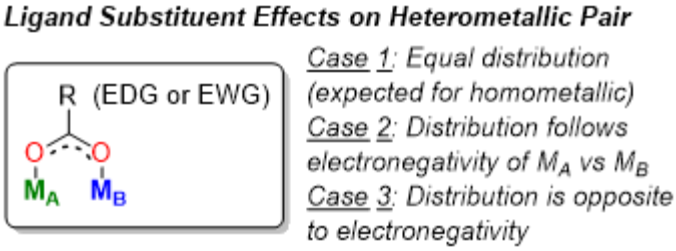

Figure 4.1.1: Possible outcomes for ligand substituent effects on an idealized heterometallic pair.

To interrogate the ligand substituent effects in a systematic series of well-defined heterometallic compounds, we examine here a class of heterotrimetallic complexes that we have found to be highly tuneable and robust to electronic modification: Heterotrimetallic metal atom chain complexes (HEMACs) with a general formula $Mo_2M'(dpa)_4Cl_2$, where M' is varied systematically across the first row transition series (Cr, Mn, Fe, Co, or Ni), and dpa is the anion of the 2,2'-dipyridylamine ligand (Figure 4.1.2).

HEMACs of this type feature a 3-center-3-electron (3*c*/3*e*) sigma bonding manifold that allows for communication and electron delocalization through the metal atom core.[26-27] Recently, we have found that the polarity of the Mo–M' bonds in these compounds is opposite of that expected from the metal atoms' electronegativities.[27] This happens because the strong Mo≡Mo quadruple bond gives rise to a low energy Mo_2 bonding combination of σ-symmetry orbitals that effectively acts as an electron donor to M'. By adding electron donating substituents to the dpa ligand and then varying the identity of the metal atom, we can determine to what extent the umpolung of the metal-metal bond polarity influences how the substituent effect is distributed on the heterometallic core.

For this investigation, we utilize the modified 4,4'-diethyl-2,2'-dipyridylamine (dedpa) ligand, which adds electron donating ethyl substituents to the dpa ligand (Figure 4.1.2). This ligand has been used previously in the synthesis of homometallic EMAC (extended metal atom chain) complexes with Cr_3, Co_3, and Ni_3 cores and has been shown to increase their solubility in nonpolar solvents and make them more electron-rich relative to dpa compounds.[28-29] We anticipated that the solubility and electron donating features would be useful for HEMACs as well. For example, the rigorous insolubility of the $Mo_2(dpa)_4$ metalloligand has prompted us to use demanding reaction conditions for HEMAC synthesis: reaction with $M'Cl_2$ in molten naphthalene as solvent. Our hope is that a more soluble metalloligand will allow us to find lower temperature synthetic routes. To probe the electron donating effects on the individual metals, we are able to use electrochemical measurements and magnetic measurements as probes of the relative HOMO energies of the HEMACs and ligand field splitting of M'.

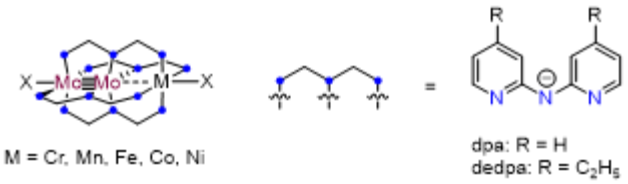

Figure 4.1.2**:** Diagram of Mo≡Mo–M compounds and structure of the dpa and dedpa ligands.

In this work we present a modernized synthesis method for the Hdedpa ligand using Buckwald-Hartwig cross coupling techniques[30-31] that has allowed us to synthesize the novel metalloligand $Mo_2(dedpa)_4$ (**1**). Metalloligand **1**, as expected, is vastly more soluble in common organic solvents than $Mo_2(dpa)_4$ (**7**), as well as being more electron rich. We have used **1** to synthesize a novel series of $Mo_2M'(dedpa)_4Cl_2$ HEMAC complexes with M' = Cr (**2**), Mn (**3**), Fe (**4**), Co (**5**), and Ni (**6**) using a solution state synthesis method with 1,4-dioxane as a solvent that we demonstrate works well for both the dpa and dedpa HEMACs. Finally, we use computational methods to explore how the ethyl substituents on dedpa impact ligand "shuffling" (Scheme 4.1.1.) of **1** and **7** (a process that appears to be facile for **1**, and is a necessary step to form HEMAC complexes from either metalloligand).

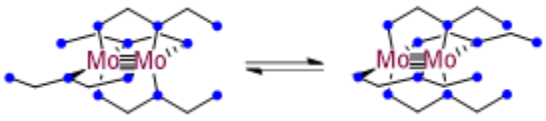

Scheme 4.1.1.: Isomerism of the ligands of **1** and **7** from the crystallographically characterized trans-(2,2) geometry to the (4,0) geometry found in HEMACs.

Results and Discussion

Section 1: Synthesis

The synthesis of the 4,4'-diethyl-2,2'-dipyridylamine (Hdedpa) ligand was achieved here through a modified Buchwald-Hartwig reaction (Scheme 4.2.1).[31] This method is higher yielding (60% vs 25% reported) than previously reported syntheses[29] and compatible with column-free workup. Deprotonation of Hdedpa with potassium bis(trimethylsilyl)amide yields the salt (Kdedpa), which was combined without further purification with $Mo_2(OAc)_4$ in THF to produce $Mo_2(dedpa)_4$ (**1**) in excellent yield (>85%).

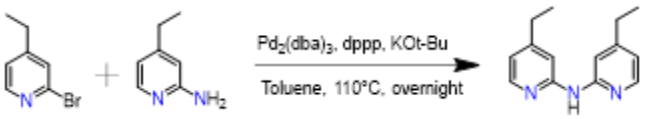

Scheme 4.2.1: Synthesis of the Hdedpa ligand used in this work. $Pd_2(dba)_3$ refers to tris(dibenzylideneacetone)dipalladium(0), and dppp refers to 1,3-bis(diphenylphosphino)propane.

Examination of **1** by NMR spectroscopy at room temperature and –20°C in CD_2Cl_2 reveals a complex, temperature dependent equilibrium in the solution state. Further investigation with 2D NMR methods shows multiple sets of pyridine rings that appear to interchange with each other. We observe that there are three major groups of peaks and four minor groups. Multiple conformations of the ligands around the Mo_2 core of **1** are possible (Figure 4.2.1),

leading us to believe that the speciation observed in the NMR spectra is the result of a slow equilibrium (slow relative to the NMR timescale) between ligand conformations in the solution state. A workup of this data is given in the Appendix (Figures S7-S21), though definitive assignment of the species observed in solution is not possible. While the dpa analog $Mo_2(dpa)_4$, **7**, is rigorously insoluble in most solvents, **1**, by contrast, is soluble in a wide range of solvents spanning in polarity from hexanes to MeOH.

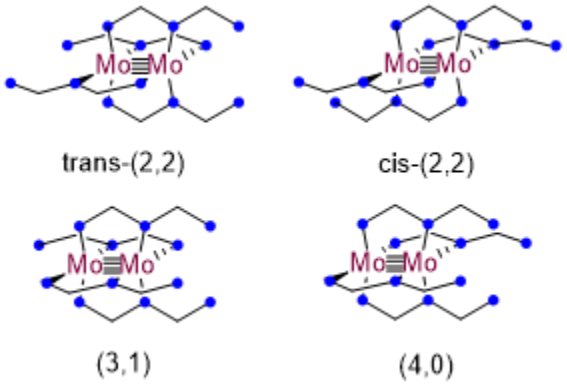

Figure 4.2.1: Possible conformations of the ligands around **1** in solution.

To produce $Mo_2M'(depa)_4Cl_2$ HEMACs with M' = Cr (**2**), Mn (**3**), Fe (**4**), Co (**5**), and Ni (**6**), two methods of synthesis were explored, as outlined in Scheme 4.2.2. First, we attempted the same method employed for the synthesis of $Mo_2M'(dpa)_4Cl_2$ compounds previously, using molten naphthalene as solvent.[32-36] Yields from these reactions ranged from fair (~30%) to excellent (~85%) depending on the metal used (Table 4.2.1).

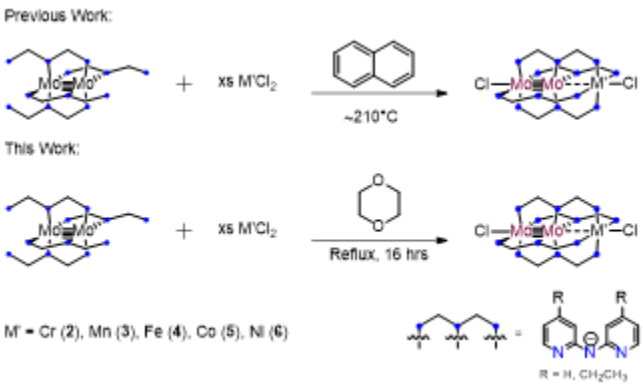

Scheme 4.2.2: General reaction schemes for producing dpa (top) and dedpa (bottom) HEMAC complexes from either naphthalene or dioxane as solvents.

The second method that we used to generate HEMAC complexes was prompted by the increased solubility of **1** as compared to **7**. First, we investigated the solution state method used to synthesize HEMACs with formula $Cr_2M'dpa_4Cl_2$: using THF as a solvent.[34, 36-37] This method failed to produce the desired product, so a higher boiling solvent was chosen: 1,4-dioxane. This ether proved to facilitate solution state synthesis for HEMACs using both the dpa and dedpa ligands. Yields for **2-6** and the dpa HEMACs are given in Table 4.2.1. For the dpa HEMACs, yields in 1,4-dioxane for M' = Cr, Mn, and Co are comparable to the previously reported syntheses, while the yields for M' = Fe and Ni are improved. The results are similar for the dedpa HEMACs. Yields for **5** and **6** are improved using 1,4-dioxane while the yield for **3** is comparable. Yields for **2** and **4** are significantly lower. The $CrCl_2$ salt used in the synthesis of **2** is not very soluble in 1,4-dioxane, likely accounting for its low yield in the solution state synthesis. For **4**, the yield can be improved from 50% to 87% by adding 10 eq of LiCl. We have not yet tested this additive in other HEMAC syntheses to determine if this effect is particular to **4** or globally applicable.

Despite the varying yields, synthesis in the solution state has a number of advantages when compared to using naphthalene as a solvent. For the dedpa HEMACs, the primary benefit is the ability to recover unreacted **1** from the reaction mixture by extraction with hexanes. We have also found workup using method 2 to be faster than method 1, though the reaction times are longer.

Table 4.2.1: Yields for HEMAC complexes from naphthalene or dioxane synthesis.

Complex	Naphthalene Yield %	Dioxane Yield %
$Mo_2Cr(dpa)_4Cl_2$	45	28
$Mo_2Mn(dpa)_4Cl_2$	32	25
$Mo_2Fe(dpa)_4Cl_2$	43	74
$Mo_2Co(dpa)_4Cl_2$	67	63
$Mo_2Ni(dpa)_4Cl_2$	39	93
$Mo_2Cr(dedpa)_4Cl_2$ (**2**)	60	17
$Mo_2Mn(dedpa)_4Cl_2$ (**3**)	46	45
$Mo_2Fe(dedpa)_4Cl_2$ (**4**)	85	50[a]
$Mo_2Co(dedpa)_4Cl_2$ (**5**)	30	65
$Mo_2Ni(dedpa)_4Cl_2$ (**6**)	56	75

[a]The yield improves to 87% when 10 eq LiCl is included in the reaction mixture.

Section 3: X-Ray Crystallography

Compounds **1-6** have been structurally characterized, and a full description of each structure can be found in the SI. Compound **1**, (Figure 4 left) was modelled in the $I4_1/a$ space group and adopts the tetragonal paddlewheel geometry expected for quadruply-bonded Mo_2^{4+} compounds. The molecule lies on the site of a crystallographic inversion center, which is located at the midpoint of the Mo–Mo vector; thus, half of the molecule is symmetry independent. Compound **1** was found to have a Mo≡Mo bond length of 2.09 Å, typical of a Mo≡Mo quadruple bond.[5] The Mo≡Mo bond length of **1** is shorter than that of **7** by 0.03 Å. Compound **1** also has a slightly smaller N–Mo–Mo–N torsion angle than **7** (~2° vs ~4°), indicating a somewhat stronger δ bonding interaction between the Mo atoms in **1**.

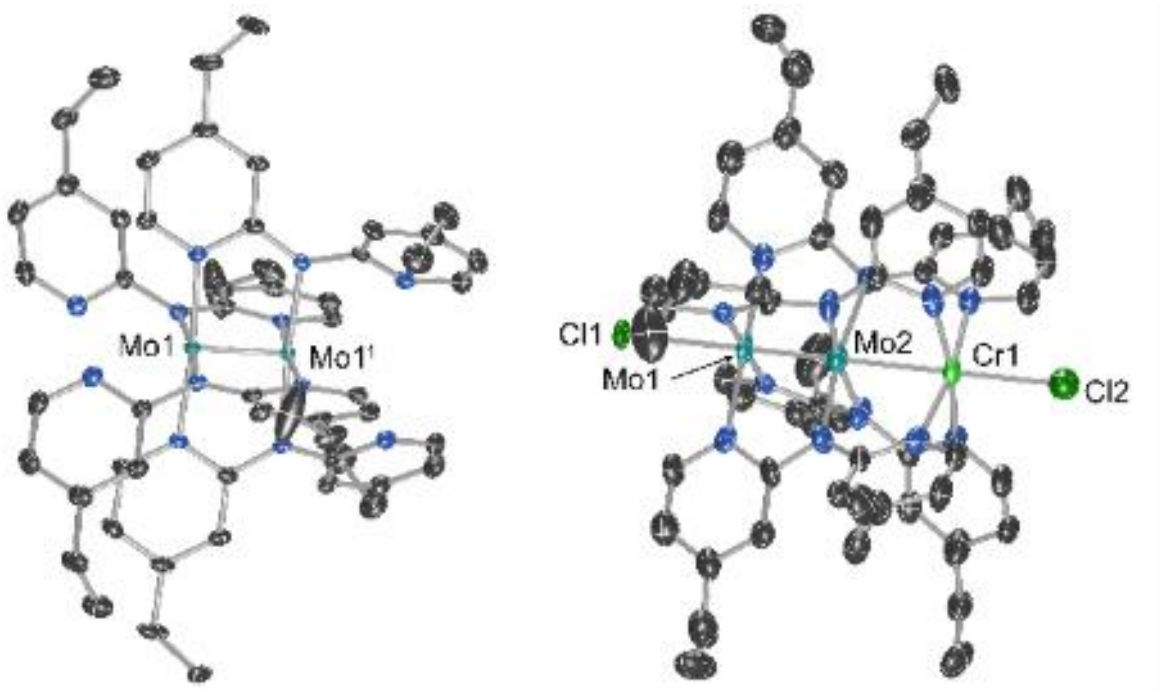

Figure 4.3.1: Left: molecular structure of **1**. Right: Molecular structure of **2**. Ellipsoids are drawn at 50% probability and hydrogen atoms are omitted for clarity. Where disorder is present, only the major component is shown.

The structure for compound **2** is shown in Figure 4.3.1 (right), and the structures of **3**-**6** are qualitatively similar (Figures S33-40 in the Appendix). Compounds **2**, **4**, **5**, and **6** are isomorphous in the *P*4*nc* space group whereas **3** adopts the cubic space group *P*432. Aside from **3**, the compounds crystallize without solvent; the crystal packing is instead dominated by interactions between the peripheral ethyl substituents fitting together like puzzle pieces (Figure S53 in the Appendix).

For the structures in the *P*4*nc* space group, the metal atoms in the molecule are colinear with a crystallographic 4-fold axis. The structures are complicated by two types of positional disorder. First, there is disorder of the metal atom positions such that molecules

pointing in opposite directions both occupy the same crystallographic site. The metal atom positions show a ~55:45 split over the two sites in all structures. The second type of positional disorder is caused by the dedpa ligands wrapping around the metal atom chains in a helical fashion, making the trimetallic compounds chiral. Both enantiomers of the helical structures co-crystallize at the same site, leading to positional disorder in the ligand manifold. For the enantiomers of the helix, the Λ isomer is favored with occupancy of ~80%. These instances of positional disorder result in four distinct crystallographic orientations of the molecule can be more simply described as pairs of enantiomers that face in opposite directions. The four disordered orientations are illustrated in Figure 5. Bond lengths for the major disorder components are provided in Table 2, with a full description of each compound found in the SI.

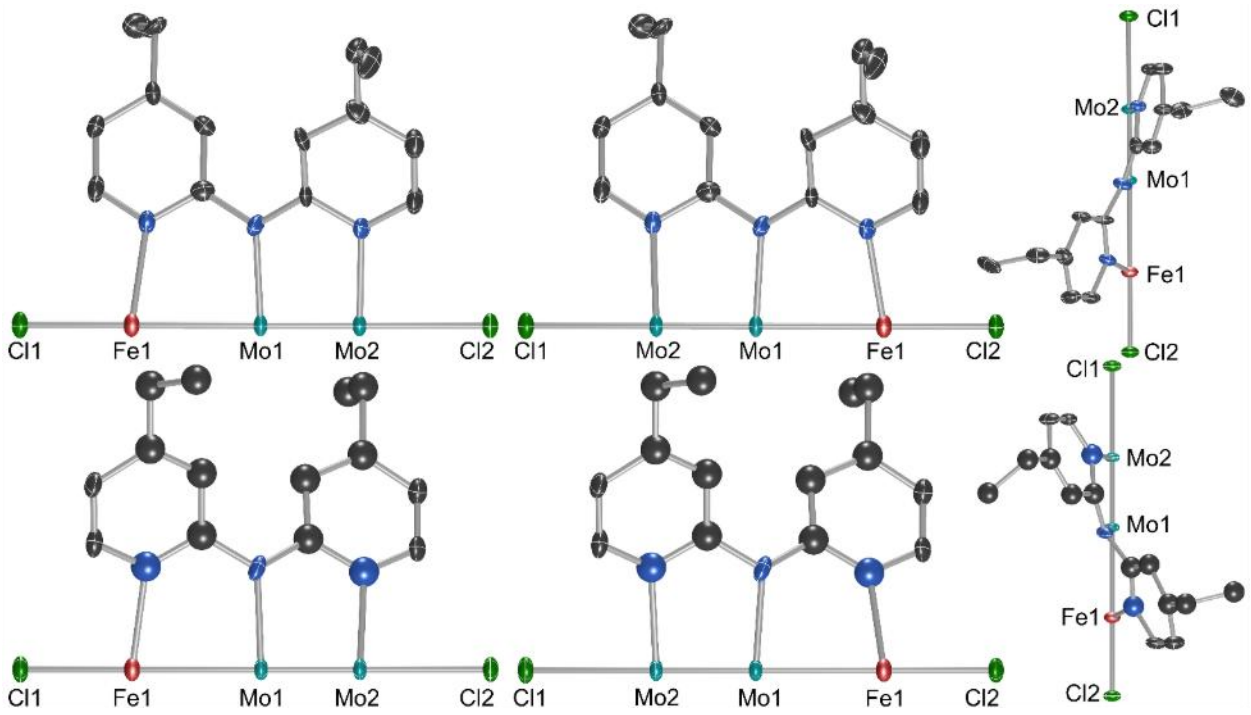

Figure 4.3.2: Positional disorder within the crystal structure of **4**, also present in **2**, **5**, and **6**, modeled as four distinct molecular orientations of two enantiomers. The top row shows the Λ enantiomer with both metal orientations (major left, minor right). The bottom row shows the Δ enantiomer with both orientations. The right most images show a side-on view of the asymmetric unit to illustrate the different helical twist of the two enantiomers. Only one ligand out of 4 is shown around the metal axis for clarity. Hydrogen atoms are omitted for clarity. Ellipsoids are shown at 50% probability.

Due to the high crystallographic symmetry for **3**, the central Mo atom of the structure is fixed at a site of 422 symmetry and does not refine to an atomic position off of this site. However, it is clear from comparing metal-metal bond distances in the structures of **2**, **4**, **5**, and **6**, that this Mo atom in **3** *should* be at a position slightly off of the 422 site, further toward the terminal Mo atom along the 4-fold axis. Since it is not possible to refine the Mo

atom at a more appropriate site, bond lengths involving this Mo atom are inconsistent with those seen in the other crystal structures and are thus deemed not to be chemically reasonable. These distances, marked with * in Table 2, are excluded from further analysis and are replaced, where necessary, with the bond lengths from the computationally optimized structure.

Table 4.3.1: Crystallographic and computational bond lengths of interest for the major components of **2-6**.

M’	Mo-Mo (Å)	Mo-M' (Å)	M’-N (Å)	Mo_{in}-N (Å)	Mo_{out}-N (Å)	Mo-Cl (Å)	M'-Cl (Å)
2	2.11(2)	2.77(2)	2.181(8)	2.123(5)	2.165(7)	2.736(17)	2.48(2)
2-DFT	2.108	2.653	2.110	2.139	2.230	2.721	2.501
3	2.1954(19)*	2.765(4)*	2.267(4)	2.133(5)	2.211(3)	2.808(3)	2.238(4)
3-DFT	2.109	2.773	2.236	2.150	2.232	2.709	2.366
4	2.100(9)	2.721(14)	2.206(8)	2.131(4)	2.171(3)	2.773(8)	2.369(13)
4-DFT	2.114	2.689	2.169	2.133	2.213	2.620	2.318
5	2.122(9)	2.620(16)	2.190(8)	2.121(5)	2.183(7)	2.688(8)	2.470(13)
5-DFT	2.115	2.574	2.137	2.133	2.213	2.622	2.370
6	2.118(9)	2.589(18)	2.151(9)	2.119(5)	2.174(8)	2.645(8)	2.435(15)
6-DFT	2.112	2.511	2.096	2.129	2.214	2.601	2.408

In Table 4.3.1, we see a decrease in Mo–M' bond lengths of ~ 0.2 Å going from **2** to **6**. A similar trend was observed with the analogous dpa compounds (Table S2), which is attributed to the decrease in M' radius and increase in Mo–M' covalency with increasing electronegativity of M'.[27] In addition, the M'–N bond lengths give insight into the spin state of M'. For **2-6**, the M'–N bond lengths > 2.15 Å indicate that each compound contains a high spin M'^{2+} ion. These results are consistent with the spin states found in the $Mo_2M'(dpa)_4Cl_2$ series, despite the fact that dedpa is more electron rich than dpa and is, presumably, a stronger field ligand.[27, 34, 38] In fact, the M'–N bond lengths are uniformly *longer* in **2-6** than in the analogous dpa compounds, suggesting that the dedpa ligand is actually a *poorer* σ-donor to M' in this series. A possible reason for this seeming paradox is that dedpa forms shorter bonds to the more electron poor outer Mo atom than dpa does, by ~0.07 – 0.1 Å. Since the inner Mo–N distances are very similar for both series of compounds, there is a lever effect whereby a shorter outer Mo–N distance requires a longer M'–N distance. Overall, this leads to a weaker ligand field around the less tightly bound M' atom and a stronger field around the more tightly bound outer Mo atom. Thus, the electron donating effect of the dedpa ligand is not distributed equally among all metal atoms in the HEMACs.

Section 4: Magnetic Properties

The high spin states of M' in **2-6** were confirmed through SQUID magnetometry. Magnetic susceptibility data in the form of χ·T vs T plots for each compound are shown in Figure 6. For each compound except **5** the χ·T vs T curve is characterized by a sharp rise starting at very low temperatures, then a linear increase with increasing temperature. The susceptibility for **5** shows a gradual incline at low temperatures that levels off at higher temperatures. Each compound reaches the expected spin only values for a high-spin M'^{2+} ion in the high temperature limit, as indicated in Figure 4.4.1, confirming that the M'^{2+} ions in **2-6** are all high spin.

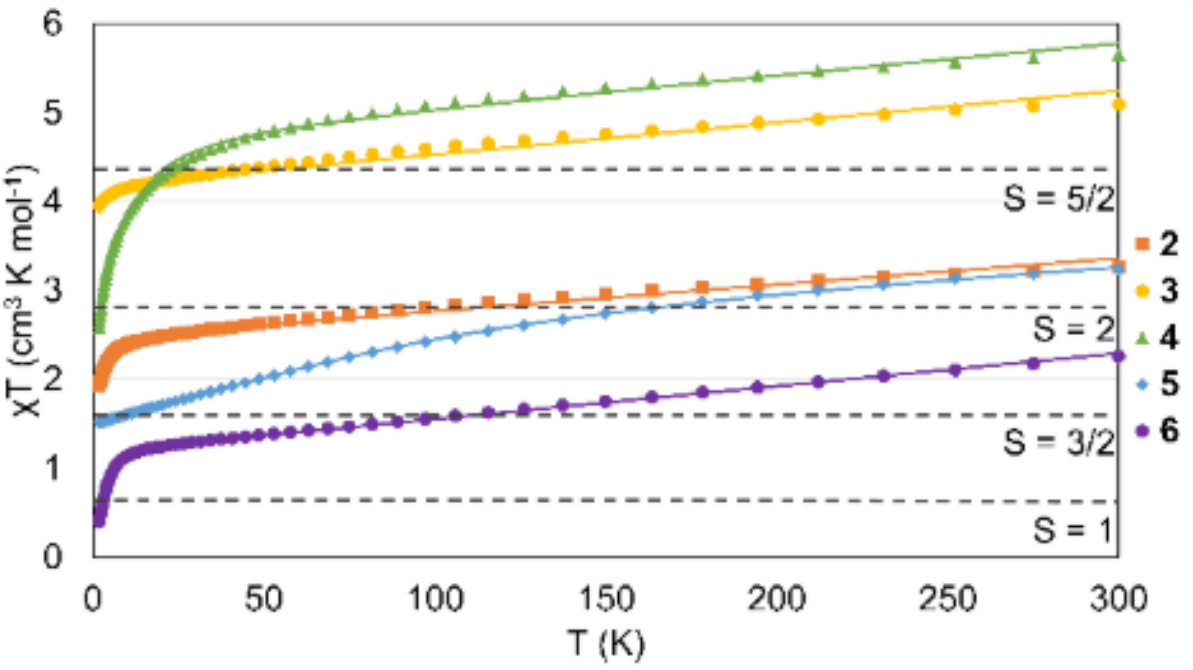

Figure 4.4.1: SQUID Magnetometry data for **2**-**6**. Data are shown as markers with the fits indicated with solid lines. The spin-only expected values are given with dotted lines. For each compound, the saturation value approximates the spin only expectation value.

The magnetic susceptibility and reduced magnetization data for compounds **2-6** were modeled using spin systems with S = 2, 5/2, 2, 3/2, and 1, respectively, using the parameters given in Table 4.4.1. These models consider each compound to contain an isolated M' center coordinated to a diamagnetic, quadruply-bonded, Mo_2 unit. The sharper rise at low temperatures seen in **2-6** indicates magnetic anisotropy that can be attributed to either an effect of zero-field splitting (ZFS), an effect of intermolecular coupling (zJ), or a combination of the two. Compounds **2** and **3** are well modelled only considering axial ZFS, but **4-6** required the additional inclusion of an intermolecular term. The modelled ZFS terms for **2** and **4** have values of $D < 0$ cm^{-1}, while those for **3**, **5**, and **6** have $D > 0$ cm^{-1}, with the sign of D being determined via modeling of the reduced magnetization curves. The intermolecular terms included for **4-6** are negative in all cases, indicating antiferromagnetic coupling between molecules in the lattice. The gentle, linear rise in the higher temperature regime for all compounds was modelled as temperature independent paramagnetism (TIP), which is large, but within a narrow range of 2,032 to 3,697 × 10^{-6} cm^3 mol^{-1}. It is possible that the relatively low-lying triplet δ-δ* state of the Mo_2 unit contributes to the large TIP.

Table 4.4.1: Fitting parameters for SQUID magnetometry data of **2-6;** EPR simulation parameters for **3** and **5** are given in brackets.

M'	$g_{\perp}$ [EPR]	$g_{\parallel}$ [EPR]	D (cm^{-1}) [EPR]	TIP	zJ
2	1.826(3)	1.729(3)	-1.526(7)	0.00331(3)	N/A
3	1.953(2) [1.95, 2.1]	1.953(2) [2]	0.5-0.75[a] [0.3]	0.00358(6)	N/A
4	2.607(4)	2.313(5)	-6.36(4)	0.00354(6)	-0.0063(9)
5	2.2362(9) [2.37, 2.89]	2.858(5) [2.3]	79.5(2) [79.5]	0.002032(9)	-0.0024(3)
6	2.2196(9)	2.092(2)	7.864(5)	0.003697(5)	-0.015(1)

[a] Value is given as a range because the reduced magnetization and susceptibility data were modelled independently.

Compounds **2** and **4** have easy axis magnetic anisotropy (D < 0), presumably oriented along the Mo-Mo-M' axis. The small value of D for **3** is consistent with the d^5 configuration for Mn(II). The resulting g-factors of these models are consistent with the respective valence electron count of each M' metal. For **2** the g_{ave} < 2.00 is consistent with the d^4 electron configuration of Cr(II). The average g for **3** is also less than 2; while the d^5 Mn(II) ion is expected to have isotropic g = 2.00, the lower value for **3** likely reflects some electron delocalization to the Mo(II) ions. The g_{ave} of **4-6** are greater than 2.00, consistent with M' systems with greater than five valence electrons.

Compounds **3** and **5** were further investigated using X-band EPR spectroscopy in frozen DCM solution at 5 and 10 K, respectively (Figure 7, A and C). Spectra for both compounds show one major, nearly axial feature (E/D = 0.03 (**3**) and 0.07 (**5**)) with intrinsic g_{avg} = 2.01 (**3**) and 2.52 (**5**) consistent with high-spin Mn^{2+} and Co^{2+} respectively. Parameters used in the simulation of both spectra are given in brackets in Table 3. The EPR spectrum for **3** is complex, with features at effective g values of $g_{\perp}g_{\perp}$~ 6 and $g_{\parallel}g_{\parallel}$~ 2 with several other observable features suggesting S = 5/2 with a small D value (0.3 cm^{-1}) that is similar to the energy of the microwave quantum (9.4 GHz = 0.31 cm^{-1}). $Mo_2Mn(dpa)_4Cl_2$ was studied by high-field EPR spectroscopy and found to have an essentially identical D value to **3.**[36] Further analysis of **3** using simulated Zeeman splitting diagrams with applied fields in the x, y, and z directions helps to confirm the assignment of the D value of **3** as positive and very close to the microwave quantum with a slight rhombicity contributing to the number of visible transitions including inter-doublet transitions (Figure 4.4.1B).

The spectrum of **5** is more clearly in the S = 3/2, $D > h\nu$ regime with effective g values of $g_{\perp}g_{\perp}$~ 4 and $g_{\parallel}g_{\parallel}$~ 2. This spectrum was modeled using a value of D fixed to that determined from the magnetic susceptibility measurement and E/D of 0.07. The features are broadened, likely due to unresolved hyperfine coupling to the I = 7/2 ^{59}Co nucleus. $Mo_2Co(dpa)_4Br_2$ has similar EPR features to **5** in its high-spin form: $D > h\nu$ and E/D = 0.1[39].

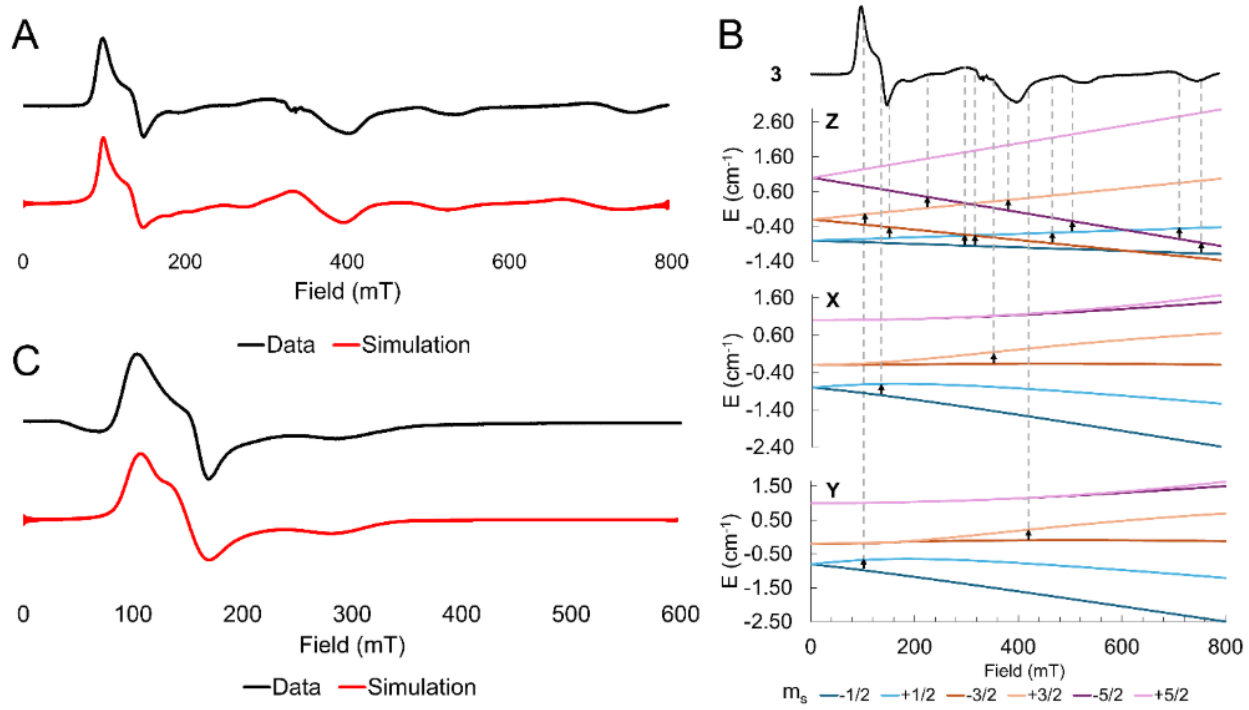

Figure 4.4.1.: **A***: An EPR spectrum of* ***3*** *taken in frozen DCM solution at 5 K. The spectrum is simulated in red with g values of [1.95, 2.1, 2], an E/D of 0.03, some unresolved hyperfine from the Mn nucleus of A = [150, 50, 0] MHz, with broadening from D-strain of [1500, 100] MHz.* **B***: A Zeeman analysis of the transitions visible in the X-band EPR spectrum of* ***3****. The experimental spectrum is shown at the top, with the simulated Zeeman diagrams for an applied field along the z, x, and y directions from top to bottom. The* m_S *states are given in pairs of complimentary colors, with* m_S *± ½ at the bottom in blue,* m_S *± 3/2 in the middle in orange, and* m_S *± 5/2 in pink at the top.* **C***: An EPR spectrum of* ***5*** *taken in frozen DCM solution at 10 K. The spectrum is simulated in red with g-values of [2.37, 2.89, 2.30]. The D-value used here is fixed to that from the fitted SQUID magnetometry data, at 79.5* cm^{-1}*. The E/D is 0.07. A = [80, 80, 0] MHz, H strain = [500, 1000, 1500] MHz, D strain = [0, 200000] MHz.*

Section 5: Mössbauer Spectrum of 4

The Mössbauer spectrum of **4** displays one quadrupole doublet (Figure 4.5.1) with an isomer shift (δ) of 1.04 mm s^{-1} and a quadrupole splitting (ΔE_Q) of 0.78 mm s^{-1}. The ΔE_Q and δ for this feature are consistent with a single pseudo-octahedral high-spin Fe^{2+} site. Given the metal-atom disorder in the crystal structure of **4**, two Fe sites would be expected to be visible in the Mössbauer spectrum, however, as only one quadrupole doublet is observed, it can be assumed that the two sites have very similar Mössbauer parameters. Attempts to model the doublet as a pair of overlapping doublets were unproductive. The similarity of the Mössbauer parameters for the different Fe sites in **4** is in contrast with the Mössbauer data for $Cr_2Fe(dpa)_4Cl_2$, for which we found two distinct quadrupole doublets corresponding to two crystallographically independent Fe sites, with identical δ values (1.01 mm s^{-1}) and very different ΔE_Q values (1.63 vs 2.39 mm s^{-1}).[36-37]

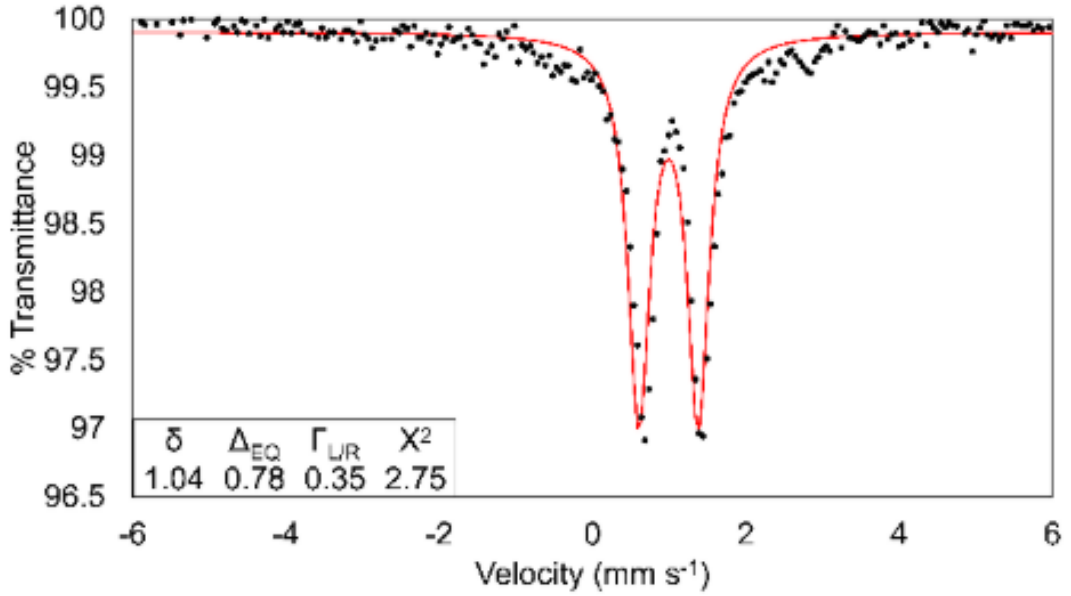

Figure 4.5.1: A Mössbauer spectrum of **4** taken at 77 K that shows one site of high spin Fe^{2+} with the fit shown in red. The doublet has a δ of 1.04 mm s^{-1} and ΔE_Q of 0.78 mm s^{-1}.

Mössbauer parameters for **4** and related compounds are given in Table 4.5.1. In comparison to the other known CrCrFe and MoMoFe compounds, **4** has a smaller quadrupole splitting by up to 2.2 mm s^{-1}. This smaller quadrupole splitting indicates a smaller electric field gradient at the Fe nucleus for **4**, which is consistent with the structural analysis above indicating longer Fe–N bonds and a weaker ligand field for the Fe atom in **4** as compared to other $M_2Fe(dpa)_4X_2$ compounds. The isomer shift of **4** is very similar to other compounds in this family, and lies in the expected range for a high spin Fe^{2+} complex.

Mössbauer parameters were calculated using DFT methods for a computationally optimized structure of **4** as well as the two crystallographically distinct sites in frozen geometry single point calculations. The experimental values of δ and ΔE_Q were not well reproduced using these computational methods, which is likely attributable to the partial sharing of valence electrons with the Mo atoms. Nevertheless, the predicted differences in δ and ΔE_Q between the two crystallographic sites are sufficiently small as to be functionally indistinguishable ($\Delta\delta$, $\Delta\Delta E_Q \sim 0.06$ mm s^{-1}), validating the theory that the two sites are too similar to appear separately in the experimental spectrum.

Table 4.5.1.: Collected Mössbauer parameters for **4** and related compounds.

Compound	δ, mm s^{-1}	ΔE_Q, mm s^{-1}
$Cr_2Fe(dpa)_4Cl_2$ (site 1)[36]	1.01	1.63
$Cr_2Fe(dpa)_4Cl_2$ (site 2)[36]	1.01	2.39
$Mo_2Fe(dpa)_4Cl_2$[40]	1.02	2.02
$Mo_2Fe(dpa)_4(OTf)_2$[27]	1.05	2.48
4	1.04	0.78
4 (site 1, DFT)	0.88	2.96
4 (site 2, DFT)	0.88	2.9
4 (DFT optimized structure)	0.82	2.92

Section 6: Electrochemical Properties

The cyclic voltammograms (CVs) of **1-6** taken in CH_2Cl_2 solution are shown in Figure 4.6.1. Each compound displays one major quasi-reversible feature; that for **1** at –966 mV vs Fc/Fc^+ may be straightforwardly assigned to the $Mo_2^{4+/5+}$ redox couple of the quadruple-bonded Mo_2 unit. This redox couple has a very low voltage as compared to other Mo_2

complexes supported by N,N'-donor ligands. For example, Mo_2(formamidine)$_4$ complexes have $Mo_2^{4+/5+}$ couples ranging from –381 mV to +170 mV vs Fc/Fc^+,[41] and the first redox event for Mo_2(2-anilino-pyridinate)$_4$ appears at 0.00 V vs Ag/AgCl (~ –400 mV vs Fc/Fc^+).[42] The parent dpa compound, **7**, is insoluble and thus could not be interrogated by cyclic voltammetry. However, salts of the $\mathbf{7}^+$ cation are isolable and have been studied.[35] The $Mo_2^{4+/5+}$ couple for **7** is reported at –832 mV vs Fc/Fc^+. Compound **1** is thus easier to oxidize than its dpa congener by ~ 130 mV, which is a significant change indicating that **1** is more electron rich than **7**. This change mirrors the lowering of the $M_3^{6+/7+}$ couples by ~ 130 mV in M_3(dedpa)$_4Cl_2$ vs M_3(dpa)$_4Cl_2$ compounds with M = Cr, Co, and Ni.[28-29]

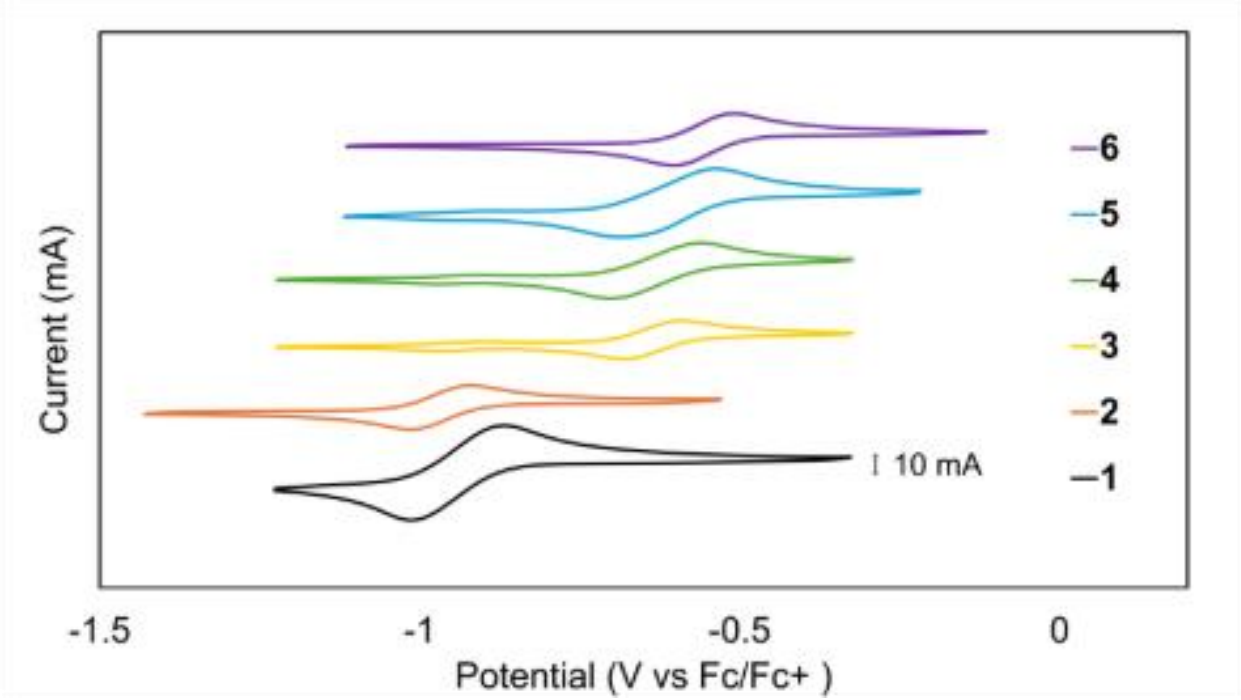

Figure 4.6.1.: Cyclic voltammetry data of **1-6** taken in CH_2Cl_2 vs Fc/Fc+ with a scan rate of 100 mV/s. The scans of **3-5** show a second peak at approximately the same V as **1**, indicating a slow equilibrium relative to scan rate in solution of **3-6** with **1**. The scans of **3-6** show a trend in which the potential of the major signal (theorized to be the $Mo_2^{4+/5+}$ couple) shifts more positive with an increasingly electronegative heterometal.

We report here, for the first time, electrochemical measurements on a complete series of Mo_2M' HEMAC compounds with M' = Cr – Ni. Compound **2** has a low $Mo_2M'^{6+/7+}$ couple, –969 mV vs Fc/Fc^+, whereas the corresponding redox events for **3** – **6** are more invariant, within the relatively small range of –635 to –556 mV vs Fc/Fc^+. These data suggest that there is a fundamental difference in the nature of the redox process for **2** vs **3** – **6**. We may consider whether the redox processes in these compounds may be attributed to the $Mo_2^{4+/5+}$ couple or the $M'^{2+/3+}$ couple. One may expect from first principles that the addition of a positively

charged Lewis acid to a redox active Mo_2 unit would cause the Mo_2 unit to be more difficult to oxidize. Thus, oxidation of the Mo_2 unit in **3** – **6** is less accessible than in **1** by at least 330 mV. This assignment of the quadruply-bonded Mo_2 group as the redox active unit in **3** – **6** also agrees with our recent report of the $[Mo_2Ni(dpa)_4Cl_2]^+$ cationic species, which clearly displayed evidence of an oxidized Mo_2^{5+} unit within the compound.[33] But what of the Mo_2Cr compound **2**? It is oxidized at only 30 mV above the parent compound **1**. It's most likely that this redox event corresponds to the oxidation of Cr^{2+} to Cr^{3+}. Support for this conclusion comes from reports of the oxidation of $Cr_3(dpa)_4X_2$ compounds, which yield unsymmetric species in which a Cr^{3+} ion is appended to an intact CrCr quadruply bonded group.[43-44]

In addition to the $Mo_2^{4+/5+}$ signals described above, **3** – **5** display a second, smaller peak that has an $E_{1/2}$ matching that of **1**. We suspect that these signals indicate an equilibrium in solution between the trimetallic HEMAC complex and the bimetallic metalloligand precursor, Eq. 4.6.1. The peak corresponding to **1** does not grow with successive scans, further supporting that the extra peak is due to an equilibrium between two species and is not due to degradation of the HEMAC upon oxidation. The peak magnitude is also not dependent on the scan rate of the measurement down to 50 mV/s, indicating that the equilibrium is slow relative to the scan rate.

$$Mo_2M'(dedpa)_4Cl_2 \rightleftharpoons Mo_2(dedpa)_4 + M'Cl_2 \qquad \text{Eq. 4.6.1: M' = Mn, Fe, Co}$$

Although the $Mo_2^{4+/5+}$ redox couples for **3** – **6** lie within a narrow range, a clear trend emerges wherein the potential becomes more positive with increasing electronegativity of the heterometal (Table 4.6.1). Electronic structure studies on the $Mo_2(dpa)_4(OTf)_2$ series

indicated that the heterometallic bonds become more covalent across the series from Mn to Ni.[27] Thus, we can conclude that the increasing covalency of the Mo_2-M' bond is modifying the oxidation potential of the Mo_2 core to make it more difficult to oxidize. From previously reported data on similar compounds with a Cr_2, Mo_2, and W_2 core (Table **4.6.1**) we can draw more conclusions about the redox properties of **1-6**. We note that redox potentials for all $[M_2(L)_4]^{0/+}$ metalloligands are known as well as for $[M_2Fe(L)_4Cl_2]^{0/+}$ compounds. These potentials are depicted in Figure 4.6.2, where we see that the Fe complexes lie uniformly higher in potential than the metalloligands. In the Cr_2Fe case, oxidation is attributed to the $Fe^{2+/3+}$ couple,[37] but for the other compounds, the M_2Fe oxidation is centered at the multiply bonded $M_2^{4+/5+}$ core. Addition of Fe to Mo_2 species **1** or **7** causes large increases in the $Mo_2^{4+/5+}$ couple, ~340 mV, compared to ~260 mV for the W_2 case. It's therefore likely that heterometallic covalency is maximal for the Mo_2–Fe bonds. Another important takeaway from Figure 4.6.1 is that the impact of the electron donating ethyl substituents of the depa ligand is clearly seen in the redox potentials of both **1** and **4**: both complexes show a ~130 mV negative shift of their $Mo_2^{4+/5+}$ couples.

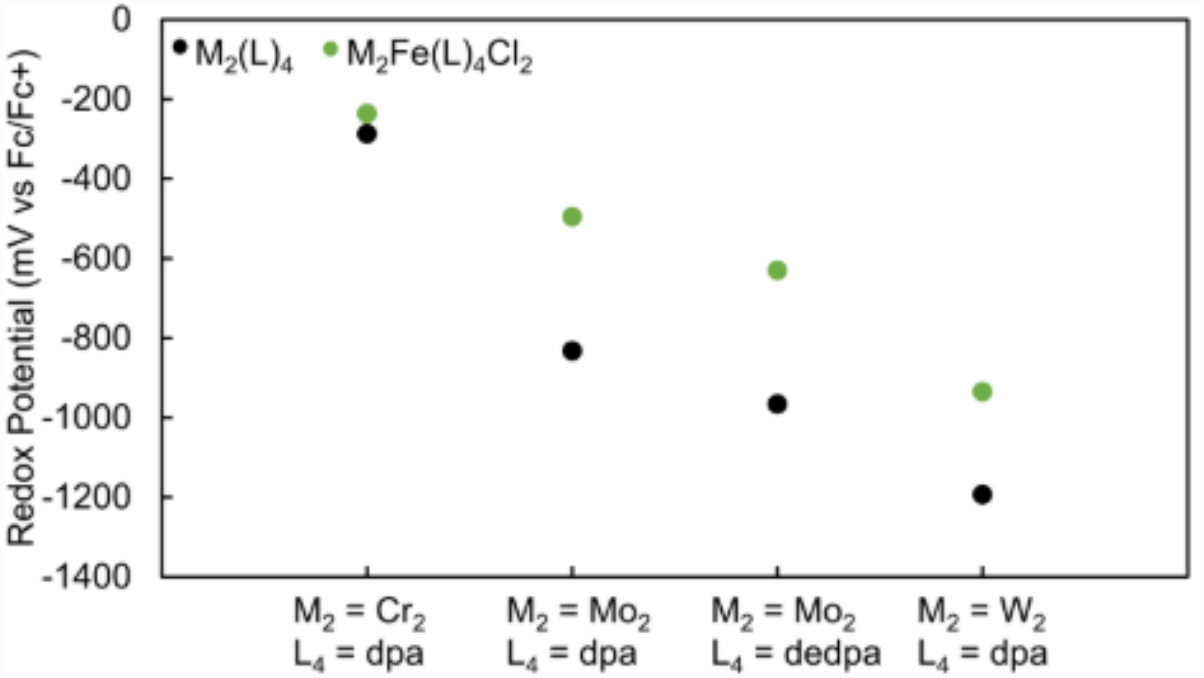

Figure 10: A comparison of redox potentials of metalloligand $M_2(L)_4$ species compared to their Fe-containing HEMAC complexes. The potentials of the HEMACs are universally higher than the metalloligands, with the difference being largest in Mo_2 containing HEMACs, indicating that the Mo_2-Fe interaction is the most covalent of the three.

Table 4.6.1: Oxidation potentials for some HEMAC compounds taken in DCM and referenced against Fc/Fc^{+}

Compound	$M_2^{4+/5+}$ $E_{1/2}$ (mV)
1	-966
2	-969
3	-635
4	-630
5	-610
6	-556
Cr_2dpa_4[37]	-287[a]
$Cr_2Fedpa_4Cl_2$[37]	-236
$Mo_2dpa_4BPh_4$[35]	-832
$Mo_2Crdpa_4Cl_2$[32]	-860
$Mo_2Fedpa_4Cl_2$[40]	-495
$Mo_2Nidpa_4Cl_2$[33]	-418
$W_2dpa_4BPh_4$[35]	-1193
$W_2Crdpa_4Cl_2$[32]	-1010
$W_2Fedpa_4Cl_2$[40]	-935

[a] this feature is irreversible.

Section 7: Electronic Structure Analysis

Density functional theory (DFT) calculations were used to analyze the structures and bonding of **2-6** further. We utilized the BP86 functional for these calculations, which has been found in our previous research efforts to be a good choice for the $Mo_2M'(dpa)_4X_2$ compounds.[27] Furthermore, bond lengths from the optimized structures are generally in good agreement with the crystallographic models, with the exception of the Mo-M' bond lengths, which have errors as high as ± 0.15 Å (Table 4.3.1 and Table S3 in the Appendix). The Mo-M' bond lengths were not improved with the use of the B3LYP or PBE functionals, so BP86 was used for models of **2-6**. As seen for the series of $Mo_2M'(dpa)_4(OTf)_2$ compounds, the Mo–M' Mayer bond orders increase from **2** to **6**. Bonding is understood in reference to the molecular orbital model in Figure 4.7.1.[27] In this diagram, Mo_2-centered electrons occupy red orbitals and M'-centered electrons occupy black orbitals. The blue orbitals, of σ symmetry, are mixed such that the three metal dz2dz2orbitals form three-center bonding, non-bonding, and antibonding orbital combinations. Since all M'^{2+} ions are high-spin, compounds **2** – **6** have electron configurations of $\sigma^2\sigma_{nb}^1$, with a 3-center, 3-electron σ bond. The change in Mo–M' Mayer bond order stems from the change in M' effective nuclear charge (*Z**) from **2** to **6**, with the Mo–M' bonds becoming more covalent from Cr to Ni.

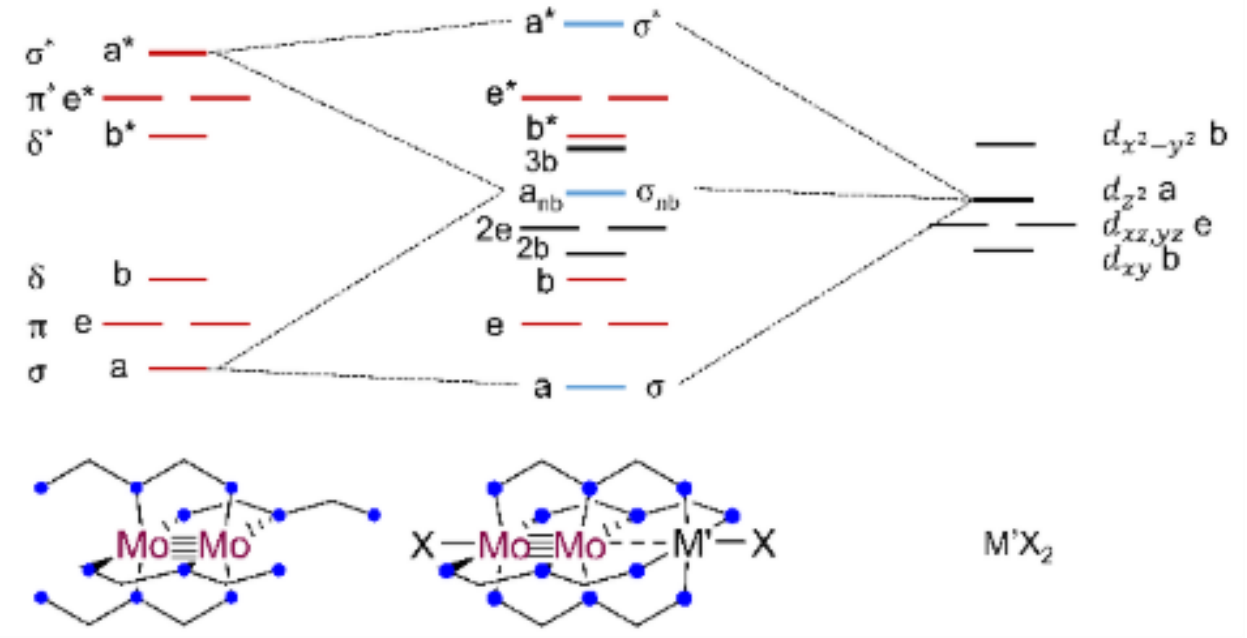

Figure 4.7.1: Idealized molecular orbital diagram for **1**, left, and its interaction with a tetragonally symmetric $M'X_2$ unit to produce an $Mo_2M'(dedpa)_4X_2$ compound (center).

Electronic spectra for **1**-**6** are best understood with reference to the molecular orbital model in Figure 4.7.1. The Mo_2 unit has its valence *d* orbitals split into bonding and antibonding orbitals of σ, π, and δ symmetry with a relatively large energy gap between the highest-occupied δ and lowest unoccupied δ^*. The valence 3*d* orbitals of the first-row metal atom generally fall between this gap, though the energies are uniformly lowered from Cr to Ni with increasing *Z**. For M' = Cr, the σ_{nb} orbital lies energetically between the Mo_2 δ and δ^* orbitals as shown in Figure 4.7.1, but the increase in *Z** from Cr to Ni causes the α M' orbitals for the later M' metals to fall below the Mo_2 δ orbital.

Electronic absorption spectra of **1-6** were taken in DCM solution (Figure 4.7.2). The spectrum for **1** features two main absorption features at 20,408 and 17,540 cm^{-1} assigned (with the aid of TD-DFT) as the Mo_2 δ→δ* transition (17,540 cm^{-1}) and a Mo_2 δ→π* transition (20,408 cm^{-1}). Compounds **2-6** have absorption features at 24,200-24,700 cm^{-1} (transition A), 20,325-20,900 cm^{-1} (transition B), 14,000-14,800 cm^{-1} (transition D), and ~12,500 cm^{-1} (transition E). An additional peak is visible in **3-6** at 17,000 cm^{-1} (**3-5**) and 18,500 cm^{-1} (**6**) (transition C). Transitions A and B are of an intensity that suggests metal to ligand charge transfer (MLCT), while transitions C-E are significantly weaker, ~ 1,000 to 2,000 L mol^{-1} cm^{-1}, suggesting that they are ligand field transitions. Based on its position, intensity, similarity to the absorption feature in **1**, and assignments in $Mo_2M'(dpa)_4Cl_2$ compounds, transition D should be assigned to the Mo_2 δ-δ* transition for each compound. Transitions C and E, however, are not assigned in the analogous $Mo_2M'dpa_4Cl_2$ complexes or in the $Mo_2M'dpa_4OTf_2$ complexes.[27, 45] We therefore have employed TD-DFT methods at the cam-B3LYP level to explore the electronic transitions further on models of **2** – **6** whose geometries were optimized as described in the DFT section above. The experimental and calculated absorption features are collected together in Table 4.7.1.

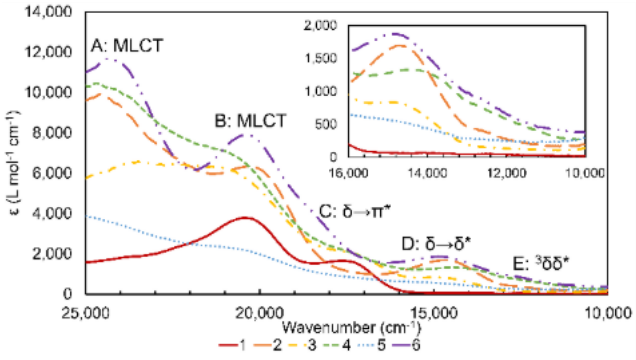

Figure 4.7.2: UV-vis spectra for **1-6** with an inset of the 10,000-14,000 cm^{-1} region. There are five distinct transitions that are present in **2-6**: two metal to ligand charge transfer bands (~24,000 and 20500 cm^{-1}), a transition assigned as δ to π* (17000-18500 cm^{-1}), a δ to δ* transition (~14,500 cm^{-1}), and a low energy transition assigned as a transition involving the Mo_2 ^{3}δδ* state (12500 cm^{-1}).

These results confirm the MLCT character of bands A and B, as well as that D results from a Mo_2-based δ-δ* transition. Interestingly, transition C is assigned to a δ-π* transition on the Mo_2 unit that has not been independently visible in other $Mo_2M'dpa_4X_2$ complexes.

Table 4.7.1: Electronic absorption transition peaks (cm^{-1}) and molar absorptivity values, ε ($L\ mol^{-1}\ cm^{-1}$)

Transition	**1**	**2**	**3**	**4**	**5**	**6**	Assignment
A	-	24631	23641	24510	24752	24272	MLCT
(ε)		(9930)	(6530)	(10300)	(3790)	(11700)	
B	20408	20325	20877	20833	20534	20325	MLCT
(ε)	(3790)	(6150)	(6180)	(6970)	(2230)	(7890)	
C	17544	-	17007	17182	-	18450	δ à π*
(ε)	(1610)		(1790)	(1880)		(4030)	
D	-	14641	14641	14025	14728	14771	δ à δ*
(ε)		(1840)	(823)	(1290)	(540)	(1870)	
E	-	12500	12500	12500	12500	12500	^{3}δδ*
(ε)		(393)	(275)	(718)	(274)	(849)	

Upon inspection, the δ-δ* transitions of **2-6** do not have the same energies, suggesting a perturbation of the Mo_2 δ-bond by the neighboring M' atom. The breakdown of TD-DFT orbital contributions for this transition indicates that the transition has Mo_2→M' charge transfer character in addition to δ-δ* character and that the degree of charge transfer

character increases as the Mo–M' bonds become more covalent from M' = Cr to Ni (Figure 4.7.3). Transition D has overwhelming (~ 80%) δ-δ* character for **2**, but the δ-δ* character decreases to only 56% in **6**, in which the transition has additional δ-σ_{nb} character (25%). Thus, as the electronegativity of M' increases and the Mo–M' bonds become more covalent, the sigma MMCT character of band D increases. The same trends can be seen in transition C, though the trends in orbital contribution are less clear.

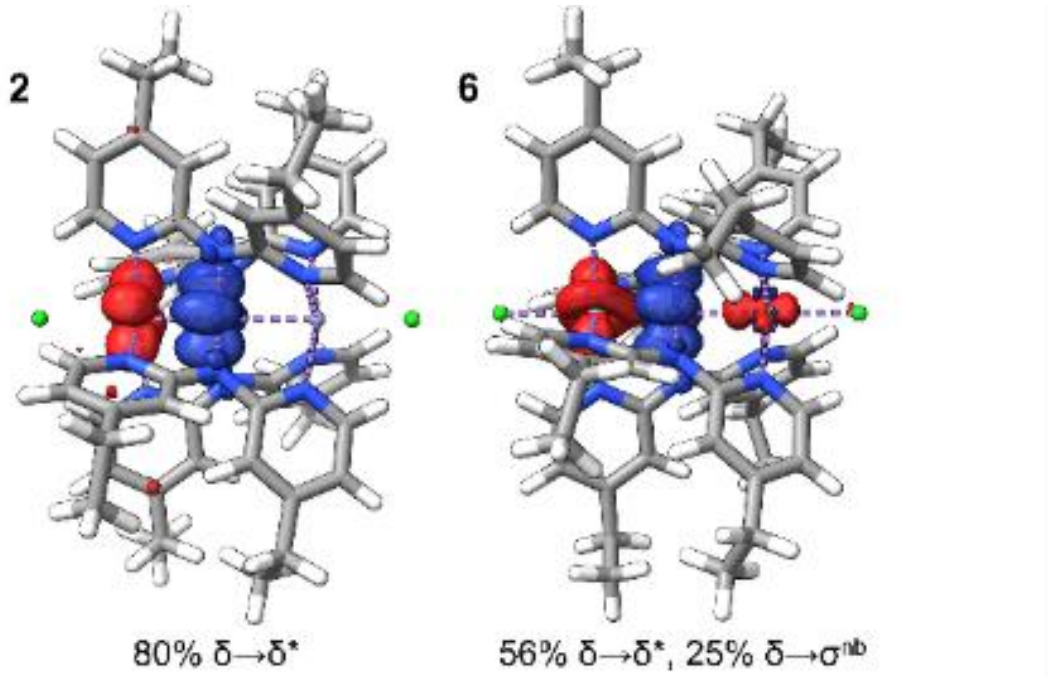

Figure 4.7.3: Electron density difference maps (EDDMs) for transition D in **2** (left) and **6** (right) where the electron density is being transferred from a δ symmetry orbital (blue) to a δ* or combined δ* and charge transfer orbital (red). The charge transfer character increases going from **2** to **6**.

Compounds **2**-**6** also display low-intensity bands at around 12,500 cm^{-1} (Band E) that may involve a formally spin-forbidden excited state of the Mo_2 unit. Because the position of

band E is independent of M', it is tempting to assign this to a Mo_2-centered transition. Specifically, a triplet Mo_2 δ-δ* excited state may be antiferromagnetically coupled to the high-spin M'^{2+} ion such that this excited state becomes accessible. For diamagnetic quadruply-bonded Mo_2 compounds, the transition from the singlet $\delta^2\delta^{*0}$ to the triplet $\delta^1\delta^{*1}$ state (a.k.a., the ^{3}δ-δ* transition) has eluded detection, being a rigorously spin-forbidden transition. This energy splitting has been determined experimentally for some phosphine-supported Mo_2 complexes to be in the range of 1,300 to 3,000 cm^{-1}, being strongly influenced by the P–Mo–Mo–P torsion angle around the quadruple bond.[46] Further estimates of the ^{3}δ-δ* energy in the range of 2,400 to 10,400 cm^{-1} have been made for a range of quadruply bonded compounds and their cations with halide, carboxylate, and phosphine supporting ligands.[5] The observed energy here, 12,500 cm^{-1}, is notably larger than in these previous reports, but we anticipate that this is due to the fact that the dedpa ligand is a strong π-donor, raising the energy of the δ* orbitals and leading to a large one-electron δ-δ* splitting (Δ*W*). The observed spin-allowed ("singlet") δ-δ* transitions for **2**-**6** lie in an expected energy range for Mo_2 quadruple bonds because the energies of these transitions are more influenced by two-electron interactions (quantum mechanical exchange, *K*), whereas the spin-forbidden ("triplet") δ-δ* energy is affected more by Δ*W*.[5, 47] Presumably, these ^{3}δ-δ* transitions also occur in the corresponding $Mo_2M'(dpa)_4X_2$ compounds, but would be lower in energy than in **2**-**6** because the dpa ligand is less π-donating than the dedpa ligand.

The assignment of Band E to a ^{3}δ-δ* state is supported by spin unrestricted TD-DFT calculations on **6**, which predict a pair of transitions at 23,393 and 23,564 cm^{-1} with non-

zero intensity that is mostly Mo_2 δ-δ* with some δ-π* character. It is notable that the addition of a paramagnetic metal to the diamagnetic Mo_2 unit provides a mechanism for increasing intensity of the spin-forbidden Mo_2 transitions.

With both singlet δ-δ* energies (average: 14,561 cm^{-1}) and triplet δ-δ* energies (12,500 cm^{-1}) available, we may estimate both *K* and Δ*W* (ignoring the effects of configuration interaction). We find an average value of $K = 2061\ cm^{-1}$, which is smaller than the range of values determined for chloro, phosphino, and carboxylato complexes (4,900 – 8,400 cm^{-1}).[5] The smaller value determined here is consistent with a higher degree of Mo–N covalency than is seen with the other types of ligands. The one-electron δ-δ* splitting Δ*W*, estimated here to be ~12,300 cm^{-1} on average, is within the anticipated range for quadruply bonded complexes. Due to the stronger electron donation of the dedpa ligand, Δ*W* is larger than the lowest energy observed electronic transition for the $[Mo_2(dpa)_4]^+$ cation (~11,000 cm^{-1}),[35] which is a direct measure of Δ*W*.

Section 8: DFT Reaction Mechanism Studies

To gain insight into the fluxional behavior of **1** as compared to $Mo_2(dpa)_4$ (**7**), DFT studies were conducted on both compounds. Crystal structures of both **1** and **7** adopt the *trans*-(2,2) configuration of ligands (Figure S32 in the Appendix), though there is evidence from NMR spectroscopy that other conformations of **1** exist in solution. Importantly, rearrangement of the equatorial ligands is required in order to form the trimetallic HEMACs. The metalloligand precursor compounds must undergo a rearrangement to the (4,0)

configuration in which there is a "pocket" to allow for the binding of a third metal atom (Scheme 4.1.1).

Geometries of both **1** and **7** were optimized to produce **1a** and **7a**. These optimized geometries were found to be in good agreement with experimentally observed bond distances. The *trans*-(2,2) structures **1a** and **7a** were used as a starting point to optimize new structures in the (3,1) configuration, **1b**, **7b**, and in the (4,0) configuration, **1c**, and **7c**. Using these optimized structures, the nudged elastic band (NEB) method[48-49] was employed to locate the transition states along the stepwise pathway shown in Scheme 4.8.1 going from the *trans*-(2,2) to (3,1) geometry (**1TS1, 7TS1**), and from the (3,1) to (4,0) geometry (**1TS2, 7TS2**). Structural data and thermodynamic info for these intermediate species are given in Table 4.8.1.

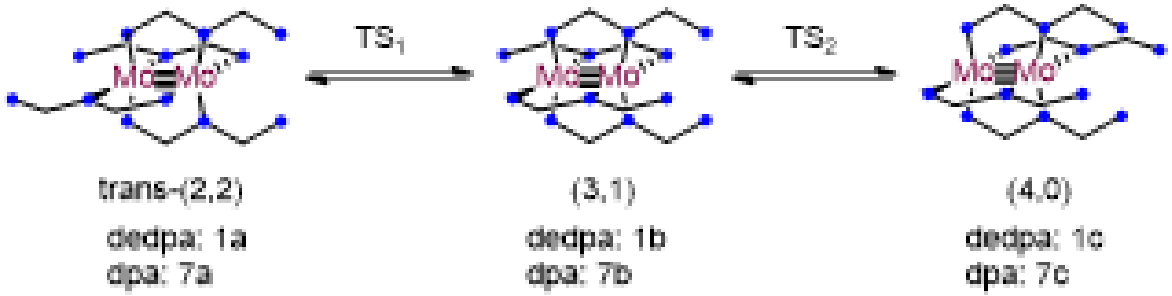

Scheme 4.8.1: Optimized structures for the species involved in ligand shuffling.

The concept of ligand "shuffling" to achieve a (4,0) conformation from a *trans*-(2,2) starting point was proposed as early as 2001 for pyridylamine and pyridylformamidine complexes based on the observation of several isomers in solution by ^{1}H NMR spectroscopy.[50-51] We studied fluxionality of $Cr_2(dpa)_4$ by ^{1}H NMR spectroscopy in the presence and absence of

$ZnCl_2$ and proposed the symmetric coordination mode **I** seen in Scheme 4.8.1. as accounting for intermediate or transition state geometries.[40] The suggestion of coordination mode **I** was based on the fact that this coordination mode has been crystallographically established in several other coordination compounds.[35, 52-56]

The NEB calculations reported here provide us with the first structural picture of this ligand shuffling process. Upon moving from the *trans*-(2,2) to the (3,1) conformation, and also from the (3,1) to the (4,0) conformation, the potential energy landscape consists of a single transition state, **TS1** or **TS2**, respectively, and no metastable intermediate species. Interestingly, the ligand undergoing the longitudinal shuffle does not adopt coordination mode **I** along its pathway, rather we optimize to a new coordination mode, **II**, which sees each pyridine ring bonded to a different metal but the amido group essentially uncoordinated. To our knowledge, there are no existing precedents for this coordination mode of the dpa ligand.

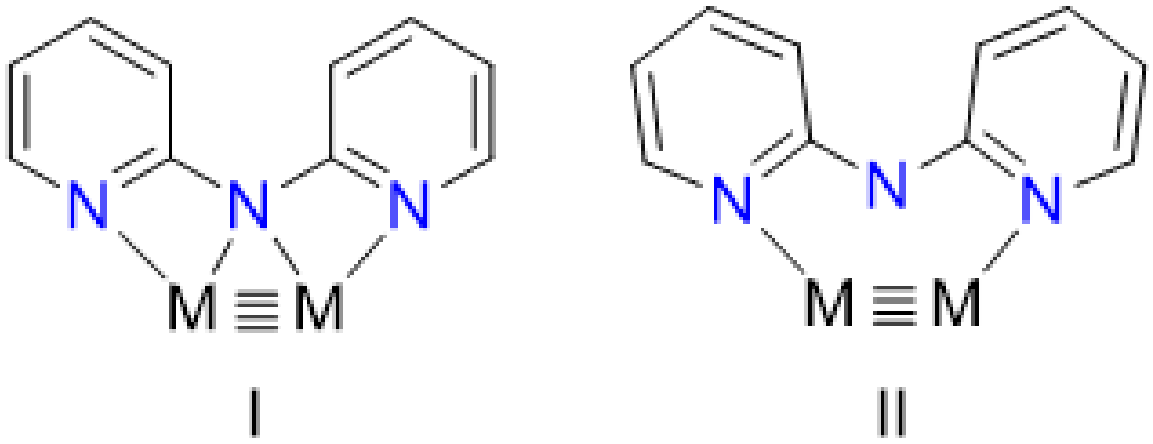

Scheme 4.8.2: Proposed coordination modes along the ligand shuffling pathway. Coordination mode **I** has all three N atoms interacting with the metals of the core whereas coordination mode **II** has only the N atoms in the pyridine rings bound to the core while the amido N is essentially unbound.

The potential energy landscape for equatorial ligand shuffling in **1** and **7** is shown in Figure 4.8.1. Notably, for **1** we find the trans-(2,2) and the (3,1) isomer to be nearly isoenergetic, whereas the trans-(2,2) isomer is clearly the lowest energy stationary point for **7**. Additionally, we calculate the $\Delta G^{\ddagger}$ at 298 K for both **TS1** and **TS2** to be lower for **1** than it is for **7**. This ΔG can further be broken down into its enthalpy and entropy components with values of ΔH of 21.9 and 19.0 kcal/mol for **1** and **7** respectively and values of ΔS of 5.7 and 1.2 cal/mol*T for **1** and **7**. These calculations agree with the fact that there are multiple isomers of **1** that are observable in solution. Although the stronger Mo–N bonds in **1** contribute to a higher transition state enthalpy, the additional degrees of freedom from the ethyl substituents likely make **TS1** for **1** more favorable from an entropy standpoint.

To gain further insight into the cause of the differences in transition state energies, an energy decomposition analysis was performed on **1a,b,c**, **7a,b,c**, and their associated transition states. Here, we include further calculations to determine the energies of just the Mo_2 core (E_{Mo}) and of just the four ligands (E_L), frozen in the geometries optimized for the associated compounds. The total energy E_{Total} of the system must be the sum of these two energetic terms and an interaction energy, E_{Int}, indicating the favorability of the metal-ligand bonds. The term E_{Int} is thus determined by Eq. 4.8.1.

$$E_{Total} = E_{M\text{-}M} + E_{Lig} + E_{Int} \qquad \text{Eqn 4.8.1.}$$

The results of this analysis are showcased in Table 8, with all values relative to the structures of either **1a** or **7a**. Uniformly, E_{Mo} values are relatively small indicating that reorganization of the MoMo bond does not play a substantial role in the energetics of the reaction. Ligand rearrangement energies and the interaction energies, however, are both large meaning that they play substantial roles. When comparing the dpa and dedpa ligands, the ligand reorganization energy along the shuffling pathway is higher for dedpa, but the interaction energy is less destabilizing in the transition states and is actually stabilizing for intermediates **1b** and **1c**. These effects lead to lower barriers in electronic energy for both TS1 and TS2, and greater overall favorability of the shuffling reaction for **1** vs **7**. We attribute this energetic benefit to greater electron donation into the Mo_2 core (or stronger Mo-ligand bonding) from the four relatively electron-rich dedpa ligands.

Table 4.8.1: Energy decomposition breakdown for **1** and **7** given in kcal mol^{-1}

	E_{Total}	E_{M-M}	$E_{Lig.}$	$E_{Int.}$		E_{Total}	E_{M-M}	$E_{Lig.}$	$E_{Int.}$
1a	0	0	0	0	**7a**	0	0	0	0
1TS1	17.21	-0.07	11.18	6.1	**7TS1**	18.84	-0.81	6.16	13.50
1b	0.19	0.25	12.79	-12.85	**7b**	4.12	-0.85	3.24	1.74
1TS2	19.67	0.14	20.02	-0.49	**7TS2**	22.53	0.03	11.96	10.55
1c	5.17	0.69	17.6	-13.12	**7c**	7.90	0.21	9.59	-1.90

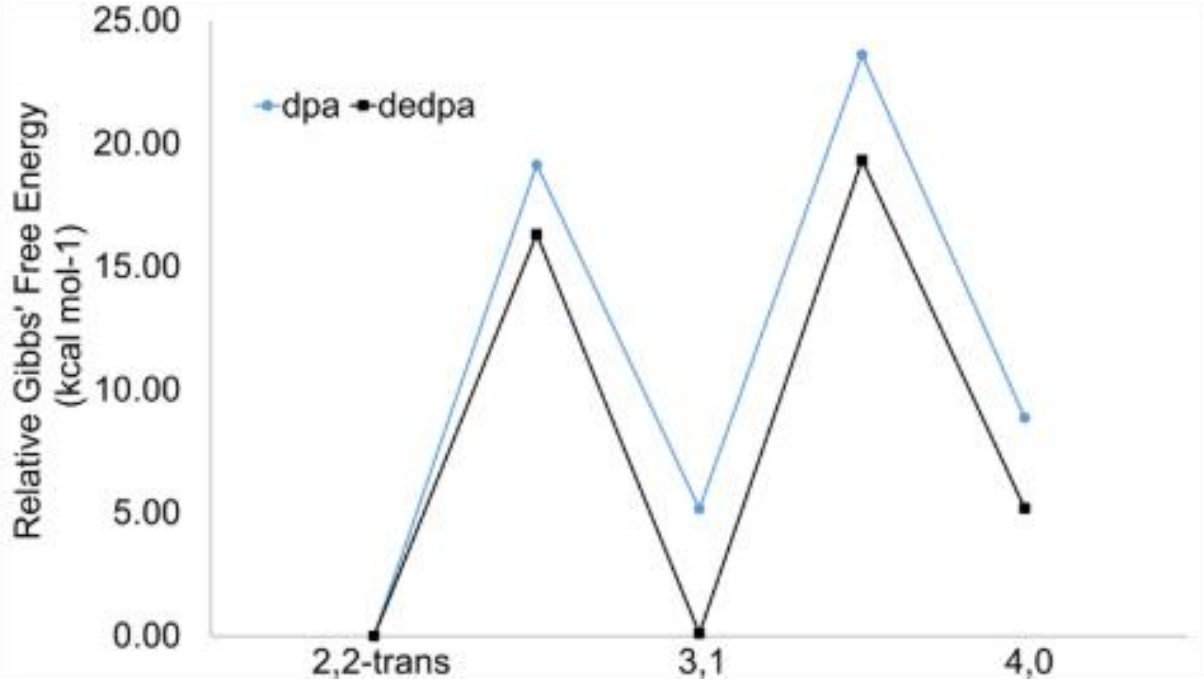

Figure 4.8.1: Relative Gibbs' free energies for the ligand shuffling of **1** and **7** for a stepwise ligand shuffling mechanism. The energies for all transition states and intermediates are relative to the (2,2)-trans configuration of both metalloligands. For each intermediate and transition state after the (2,2)-trans starting point, the energies are higher for **7** than **1**, but by only ~5 kcal mol^{-1} for each point. Calculations were performed with the BP86 functional.

These two conflicting effects of higher reorganization energy due to a larger ligand and more stabilized transition states due to electron donating groups suggest that other substituted dpa ligands are likely to show behavior that cannot be boiled down to a simple, single Hammett substituent effect.

Conclusions

In this work, we have presented the novel syntheses of $Mo_2(dedpa)_4$ (**1**) and five new trimetallic compounds of the form $Mo_2M'(dedpa)_4Cl_2$ with M' = Cr, Mn, Fe, Co, and Ni (**2-6**). We synthesize these compounds using a novel solution-state synthetic method that we show also works for dpa HEMACs of the same form. We find that the effects of the electron donating ethyl sunstituents in the depa ligand are not felt uniformly by the Mo_2 and M' groups. Contrary to our expectations, the more electron-rich dedpa ligand provides a *weaker* ligand field at the M' site with a concomitantly stronger field at the Mo_2 core, which also allows for low energy triplet δ-δ* states to be visible in the absorption spectra of **2-6**. Cyclic voltammetry confirms that the dedpa ligand creates a more electron-rich, and thus easier to oxidize Mo_2 unit with the series of compounds as compared to dpa compounds with similar structures. Computational analysis of the isomerism of **1** in comparison to an unsubstituted version showed that, while reorganization energy is larger for the more bulky dedpa ligand, the stronger metal-ligand bonding leads to lower energy transition states along the ligand shuffling reaction pathway. Overall, these results suggest that the influence of substituents on the dpa ligand is not distributed evenly between the metals of **2-6**, with a stronger effect present on the Mo atoms, and a weakening of the ligand field at the M' heterometal. The fact that these effects occur counter to expectation based on metal atom electronegativities highlights the importance of the heterometallic bond polarity umpolung in these compounds.

References

[1] J. F. Berry, C. C. Lu, Metal–Metal Bonds: From Fundamentals to Applications *Inorg. Chem.* **2017**, *56*, 7577-7581, 10.1021/acs.inorgchem.7b01330.

[2] C. M. Thomas, Metal-Metal Multiple Bonds in Early/Late Heterobimetallic Complexes: Applications Toward Small Molecule Activation and Catalysis *Comments Inorg. Chem.* **2011**, *32*, 14-38, 10.1080/02603594.2011.593213.

[3] B. Wu, M. J. T. Wilding, S. Kuppuswamy, M. W. Bezpalko, B. M. Foxman, C. M. Thomas, Exploring Trends in Metal–Metal Bonding, Spectroscopic Properties, and Conformational Flexibility in a Series of Heterobimetallic Ti/M and V/M Complexes (M = Fe, Co, Ni, and Cu) *Inorg. Chem.* **2016**, *55*, 12137-12148, 10.1021/acs.inorgchem.6b01543.

[4] T. Cheng, M. Meng, H. Lei, C. Y. Liu, Perturbation of the Charge Density between Two Bridged Mo_2 Centers: The Remote Substituent Effects *Inorg. Chem.* **2014**, *53*, 9213-9221, 10.1021/ic501313q.

[5] V. M. Miskowski, M. D. Hopkins, J. R. Winkler, H. B. Gray, in *Inorganic Electronic Structure and Spectroscopy, Volume II: Applications and Case Studies, Vol. 2* (Eds.: E. I. Solomon, A. B. P. Lever), John Wiley and Sons, New York, **1999**, pp. 343-402.

[6] T. Miyazawa, T. Suzuki, Y. Kumagai, K. Takizawa, T. Kikuchi, S. Kato, A. Onoda, T. Hayashi, Y. Kamei, F. Kamiyama, M. Anada, M. Kojima, T. Yoshino, S. Matsunaga, Chiral paddle-wheel diruthenium complexes for asymmetric catalysis *Nat. Catal.* **2020**, *3*, 851-858, 10.1038/s41929-020-00513-w.

[7] I. Tolbatov, P. Umari, A. Marrone, Diruthenium Paddlewheel Complexes Attacking Proteins: Axial versus Equatorial Coordination *Biomolecules* **2024**, *14*, 530,

[8] E. Van Caemelbecke, T. Phan, W. R. Osterloh, K. M. Kadish, Electrochemistry of metal-metal bonded diruthenium complexes *Coord. Chem. Rev.* **2021**, *434*, 213706, 10.1016/j.ccr.2020.213706.

[9] G. A. McCarver, T. Yildirim, W. Zhou, Hetero-bimetallic paddlewheel complexes for enhanced CO_2 reduction selectivity in MOFs: a first principles study *Phys. Chem. Chem. Phys.* **2024**, *26*, 7627-7637, 10.1039/D3CP05694E.

[10] E. V. Dikarev, T. G. Gray, B. Li, Heterobimetallic Main-Group–Transition-Metal Paddle-Wheel Carboxylates *Angew. Chem. Int. Ed.* **2005**, *44*, 1721-1724, 10.1002/anie.200462433.

[11] B. Li, H. Zhang, L. Huynh, M. Shatruk, E. V. Dikarev, Mo/Rh Carboxylate: Heterometallic Compound Built of Homometallic Paddlewheel Units *Inorg. Chem.* **2007**, *46*, 9155-9159, 10.1021/ic7009012.

[12] D. R. Langstieh, R. H. D. Lyngdoh, R. B. King, H. F. Schaefer, Lantern-type dinickel complexes: An exploration of possibilities for nickel–nickel bonding with bridging bidentate ligands *J. Comput. Chem.* **2023**, *44*, 355-366, 10.1002/jcc.26936.

[13] G. Parkin, in *Metal-Metal Bonding* (Ed.: G. Parkin), Springer Berlin Heidelberg, Berlin, Heidelberg, **2010**, pp. 113-145.

[14] R. Wolf, C. Ni, T. Nguyen, M. Brynda, G. J. Long, A. D. Sutton, R. C. Fischer, J. C. Fettinger, M. Hellman, L. Pu, P. P. Power, Substituent Effects in Formally Quintuple-Bonded

ArCrCrAr Compounds (Ar = Terphenyl) and Related Species *Inorg. Chem.* **2007**, *46*, 11277-11290, 10.1021/ic702112e.

[15] M. A. Esteruelas, S. Moreno-Blázquez, M. Oliván, E. Oñate, N,C,N-Pincers in Platinum Bimetallic Complexes: Influence of the Pincer and Bridging Ligands on the Metal–Metal Bond and the Photophysical Properties *Inorg. Chem.* **2024**, *63*, 14482-14494, 10.1021/acs.inorgchem.4c01712.

[16] H. Han, Z. Wei, M. C. Barry, J. C. Carozza, M. Alkan, A. Y. Rogachev, A. S. Filatov, A. M. Abakumov, E. V. Dikarev, A three body problem: a genuine heterotrimetallic molecule vs. a mixture of two parent heterobimetallic molecules *Chem. Sci.* **2018**, *9*, 4736-4745, 10.1039/C8SC00917A.

[17] J. P. Krogman, C. M. Thomas, Metal–metal multiple bonding in C_3-symmetric bimetallic complexes of the first row transition metals *Chem. Commun.* **2014**, *50*, 5115-5127, 10.1039/C3CC47537A.

[18] M. Imperato, A. Nicolini, M. Boniburini, D. Sartini, E. Benassi, M. Chiesa, L. Gigli, Y.-K. Liao, A. Raza, E. Salvadori, L. Sorace, A. Cornia, Dual Structure of a Vanadyl-Based Molecular Qubit Containing a Bis(β-diketonato) Ligand *Inorg. Chem.* **2024**, *63*, 7912-7925, 10.1021/acs.inorgchem.4c00834.

[19] M. Imperato, A. Nicolini, O. Mironova, E. Benassi, N. Demitri, L. Gigli, A. Mucci, A. Cornia, Conclusive Insight into the Coordination Complexes of a Flexible Bis(β-diketonato) Ligand and Their Phase-Dependent Structure: A Multi-Technique Approach *Chem. Eur. J.* **2025**, *31*, e202500697, 10.1002/chem.202500697.

[20] T. Ren, Substituent effects in dinuclear paddlewheel compounds: electrochemical and spectroscopic investigations *Coord. Chem. Rev.* **1998**, *175*, 43-58, 10.1016/S0010-8545(98)00202-1.

[21] H. Dong, Q. Meng, B.-Z. Chen, Y.-B. Wu, Theoretical studies on the multiple metal–metal bonds in the bimetallic molecules and the ultrashort V–Mn bonds in the complexes *J. Organomet. Chem.* **2012**, *717*, 108-115, 10.1016/j.jorganchem.2012.07.035.

[22] B. G. Cooper, C. M. Fafard, B. M. Foxman, C. M. Thomas, Electronic Factors Affecting Metal−Metal Interactions in Early/Late Heterobimetallics: Substituent Effects in Zirconium/Platinum Bis(phosphinoamide) Complexes *Organometallics* **2010**, *29*, 5179-5186, 10.1021/om100356a.

[23] T. L. Sunderland, J. F. Berry, Expanding the family of heterobimetallic Bi–Rh paddlewheel carboxylate complexes via equatorial carboxylate exchange *Dalton Trans.* **2016**, *45*, 50-55, 10.1039/C5DT03740A.

[24] E. V. Dikarev, B. Li, H. Zhang, Tuning the Properties at Heterobimetallic Core: Mixed-Ligand Bismuth−Rhodium Paddlewheel Carboxylates *J. Am. Chem. Soc.* **2006**, *128*, 2814-2815, 10.1021/ja058294h.

[25] A. J. Ayres, M. Zegke, J. P. A. Ostrowski, F. Tuna, E. J. L. McInnes, A. J. Wooles, S. T. Liddle, Actinide-transition metal bonding in heterobimetallic uranium– and thorium–molybdenum paddlewheel complexes *Chem. Commun.* **2018**, *54*, 13515-13518, 10.1039/C8CC05268A.

[26] M.-M. Rohmer, A. Strich, M. Bénard, J.-P. Malrieu, Metal–Metal Bond Length Variability in Co_3(dipyridylamide)$_4Cl_2$: Bond-Stretch Isomerism, Crystal Field Effects, or Spin Transition Process? A DFT Study *J. Am. Chem. Soc.* **2001**, *123*, 9126-9134, 10.1021/ja0103142.

[27] A. M. Wheaton, J. A. Chipman, M. D. Roy, J. F. Berry, Metal–Metal Bond Umpolung in Heterometallic Extended Metal Atom Chains *Inorg. Chem.* **2022**, *61*, 15058-15069, 10.1021/acs.inorgchem.2c02118.

[28] J. F. Berry, F. A. Cotton, T. Lu, C. A. Murillo, Increasing Solubility and Stability of Linear Tricobalt(II) Chains with depa (Diethyldipyridylamide) Ligands *Inorg. Chem.* **2003**, *42*, 4425-4430, 10.1021/ic034149y.

[29] J. F. Berry, F. A. Cotton, T. Lu, C. A. Murillo, X. Wang, Enhancing the Stability of Trinickel Molecular Wires and Switches: Ni_3^{6+}/Ni_3^{7+} *Inorg. Chem.* **2003**, *42*, 3595-3601, 10.1021/ic0341486.

[30] M. Elie, F. Sguerra, F. Di Meo, M. D. Weber, R. Marion, A. Grimault, J.-F. Lohier, A. Stallivieri, A. Brosseau, R. B. Pansu, J.-L. Renaud, M. Linares, M. Hamel, R. D. Costa, S. Gaillard, Designing NHC–Copper(I) Dipyridylamine Complexes for Blue Light-Emitting Electrochemical Cells *ACS Appl. Mater. Interfaces* **2016**, *8*, 14678-14691, 10.1021/acsami.6b04647.

[31] R. Marion, F. Sguerra, F. Di Meo, E. Sauvageot, J.-F. Lohier, R. Daniellou, J.-L. Renaud, M. Linares, M. Hamel, S. Gaillard, NHC Copper(I) Complexes Bearing Dipyridylamine

Ligands: Synthesis, Structural, and Photoluminescent Studies *Inorg. Chem.* **2014**, *53*, 9181-9191, 10.1021/ic501230m.

[32] D. W. Brogden, J. H. Christian, N. S. Dalal, J. F. Berry, Completing the series of Group VI heterotrimetallic $M_2Cr(dpa)_4Cl_2$ (M_2=Cr_2, Mo_2, MoW and W_2) compounds and investigating their metal–metal interactions using density functional theory *Inorg. Chim. Acta* **2015**, *424*, 241-247, 10.1016/j.ica.2014.08.020.

[33] J. A. Chipman, J. F. Berry, Extraordinarily Large Ferromagnetic Coupling (J≥150 cm^{-1}) by Electron Delocalization in a Heterometallic Mo≣Mo−Ni Chain Complex *Chem. Eur. J.* **2018**, *24*, 1494-1499, 10.1002/chem.201704588.

[34] M. Nippe, E. Victor, J. F. Berry, Do Metal–Metal Multiply-Bonded "Ligands" Have a trans Influence? Structural and Magnetic Comparisons of Heterometallic Cr≣Cr···Co and Mo≣Mo···Co Interactions *Eur. J. Inorg. Chem.* **2008**, 5569-5572, 10.1002/ejic.200801001.

[35] M. Nippe, E. Victor, J. F. Berry, Oxidation Chemistry of Axially Protected Mo_2 and W_2 Quadruply Bonded Compounds *Inorg. Chem.* **2009**, *48*, 11889-11895, 10.1021/ic901965b.

[36] M. Nippe, J. Wang, E. Bill, H. Hope, N. S. Dalal, J. F. Berry, Crystals in Which Some Metal Atoms are More Equal Than Others: Inequalities From Crystal Packing and Their Spectroscopic/Magnetic Consequences *J. Am. Chem. Soc.* **2010**, *132*, 14261-14272, 10.1021/ja106510g.

[37] M. Nippe, J. F. Berry, Introducing a Metal–Metal Multiply Bonded Group as an “Axial Ligand” to Iron: Synthetic Design of a Linear Cr–Cr···Fe Framework *J. Am. Chem. Soc.* **2007**, *129*, 12684-12685, 10.1021/ja076337j.

[38] J. A. Chipman, J. F. Berry, Paramagnetic Metal–Metal Bonded Heterometallic Complexes *Chem. Rev.* **2020**, *120*, 2409-2447, 10.1021/acs.chemrev.9b00540.

[39] A. M. Wheaton, J. A. Chipman, R. K. Walde, H. Hofstetter, J. F. Berry, Chemically Separable Co(II) Spin-State Isomers *J. Am. Chem. Soc.* **2024**, *146*, 26926-26935, 10.1021/jacs.4c08097.

[40] M. Nippe, E. Bill, J. F. Berry, Group 6 Complexes with Iron and Zinc Heterometals: Understanding the Structural, Spectroscopic, and Electrochemical Properties of a Complete Series of MM···M' Compounds *Inorg. Chem.* **2011**, *50*, 7650-7661, 10.1021/ic2011315.

[41] C. Lin, J. D. Protasiewicz, E. T. Smith, T. Ren, Linear Free Energy Relationships in Dinuclear Compounds. 2. Inductive Redox Tuning via Remote Substituents in Quadruply Bonded Dimolybdenum Compounds *Inorg. Chem.* **1996**, *35*, 6422-6428, 10.1021/ic960555o.

[42] A. R. Chakravarty, F. A. Cotton, E. S. Shamshoum, 2-Anilinopyridine complexes of dimolybdenum(II) and ditungsten(II) *Inorg. Chem.* **1984**, *23*, 4216-4221, 10.1021/ic00193a024.

[43] J. F. Berry, F. A. Cotton, T. Lu, C. A. Murillo, B. K. Roberts, X. Wang, Molecular and Electronic Structures by Design: Tuning Symmetrical and Unsymmetrical Linear Trichromium Chains *J. Am. Chem. Soc.* **2004**, *126*, 7082-7096, 10.1021/ja049055h.

[44] R. Clérac, F. A. Cotton, L. M. Daniels, K. R. Dunbar, C. A. Murillo, I. Pascual, Linear Trichromium Complexes with Direct Cr to Cr Contacts. 2. Compounds with Cr_3(dipyridylamide)$_4^{3+}$ Cores *Inorg. Chem.* **2000**, *39*, 752-756, 10.1021/ic991022t.

[45] J. A. Chipman, J. F. Berry, Facile Axial Ligand Substitution in Linear Mo≣Mo–Ni Complexes *Inorg. Chem.* **2018**, *57*, 9354-9363, 10.1021/acs.inorgchem.8b01331.

[46] F. A. Cotton, J. L. Eglin, B. Hong, C. A. James, Singlet-triplet separations measured by phosphorus-31{proton} NMR; applications to quadruply-bonded dimolybdenum and ditungsten complexes *Inorg. Chem.* **1993**, *32*, 2104-2106, 10.1021/ic00062a037.

[47] F. A. Cotton, D. G. Nocera, The Whole Story of the Two-Electron Bond, with the δ Bond as a Paradigm *Acc. Chem. Res.* **2000**, *33*, 483-490, 10.1021/ar980116o.

[48] G. Henkelman, H. Jónsson, Improved tangent estimate in the nudged elastic band method for finding minimum energy paths and saddle points *J. Chem. Phys.* **2000**, *113*, 9978-9985, 10.1063/1.1323224.

[49] G. Mills, H. Jónsson, G. K. Schenter, Reversible work transition state theory: application to dissociative adsorption of hydrogen *Surf. Sci.* **1995**, *324*, 305-337, 10.1016/0039-6028(94)00731-4.

[50] R. Clérac, F. A. Cotton, K. R. Dunbar, C. A. Murillo, X. Wang, Dinuclear and Heteropolynuclear Complexes Containing Mo_2^{4+} Units *Inorg. Chem.* **2001**, *40*, 420-426, 10.1021/ic001002n.

[51] R. Clérac, F. Albert Cotton, S. P. Jeffery, C. A. Murillo, X. Wang, Isomerization by ligand shuffling along a Cr_2^{4+} unit: further reactions leading to cleavage of a quadruple bond *Dalton Trans.* **2003**, 3022-3027, 10.1039/B305304K.

[52] F. A. Cotton, L. M. Daniels, C. A. Murillo, H.-C. Zhou, Metal-metal versus metal-ligand bonding in dimetal compounds with tridentate ligands *Inorg. Chim. Acta* **2000**, *305*, 69-74, 10.1016/S0020-1693(00)00115-8.

[53] K. Müller-Buschbaum, Erste Dipyridylamide der Selten-Erd-Elemente: Neuartige Selten-Erd-Stickstoff-Koordinationen in $[Ln(N(C_5H_4N)_2)_3]_2$, Ln = La, Gd, Yb *Z. Anorg. Allg. Chem.* **2003**, *629*, 2127-2132, 10.1002/zaac.200300189.

[54] J. F. Berry, F. A. Cotton, C. A. Murillo, Mono-, di-, and tri-ruthenium complexes with the ligand 2,2'-dipyridylamide (dpa): insights into the formation of extended metal atom chains *Inorg. Chim. Acta* **2004**, *357*, 3847-3853, 10.1016/j.ica.2004.02.041.

[55] K. Müller-Buschbaum, C. C. Quitmann, Homoleptic Rare Earth Dipyridylamides $[Ln_2(N(NC_5H_4)_2)_6]$, Ln = Ce, Nd, Sm, Ho, Er, Tm, Yb, and Sc: Metal Oxidation by the Amine Melt and in 1,2,3,4-Tetrahydroquinoline with the Focus of Different Metal Activation by Amalgams, Liquid Ammonia, and Microwaves *Inorg. Chem.* **2006**, *45*, 2678-2687, 10.1021/ic0514795.

[56] D. W. Brogden, J. F. and Berry, Coordination Chemistry of 2,2'-Dipyridylamine: The Gift That Keeps on Giving *Comments Inorg. Chem.* **2016**, *36*, 17-37, 10.1080/02603594.2015.1079522.

[57] APEX4, 2022.1-1, Bruker-AXS, Madison, Wisconsin, USA, **2022.**

[58] G. A. Bain, J. F. Berry, Diamagnetic Corrections and Pascal's Constants *J. Chem. Educ.* **2008**, *85*, 532, 10.1021/ed085p532.

[59] A. D. Becke, Density-functional thermochemistry. III. The role of exact exchange *J. Chem. Phys.* **1993**, *98*, 5648-5652, 10.1063/1.464913.

[60] T. Bender, P. von Zezschwitz, Total Synthesis of 4-Acetyl-1,3-Dihydroimidazo[4,5-c]Pyridin-2-One, a New Microbial Metabolite from a Streptomyces Species *Nat. Prod. Commun.* **2009**, *4*, 1934578X0900400719, 10.1177/1934578X0900400719.

[61] V. Bonnet, F. Mongin, F. Trécourt, G. Quéguiner, P. Knochel, Syntheses of substituted pyridines, quinolines and diazines via palladium-catalyzed cross-coupling of aryl Grignard reagents *Tetrahedron* **2002**, *58*, 4429-4438, 10.1016/S0040-4020(02)00411-8.

[62] F. H. Case, T. J. Kasper, The Preparation of Some Substituted 2,6-Bis-(2-pyridyl)-pyridines *J. Am. Chem. Soc.* **1956**, *78*, 5842-5844, 10.1021/ja01603a036.

[63] N. F. Chilton, R. P. Anderson, L. D. Turner, A. Soncini, K. S. Murray, PHI: A powerful new program for the analysis of anisotropic monomeric and exchange-coupled polynuclear d- and f-block complexes *J. Comput. Chem.* **2013**, *34*, 1164-1175, 10.1002/jcc.23234.

[64] J. E. Dennis, D. M. Gay, R. E. Walsh, An Adaptive Nonlinear Least-Squares Algorithm *ACM Trans. Math. Softw.* **1981**, *7*, 348–368, 10.1145/355958.355965.

[65] M. Garcia-Ratés, F. Neese, Effect of the Solute Cavity on the Solvation Energy and its Derivatives within the Framework of the Gaussian Charge Scheme *J. Comput. Chem.* **2020**, *41*, 922-939, 10.1002/jcc.26139.

[66] T. D. Goddard, C. C. Huang, E. C. Meng, E. F. Pettersen, G. S. Couch, J. H. Morris, T. E. Ferrin, UCSF ChimeraX: Meeting modern challenges in visualization and analysis *Protein Sci.* **2018**, *27*, 14-25, 10.1002/pro.3235.

[67] S. Grimme, J. Antony, S. Ehrlich, H. Krieg, A consistent and accurate ab initio parametrization of density functional dispersion correction (DFT-D) for the 94 elements H-Pu *J. Chem. Phys.* **2010**, *132*, 154104, 10.1063/1.3382344.

[68] S. Grimme, S. Ehrlich, L. Goerigk, Effect of the damping function in dispersion corrected density functional theory *J. Comput. Chem.* **2011**, *32*, 1456-1465, 10.1002/jcc.21759.

[69] F. Kleemiss, O. V. Dolomanov, M. Bodensteiner, N. Peyerimhoff, L. Midgley, L. J. Bourhis, A. Genoni, L. A. Malaspina, D. Jayatilaka, J. L. Spencer, F. White, B. Grundkötter-Stock, S. Steinhauer, D. Lentz, H. Puschmann, S. Grabowsky, Accurate crystal structures and chemical properties from NoSpherA2 *Chem. Sci.* **2021**, *12*, 1675-1692, 10.1039/D0SC05526C.

[70] L. Krause, R. Herbst-Irmer, G. M. Sheldrick, D. Stalke, Comparison of silver and molybdenum microfocus X-ray sources for single-crystal structure determination *J. Appl. Crystallogr.* **2015**, *48*, 3-10, 10.1107/S1600576714022985.

[71] C. Lee, W. Yang, R. G. Parr, Development of the Colle-Salvetti correlation-energy formula into a functional of the electron density *Phys. Rev. B: Condens. Matter* **1988**, *37*, 785-789, 10.1103/PhysRevB.37.785.

[72] P.-O. Löwdin, *Advances in quantum chemistry, Vol. 11*, Academic Press, **1979**.

[73] P. O. Löwdin, On the Non-Orthogonality Problem Connected with the Use of Atomic Wave Functions in the Theory of Molecules and Crystals *J. Chem. Phys.* **1950**, *18*, 365-375, 10.1063/1.1747632.

[74] E. C. Meng, T. D. Goddard, E. F. Pettersen, G. S. Couch, Z. J. Pearson, J. H. Morris, T. E. Ferrin, UCSF ChimeraX: Tools for structure building and analysis *Protein Sci.* **2023**, *32*, e4792, 10.1002/pro.4792.

[75] F. Neese, Prediction and interpretation of the ^{57}Fe isomer shift in Mössbauer spectra by density functional theory *Inorg. Chim. Acta* **2002**, *337*, 181-192, 10.1016/S0020-1693(02)01031-9.

[76] F. Neese, An improvement of the resolution of the identity approximation for the formation of the Coulomb matrix *J. Comput. Chem.* **2003**, *24*, 1740-1747, 10.1002/jcc.10318.

[77] F. Neese, Software update: The ORCA program system—Version 5.0 *Wiley Interdiscip. Rev. Comput. Mol. Sci.* **2022**, *12*, e1606, 10.1002/wcms.1606.

[78] F. Neese, The SHARK integral generation and digestion system *J. Comput. Chem.* **2023**, *44*, 381-396, 10.1002/jcc.26942.

[79] D. A. Pantazis, X.-Y. Chen, C. R. Landis, F. Neese, All-Electron Scalar Relativistic Basis Sets for Third-Row Transition Metal Atoms *J. Chem. Theory Comput.* **2008**, *4*, 908-919, 10.1021/ct800047t.

[80] J. P. Perdew, K. Burke, M. Ernzerhof, Generalized Gradient Approximation Made Simple *Phys. Rev. Lett.* **1996**, *77*, 3865-3868, 10.1103/PhysRevLett.77.3865.

[81] E. F. Pettersen, T. D. Goddard, C. C. Huang, E. C. Meng, G. S. Couch, T. I. Croll, J. H. Morris, T. E. Ferrin, UCSF ChimeraX: Structure visualization for researchers, educators, and developers *Protein Sci.* **2021**, *30*, 70-82, 10.1002/pro.3943.

[82] I. Prisecaru, WMOSS4 Mossbauer spectral analysis software, **2009.**

[83] M. Römelt, S. Ye, F. Neese, Calibration of Modern Density Functional Theory Methods for the Prediction of ^{57}Fe Mössbauer Isomer Shifts: Meta-GGA and Double-Hybrid Functionals *Inorg. Chem.* **2009**, *48*, 784-785, 10.1021/ic801535v.

[84] G. Sheldrick, SHELXT - Integrated space-group and crystal-structure determination *Acta Crystallogr. Sect. A* **2015**, *71*, 3-8, 10.1107/S2053273314026370.

[85] G. Sheldrick, Crystal structure refinement with SHELXL *Acta Crystallogr. Sect. C* **2015**, *71*, 3-8, 10.1107/S2053229614024218.

[86] S. Sinnecker, L. D. Slep, E. Bill, F. Neese, Performance of Nonrelativistic and Quasi-Relativistic Hybrid DFT for the Prediction of Electric and Magnetic Hyperfine Parameters in ^{57}Fe Mössbauer Spectra *Inorg. Chem.* **2005**, *44*, 2245-2254, 10.1021/ic048609e.

[87] A. Spek, PLATON SQUEEZE: a tool for the calculation of the disordered solvent contribution to the calculated structure factors *Acta Crystallogr. Sect. C* **2015**, *71*, 9-18, doi:10.1107/S2053229614024929.

[88] P. J. Stephens, F. J. Devlin, C. F. Chabalowski, M. J. Frisch, Ab initio calculation of vibrational absorption and circular dichroism spectra using density functional force fields *J. Phys. Chem.* **1994**, *98*, 11623-11627,

[89] S. Stoll, A. Schweiger, EasySpin, a comprehensive software package for spectral simulation and analysis in EPR *J. Magn. Reson.* **2006**, *178*, 42-55, 10.1016/j.jmr.2005.08.013.

[90] S. H. Vosko, L. Wilk, M. Nusair, Accurate spin-dependent electron liquid correlation energies for local spin density calculations: a critical analysis *Can. J. Phys.* **1980**, *58*, 1200-1211, 10.1139/p80-159.

[91] F. Weigend, Accurate Coulomb-fitting basis sets for H to Rn *Phys. Chem. Chem. Phys.* **2006**, *8*, 1057-1065, 10.1039/B515623H.

[92] F. Weigend, R. Ahlrichs, Balanced basis sets of split valence, triple zeta valence and quadruple zeta valence quality for H to Rn: Design and assessment of accuracy *Phys. Chem. Chem. Phys.* **2005**, *7*, 3297-3305, 10.1039/B508541A.

[93] T. Yanai, D. P. Tew, N. C. Handy, A new hybrid exchange–correlation functional using the Coulomb-attenuating method (CAM-B3LYP) *Chem. Phys. Lett.* **2004**, *393*, 51-57, 10.1016/j.cplett.2004.06.011.

[94] R. K. Walde, T. C. Pankratz, J. F. Berry; **2025**; .xyz files for HEMAC complexes;Dryad; 10.5061/dryad.jq2bvq8nb

[95] R. K. Walde, A. M. Wheaton, J. F. Berry; **2025**; Deposition Numbers 2456099 (1), 2455982 (2), 2456098 (3), 2455984 (4), 2455983 (5), and 2456097 (6) contain the supplementary crystallographic data for this paper. These data are provided free of charge by the joint Cambridge Crystallographic Data Centre and Fachinformationszentrum Karlsruhe Access Structures service;Cambridge Crystallographic Data Center;